

UNCLASSIFIED

AD NUMBER
AD802033
NEW LIMITATION CHANGE
TO Approved for public release, distribution unlimited
FROM Distribution authorized to U.S. Gov't. agencies and their contractors; Critical Technology; NOV 1957. Other requests shall be referred to Air Research and Development Command, Washington, DC.
AUTHORITY
SAMSO USAF ltr, 28 Feb 1972

THIS PAGE IS UNCLASSIFIED

AD 802033

~~SECRET~~

LMSD-2600

COPY NO. 40
63 SHEETS

**X-17 RE-ENTRY TEST VEHICLE
R- 26 FINAL FLIGHT REPORT**

**SUBMITTED
UNDER CONTRACT**

AF 04 (645)-7

**MODEL AF X-17
MSD-0203**

This document is subject to
special export controls and
each transmittal to foreign
nationals may be made only
with prior approval of
AFSSD CODE SS-0

This document contains information affecting the national defense of the United States within the meaning of the Espionage Laws, Title 18, U.S.C. Sec. 793 and 794. Its transmission or the revelation of its contents in any manner to an unauthorized person is prohibited by law.

~~SECRET~~

LMSD-2600

FOREWORD

THIS IS THE FINAL FLIGHT REPORT OF THE TWENTY-SIXTH RESEARCH FLIGHT OF THE X-17 PROJECT. TWENTY-FIVE RESEARCH VEHICLES WERE FLOWN BY THE MISSILE SYSTEMS DIVISION, LOCKHEED AIRCRAFT CORPORATION, UNDER LETTER CONTRACT AF 04(645)-7 WITH THE BALLISTIC MISSILES DIVISION, AIR RESEARCH AND DEVELOPMENT COMMAND. THE TWENTY-SIXTH FLIGHT WAS FLOWN ACCORDING TO CONTRACT CHANGE NOTICE NO. 23, DATED 2 MAY 1957.

PREPARED BY:

D. M. Tellep

D. M. TELLEP

H. Hoshizaki

H. HOSHIZAKI

APPROVED BY:

M. Tucker

M. TUCKER

APPROVED:

J. M. McCutcheon

J. M. McCUTCHEON

Department Manager

X-17 Project Department

CONTENTS

<u>Section</u>	<u>Page</u>
Foreword	ii
List of Figures	iv
List of Tables	vi
Nomenclature	vii
Summary	1
Introduction	2
Trajectory	4
Instrumentation	7
Surface Finish	10
Telemetry and Data Reduction	12
Thermocouple Data-Smoothing Technique	13
Methods of Analysis	14
Discussion of Results	17
General Observations	17
Re-Entry Temperature Data	24
Re-Entry Heat Rates	26
Behavior of Transition Parameters	33
Exit Temperatures, Reynolds Number, and Accelerations	34
Pressure Measurements	35
Figures 1 - 69	37 - 103
References	104

LIST OF FIGURES

<u>Figure No.</u>	<u>Title</u>	<u>Page</u>
Frontispiece	R-26 at Launch.	x
1.	R-26 Flight Trajectory, First Stage	37
2.	R-26 Velocity and Altitude Histories, First-Stage Boost	38
3.	R-26 Reynolds-Number and Mach-Number Time Histories during First-Stage Boost.	39
4.	R-26 Velocity and Altitude Time Histories, Second- and Third-Stage Boost	40
5.	R-26 Reynolds-Number and Mach-Number Histories during Second- and Third-Stage Boost.	41
6.	R-26 Longitudinal Accelerations during Re-Entry . .	42
7.	R-26 Normal and Lateral Accelerations during Re-Entry.	43
8.	R-26 Nose, Thermocouple and Pressure-Orifice Locations	44
9.	Summary of X-17 Transition Reynolds Number on Hemispheres	45
10-32.	Actual Temperature Data during Re-Entry, Thermocouples A through W	46-68
33.	Comparison of Measured Temperatures on Long and Short Roughness Runs during Re-Entry.	69
34.	Comparison of Measured Temperatures on Control Run and Long Rough Run during Re-Entry.	70
35-44.	Comparison of Observed and Predicted Heat Rates at Thermocouples A through W (Re-Entry).	71-80
45.	Heat-Transfer Distributions on the X-17 Nose during Re-Entry, Data from Thermocouples A through J and O through W	81

LIST OF FIGURES (Continued)

<u>Figure No.</u>	<u>Title</u>	<u>Page</u>
46.	Heat-Transfer Distributions on the X-17 Nose during Re-Entry, Data from Thermocouples A and K through N	82
47.	Ratio of rms Surface Roughness to Momentum Thickness vs. Momentum-Thickness Reynolds Number during Re-Entry	83
48.	Boundary-Layer Cooling Ratio During Re-Entry. . . .	84
49.	Boundary-Layer Cooling-Ratio Distribution during Re-Entry.	85
50.	Typical Temperature-Time History during Exit. . . .	86
51.	Longitudinal Accelerations during Exit.	86
52.	Comparison of Measured Temperatures on Long and Short Roughness runs during Exit.	87
53.	Temperature Profiles on the Nose during Exit, Data from Thermocouples A and K through N.	88
54.	Momentum-Thickness Reynolds Number during Exit. . .	89
55-63.	Actual Pressure Data during Re-Entry.	90-97
64.	Comparison of Observed and Predicted Pressures during Re-Entry	98
65.	Theoretical Laminar Heat-Transfer Distribution on a Hemisphere.	99
66.	\tilde{Re}/Re_{1R} as a Function of Angular Position on a Hemisphere.	100
67.	$(\tilde{Re}_{wT}/Re_{1R})(\mu_w/\mu_1)(T_w/T_1)(1/F_1)$ as a Function of Angular Position on a Hemisphere.	101
68.	η as a Function of Angular Position on a Hemisphere	102
69.	$\rho_e u_e / \rho_1 u_1$ as a Function of Angular Position for Various Free-Stream Mach Numbers.	103

LIST OF TABLES

<u>Table</u>	<u>Title</u>	<u>Page</u>
I	Summary of Important Events	5
II	R-26 Thermocouple Locations	8
III	R-26 Pressure-Orifice Locations	9
IV	List of Surface Defects	11
V	Summary of Transition Events	21
VI	Conditions on Hemispheres at Transition	22

NOMENCLATURE

c	Specific heat
c_{fe}	Skin-friction coefficient
D	Body diameter
e	Internal energy
f	Density ratio = $(\bar{\rho} / \rho_w)$
h	Static enthalpy
H	Total enthalpy
k	Thermal conductivity
m	Molecular weight
M	Mach number
M	Modulus in heat-conduction equations = $-\frac{\Delta y^2}{\alpha \Delta t}$
p	Pressure
Pr	Prandtl number
q	Heat rate
r	Distance from axis of revolution to body surface
R	Body radius
\tilde{Re}	Integrated Reynolds number = $\frac{\int_0^x \rho_e \mu_e u_e r_o^2 dx}{\mu_e^2 r_o^2}$
Re_{1D}	Reynolds number based on diameter and free-stream conditions = $\frac{\rho_1 u_1 D}{\mu_1}$

NOMENCLATURE

c	Specific heat
c_{fe}	Skin-friction coefficient
D	Body diameter
e	Internal energy
f	Density ratio = $(\bar{\rho} / \rho_w)$
h	Static enthalpy
H	Total enthalpy
k	Thermal conductivity
m	Molecular weight
M	Mach number
M	Modulus in heat-conduction equations = $\frac{\Delta y^2}{\alpha \Delta t}$
p	Pressure
Pr	Prandtl number
q	Heat rate
r	Distance from axis of revolution to body surface
R	Body radius
\tilde{Re}	Integrated Reynolds number = $\frac{\int_0^x \rho_e \mu_e u_e r_o^2 dx}{\mu_e^2 r_o^2}$
Re_{1D}	Reynolds number based on diameter and free-stream conditions = $\frac{\rho_1 u_1 D}{\mu_1}$

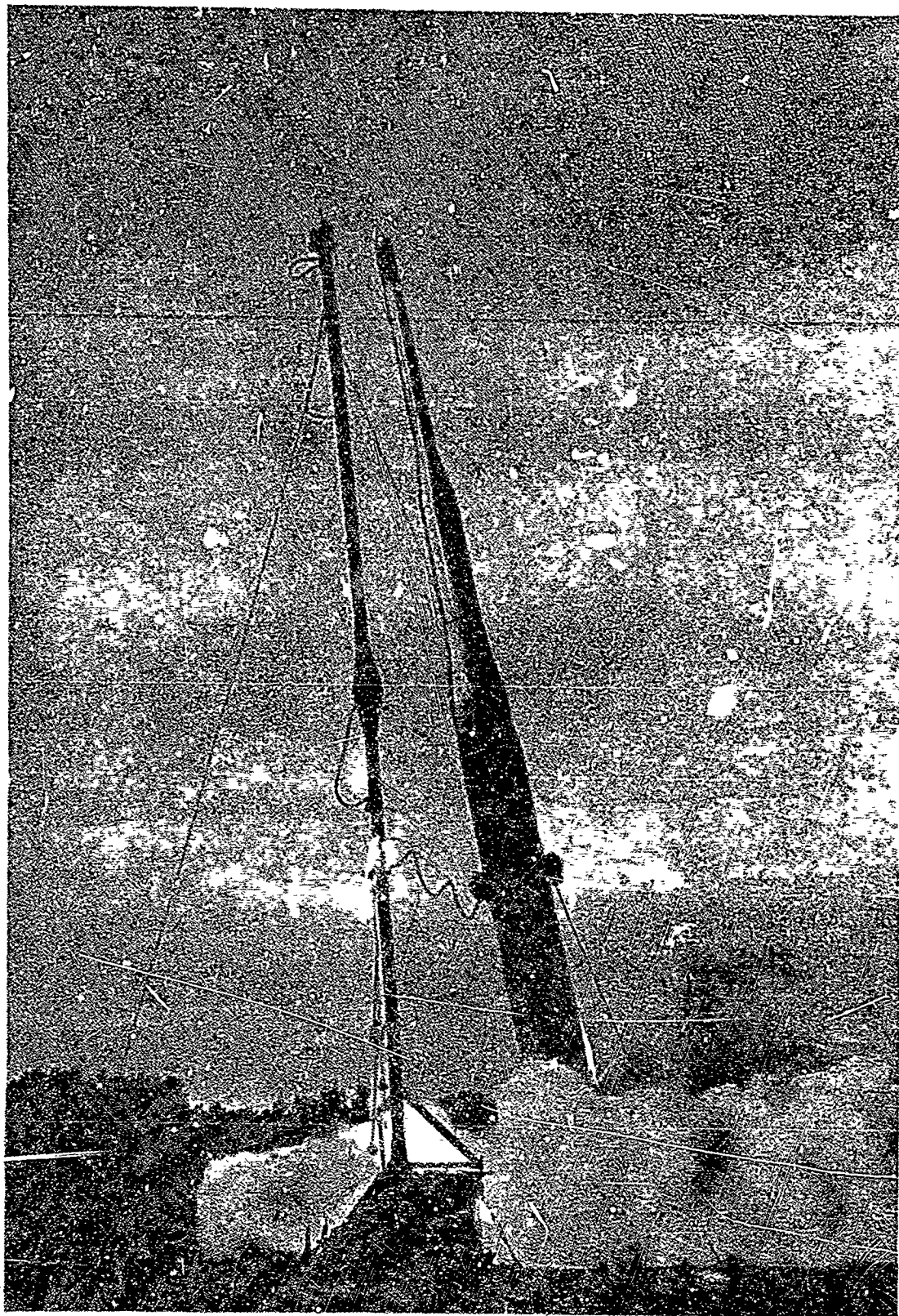
- Re_{LR} Reynolds number based on body radius and free-stream conditions = $\frac{\rho_1 u_1 R}{\mu_1}$
- Re_{WT} Turbulent Reynolds number = $\frac{\int_0^x \rho_w u_e^2 r_o dx}{\mu_w r_o u_e}$
- Re_θ Reynolds number based on local conditions and momentum thickness = $\frac{\rho_e u_e \theta}{\mu_e}$
- t Time
- T Temperature
- u Velocity
- x Distance along body surface, measured from stagnation point
- y Distance normal to body surface
- z Velocity ratio = (\bar{u}/u_e)
- α Thermal diffusivity = $k/\rho c$
- β Angle between tangent to body surface and free-stream direction
- γ Polytropic constant = $(\partial h/\partial e)_s$
- δ Skin thickness
- δ Boundary-layer thickness
- ϵ Depth of thermocouple
- θ Angle between normal to body surface and free-stream direction
- θ Momentum thickness
- κ Body-surface curvature
- μ Absolute viscosity
- ν Kinematic viscosity
- ρ Density

τ Shear stress or Reynolds stress

$$\phi = \int_0^1 (\rho / \rho_e)^{\frac{1}{2}} dz$$

Subscripts

- 1 Free-stream conditions ahead of shock
- A Stagnation-point condition
- e Local condition just outside boundary layer
- o Body-surface condition
- p Thermocouple location
- t2 Stagnation conditions behind normal shock
- T Transition conditions
- w Body-surface conditions



SUMMARY

The X-17 R-26 vehicle re-entered the atmosphere at a nominal velocity of 5000 ft/sec. Second- and third-stage thrust increased the velocity to a peak value of 13,300 ft/sec. As the vehicle descended from 90,000 to 46,000 ft., the Reynolds number, Re_{LD} , based on free-stream conditions and body diameter, ranged from 1.0 to 16.5 million.

Temperatures were measured at 23 locations on the nose, a 9-in. diameter, nickel-plated copper hemisphere. The surface of the nose was polished to a nominal 1/2-microin. rms surface finish, except for two narrow patches of 45-microin. rms roughness. These rough patches both covered a major thermocouple run. One patch started at the 20-degree body-angle location, while the other began at the 40-degree position. Data were also obtained on a smooth control run.

The results of the data analysis indicate that transition first occurred on the 45-microinch rms roughness runs at the 45-degree position. The transition front then moved forward on both thermocouple runs onto the polished portion of the nose to the 15-degree location. Transition occurred on the smooth control run about 1.5 seconds after transition was detected on the rough runs.

[The most significant fact observed on this flight was that roughness caused early transition but did not control the rate or extent of the subsequent forward movement of the transition front.]

INTRODUCTION

The Lockheed Missile Systems Division has been engaged in a research and development program in accordance with the provisions of Contract AF 04(645)-7. The purpose of this program is to obtain aerodynamic heating data during the re-entry of a ballistic vehicle into the atmosphere of the earth. An original program of twenty-five research flights was planned to obtain this data for various nose shapes over a range of Mach and Reynolds numbers. This program had been recently completed and the results obtained have been summarized in Reference 1. An additional flight was contracted for, after completion of the original program. This report documents Flight R-26, the twenty-sixth of the research flights.

The test vehicle is a Lockheed designed, three-stage ballistic missile. The tandem configuration consists of five solid-fuel rocket motors. A single XM-20 motor is used to power the first stage, and a cluster of three XM-19 motors is used for the second stage. The third stage is powered by a single XM-19E1 motor. Stability of first stage is obtained by a symmetrical arrangement of four tail fins. Second- and third-stage stability is achieved by flaring the aft end of each stage to form a truncated cone. The third stage contains the nose cone and telemeter package.

A more complete description for a typical vehicle, including general-arrangement and inboard-profile drawings, weight-and-balance and alignment summaries, and an instrumentation schedule, is given in Appendix A of Part I in Reference 2.

TRAJECTORY

The R-26 flight test was conducted 22 August 1957. The vehicle was launched from Cape Canaveral, AFMTC, Florida, at 1003 hours, EST. The launcher setting was 77.3° elevation and 75° azimuth. The existing winds produced a trajectory which was equal to a zero-wind launcher setting of 77.4° elevation and 88° azimuth.

Camera tracking data was obtained until the vehicle disappeared through a cloud layer at about 15,000 ft. altitude. Radar tracking data was obtained over the apogee of the trajectory to the first-stage-separation altitude of 93,500 ft. Ignition of the first-stage rocket was normal, and first motion occurred at 0.34 sec., AFMTC time.

Figure 1 presents the first-stage velocity, altitude, and range time histories, based on a computed extrapolation of the radar data. The expanded time history of the first-stage boost phase, Figure 2, indicates that the motor performance was normal and that a maximum velocity of 5100 feet per second was realized. Figure 3 contains the corresponding Mach-number and Reynolds-number time-histories. Atmospheric data obtained at launch were used to determine the Mach number and Reynolds number. The Reynolds number is based upon free-stream properties and the nose-cone diameter.

Separation of the first and second stages occurred at 93,500 ft. altitude at 309.86 sec. Velocity at the time of separation was 4,860 ft/sec.

Second-stage ignition occurred 0.74 sec. later at 90,500 ft. altitude. The second-stage configuration was accelerated to a velocity of 9,000 ft/sec. at 75,000 ft. altitude.

Third-stage ignition occurred satisfactorily 2.46 sec. after second-stage ignition. The final configuration was boosted to a peak velocity of 13,300 ft/sec. at 58,500 ft. altitude. Figure 4 contains the second- and third-stage velocity and altitude time histories. The corresponding Mach and Reynolds numbers are shown in Figure 5.

A summary of important events during the flight is given in Table I, below.

Table I
Summary Of Important Events

<u>Event</u>	<u>Time (sec.)</u>	<u>Velocity (fps.)</u>	<u>Altitude (ft.)</u>
First-to-second stage separation	309.86	4,860	93,500
Second-stage ignition	310.60	4,800	90,500
Third-stage ignition	313.06	9,000	74,200
Peak velocity	314.7	13,300	58,500

The longitudinal, normal, and lateral accelerations during re-entry are presented in Figs. 6 and 7. In the vicinity of third-stage burnout, 314.7 seconds, the normal and lateral accelerometer data (Fig. 7) show that the

~~SECRET~~

LMSD-2600

vehicle was pitching with an amplitude of about 3 degrees. The roll rate at this time was 2.3 cps. Four seconds after third-stage burnout, the angle of attack decreased to about one degree.

INSTRUMENTATION

The R-26 nose was a 9-in. diameter hemisphere. It was fabricated from high-purity, vacuum-melted copper (Cupro - Vac E, supplied by Vacuum Metals, Inc.) and plated with a thin layer of nickel. Thermocouple plugs were fabricated from OFHC copper.

Instrumentation consisted of 8 ultradyne pressure transducers and 23 chromel-alumel thermocouples. The detailed locations of pressure orifices and thermocouples are shown in Fig. 8. The thermocouples are given letter designations from A through W for reference in the remainder of this report. Table II lists the thermocouple locations, depths, and wall thicknesses. Pressure orifice locations are presented in Table III.

The thermocouple installation technique is described in Reference 2, Part II, Instrumentation Section.

Table II
R-26 Thermocouple Locations

Thermocouple	Angular Distance from Stagnation Point (Degrees)	
A	0	45-microinch rms roughness area beginning at 40°
B	15	
C	22.5	
D	30	
E	37.5	
F	45	
G	52.5	control run, 1/2-microinch rms
H	60	
I	67.5	
J	75	
K	30	
L	37.5	
M	45.0	45-microinch rms roughness area beginning at 20°
N	52.5	
O	15	
P	22.5	
Q	30	
R	37.5	
S	45	
T	52.5	
U	60	
V	67.5	
W	75	

Total wall thickness	0.755 in.	} After buffing
Depth of thermocouple junctions	0.025 in.	
Thickness of nickel plating	0.005 in.	

Table III
R-26 Pressure-Orifice Locations

Orifice	Angular Distance From Stagnation Point, (Degrees)
A	55
B	60
C	65
D	70
E	75
F	80
G	85
H	90

SURFACE FINISH

The R-26 nose was plated with 7 mils of nickel over a copper strike applied at 75 amperes per square foot for three minutes. Plating results were good, and the surface was buffed and polished with various grades of diamond compounds in the usual manner (Reference 3).

During the buffing operation, the nickel plate was completely removed in a small region (See Table IV, below), and it was necessary to replace the nickel using Dalic electroplating procedure. The deepest pit on the instrumented surface was 60 microinches deep. All defects of depth greater than 20 microinches are listed below in a polar coordinate system defined as distance from the stagnation point in inches, and degrees counter-clockwise from the +Z axis looking aft. The general surface finish as inferred from interferograms was about 1/2 microinch rms.

After the polishing operations were completed, two roughness patches were made on the surface. Both patches were approximately 45 microinches rms and covered the two major thermocouple runs. An 80 TP carborundum abrasive was used to roughen the patches. The patch covering thermocouple run A-J began 40 degrees aft of the stagnation point, and the other began at the 20-degree position. Other details about the roughness areas are indicated in Fig. 8.

Table IV

List Of Surface Defects

Defect	Distance	Degrees	Diameter (mils)	Depth (microin.)
Pit	0.6	105	3	15
Pit	0.7	250	3	50
Pit	1.2	40	5	60
Pit	1.4	150	2	20
Pit	1.9	120	3	20
Pit	2.1	240	4	30
Pit	2.2	15	7	50
Pit	3.3	325	5	25
Dalic Patch				
-Nickel Interface	3.9	70	1-1/2 in. sq.	20-30
Pit	4.3	335	8	50

TELEMETRY AND DATA REDUCTION

Nose temperature data on the R-26 flight were monitored on telemeter channel 16. The general quality of the data was not as good as on previous flights, due possibly to a dirty or worn commutator. Although nose temperature data were obtained to approximately nine seconds after third-stage burnout, the data were reduced only up to 321 seconds (approximately 6.5 seconds after third-stage burnout).

The actual temperature data are presented in Figs. 10 to 32. Automatic decommutation of the data was possible up to 312 seconds. Between 312 and 321 seconds the data were manually decommutated.

Thermocouples R, S, T, U, and V yielded questionable temperature data beginning between 316 and 318 seconds, as seen in Figs. 27 to 31.

Nose static pressure measurements were obtained on channel 14. Due to in-flight calibration shifts, the data are believed to be accurate to only 1.5 percent of total bandwidth. The actual pressure data during re-entry are presented in Figs. 55 to 63.

THERMOCOUPLE DATA-SMOOTHING TECHNIQUE

The commutated thermocouple data contain a certain amount of scatter, which would produce erratic heat rates if used as reduced. Therefore, in order to solve the transient heat-conduction problem for each thermocouple location, it is necessary to first smooth the data.

The data-smoothing technique uses a second-degree, least-squares, "walking" polynomial. A least-squares parabola is fitted to nine consecutive data points, and the center value of the parabola is taken as the smoothed data point. The polynomial is then advanced along the raw data by dropping one data point and adding a new one. The procedure is repeated to obtain additional smoothed points. Details of the data-smoothing technique are given in Appendix A of Reference 2.

METHODS OF ANALYSIS

The state of the boundary layer at each thermocouple location during re-entry is determined primarily from a comparison of the observed heat rates with laminar and turbulent predictions. The observed heat-transfer and temperature distributions over the surface are also examined for evidence of transition.

The laminar and turbulent heat-transfer predictions were made for the measured trajectory using the Rocket-Panel atmosphere (Reference 4) and actual nose temperature data. The laminar heat-transfer rates were predicted from the AVCO stagnation-point theory (Reference 5) for an equilibrium boundary layer with Prandtl number 0.71 and Lewis number 1.4. The Bromberg-Lees theory for the distribution of laminar heat transfer (References 6 and 7) was used. Turbulent heat rates were computed from the theory by Denison (Reference 8), which extended Van Driest's procedure (Reference 9) to blunt bodies at hypersonic speeds and also by a method developed by Bromberg, Fox, and Ackermann (Reference 10).

Application of the boundary-layer theories requires a knowledge of the inviscid flow field outside the boundary layer. The inviscid flow was determined by combining the Newtonian and Prandtl-Meyer pressure distributions and assuming isentropic expansion from the stagnation point. The

Prandtl-Meyer flow was matched to the Newtonian pressure distribution at a point where the pressure and derivative of pressure with respect to angle are identical, as suggested by Lees. A specific heat ratio of 1.4 for the Prandtl-Meyer expansion was found to give good agreement with measured pressures on previous flights. The heat-transfer predictions and momentum-thickness Reynolds numbers contained in previous reports on hemispherical nose shapes (References 11, 12, 13, 14) were based upon a Newtonian pressure distribution over the entire body. The modifications introduced by the new method into the significant parameters such as q/q_A , \tilde{Re}/Re_{1R} , η , $\rho_e u_e/\rho_1 u_1$, and $\tilde{Re}_{wt}/Re_{1R} (\mu_w/\mu_1) (T_w/T_1) (1/F_1)$ are shown in Figures 65 to 69. Differences are introduced at body angles greater than about 55° .

The observed heat rates were deduced from the temperature data by solving the transient heat-conduction problem. A one-dimensional analysis in which constant thermal properties were assumed was made at each thermocouple location. This method neglects the effects of lateral conduction and curvature of the surface. However, the large temperature gradients across the skin which occur during re-entry are accounted for.

A two-dimensional, constant thermal-property analysis was made for thermocouple positions A through I and O through V on the two major thermocouple runs. This procedure assumes axial symmetry but takes account of lateral conduction and curvature of the surface. Details of the above methods are presented in Appendices E and G of Reference 2. The constants used in the heat-transfer analyses described above were:

Exit

Thermal diffusivity, $\alpha = 0.00114 \text{ ft}^2/\text{sec.}$

Thermal conductivity, $k = 0.0603 \text{ BTU/sec-ft. } ^\circ\text{F.}$

Re-Entry

Thermal diffusivity, $\alpha = 0.000924 \text{ ft}^2/\text{sec.}$

Thermal conductivity, $k = 0.0555 \text{ BTU/sec-ft. } ^\circ\text{F.}$

These represent mean values of the Armour and Battelle measurements (References 15 and 16) for the two temperature ranges.

At the stagnation point a one-dimensional analysis was made, including the effects of variable thermal properties. The details of this method are described in Reference 1. The variation of thermal properties of the copper were described by the following expressions:

$$k = 0.062 - 6.2 \times 10^{-6}T \text{ (BTU/ft}^2 \text{ - sec } ^\circ\text{F/ft.)}$$

$$\rho c = 51.2 + 5.31 \times 10^{-3}T \text{ (BTU/ft}^3 \text{ - } ^\circ\text{F).}$$

(T is in degrees Fahrenheit.)

DISCUSSION OF RESULTS

GENERAL OBSERVATIONS

The R-26 flight was the fourth Lockheed X-17 research flight which had as its purpose the determination of the effect of controlled surface roughness on transition Reynolds number. The R-26 experiment was designed to clarify the effects of surface roughness. The nose was equipped with two roughness patches of equal magnitude but different length. The magnitude of the roughness was set at 45 microinches rms in order to provide a more severe test of roughness than on previous flights.

The basic reason for making the patches of different length was to determine if transition was so completely roughness-dominated that the turbulent flow region would exist initially only in roughened areas. For example, if transition should occur on both rough runs and exist only as far forward as the start of each run, it could be fairly concluded that transition was highly roughness sensitive.

The total extent of the roughness area on initiating transition was another effect which the different-length runs were designed to investigate.

As on previous flights, a control run of thermocouples was provided to supply the fundamental comparison of transition in rough and smooth areas.

Review Of Previous Results

The R-9, R-11, and R-22 flights previously demonstrated the feasibility of conducting surface roughness experiments with a narrow patch of controlled

roughness on the nose cone while simultaneously maintaining smooth control areas for "natural" transition results. The magnitude of the surface roughness used on the various flights are listed below.

Surface Roughness Experiments With Hemispheres

Flight	Roughness (Microinches rms)
R-9	30
R-11	6
R-22	20 and 6 (two patches)
R-26	45 (two patches)

Before discussing the results obtained on Flight R-26, it will be helpful to review the transition events on the previous flights.

Flight R-9

On flight R-9 transition occurred at almost the same instant at all thermocouples between 20 and 90 degrees on the 30-microinch-rms roughness patch. Transition did not occur on a smooth thermocouple run located 180 degrees circumferentially from the roughness patch at all times that data were obtained. About 1 second after transition originated on the rough patch, turbulent flow was observed on two secondary thermocouple runs which were located 90 degrees circumferentially from the 30-microinch patch. The momentum-thickness Reynolds number at the 20-degree position on the roughness patch was 180, the lowest observed in the RTV program.

Flight R-11

Transition occurred almost instantaneously on the 6-microinch-rms roughness patch between 50 and 70 degrees. No forward movement of the transition front beyond the 50 degree position was observed, since data were lost prematurely at the 40-degree location and the flow was apparently laminar at 30-degrees.

Transition also occurred on the control run at body angles of 70 and 90 degrees at practically the same time transition took place on the 6-rms run, and subsequently moved forward to the 60-degree position.

Laminar flow was observed on two short thermocouple runs which covered body angles between 20 and 50 degrees.

The value of the momentum-thickness Reynolds number on the 6-microinch run at the 50-degree position at the time of transition was 550.

Flight R-22

Transition originated on the aft end of the 20-microinch-rms run and moved forward to the 22.5-degree location during an interval of 1.5 seconds. The transition data obtained on the 6-microinch rms roughness run were questionable because of the fact that the heat rates were neither clearly laminar nor turbulent. About 1 second after it originated on the 20-microinch-rms roughness run, turbulent flow occurred on a smooth control run located midway between the two roughness patches. As transition moved forward on the 20 rms run from 52.5 degrees to 22.5 degrees, the momentum-thickness Reynolds number at the point of transition ranged from 420 to 280.

R-26 Transition Results

Transition from laminar to turbulent flow was detected on both roughness patches between 314.2 and 314.4 seconds. Transition initially occurred almost instantaneously on both rough runs at all locations aft of 45 degrees. The heat-rate data and the temperature levels both indicate that transition may have started slightly earlier on the longer roughness patch than on the shorter one.

The turbulent front on both roughness runs then moved forward to the 15-degree position by 316.9 seconds. The short and long roughness runs started at the 40- and 20-degree body positions respectively. Hence, surface roughness did not control either the extent or rate of the forward movement of the transition front.

Transition was detected on the control run approximately 1.5 seconds after it first appeared in the rough areas. All thermocouples on the control run showed transition practically simultaneously.

The minimum momentum-thickness Reynolds numbers when transition was initially detected on the rough and smooth runs were 350 and 370 respectively. After the transition front moved to the 15-degree body location, the momentum-thickness transition Reynolds number was approximately 200.

A more detailed discussion of the R-26 transition events is presented under 'Behavior of Transition Parameters' in this section. A summary of the R-26 transition events is given in Table V.

In Table VI the conditions on the R-26 nose at the time of transition are compared to those on previous flights which used the hemispherical nose shape.

Table V
Summary Of Transition Events

Thermocouple run	Surface Finish (Microin. rms)	Time When Transition Was First Detected (Sec.)	Body Angle Where Transition Was First Detected (Deg.)	Foremost Point of Transition (Deg.)	Comments
A-J	45, starting at 40° body position	314.4	45	15	Transition moved forward over a 2.5 sec. interval.
K-N	1/2	315.9	30	30	The most forward thermocouple was located at 30°.
O-W	45, starting at 20° body position	314.4	45	15	Transition moved forward over a 2.5 sec. interval.

TABLE VI
CONDITIONS ON HEMISPHERES AT TRANSITION

Flight	R-2	R-8	R-9	R-11	R-22	R-22	R-26	R-26
Surface finish at time of launch (μ inches rms)	2	1/2	30	6	20*	6	45	1/2
Free-stream Reynolds number, Re_D	19.3×10^6	11.5×10^6	7.8×10^6	14.2×10^6	6.5×10^6 14.5×10^6	16.5×10^6	5.4×10^6 16.5×10^6	15×10^6
Free-stream Mach number, M_1	12.1	10.6	12.6	11.6	9.4-11.0	11.3	9.7-13.4	12.4
Altitude (ft.)	38,060	46,500	59,500	45,500	55,500-12,000	40,000	37,000-62,000	57,000
Average temperature in subsonic region ($^{\circ}F$)	1100	600	850	700	340-660	870	800-1650	1200
Average boundary-layer cooling, h_v/h_e	0.13	0.12	0.10	0.12	0.13	0.13	0.09	0.09
Momentum thickness at stagnation point (μ inches)	600	740	930	690	955-670	630	--	--
Ratio of rms roughness to boundary- layer momentum thickness, δ/θ	--	--	0.031	0.0073	0.012-0.0275	0.0034**	0.03-0.07	--
Maximum laminar momentum thickness Reynolds number observed after transition, Re_{θ}	410	230	180	550	275	760**	200	370
Acceleration (G)	Approx. Zero	+65	+80	+62	Zero to +60	+65	+72 to -70	-70
Angle of attack (degrees)	At least 2.5°	3 to 10°	At least 4°	2.5°	0° to 8°	8°	0° to 3°	3°

* Transition crept forward on this run, hence a range of conditions were encountered

** Questionable data. In addition, transition may also have occurred at other thermocouple locations on this run. (See text)

Effect Of Surface Roughness On Transition

Without discussing transition Reynolds number or other transition parameters, but confining attention only to the physical events which occurred during re-entry, the R-9, R-22, and R-26 results show quite conclusively that the surface roughness which was present (20-45 microin. rms) caused premature transition. On each of these flights considerably higher heat rates and surface temperatures were observed in roughened areas than in smooth areas.

The results obtained from the 6-microinch rms surface on the R-11 and R-22 flights indicated that roughness of this magnitude did not cause early transition. Hence, for the boundary-layer conditions encountered in the X-17 series, a rough dividing band for surface-roughness effects appears to be established.

When reviewed in the above manner, the results from the roughness experiment seem quite clear. However, when attempts are made to correlate the data from the various flights by comparing transition Reynolds numbers, the results become somewhat obscured. In the past flight reports the momentum-thickness Reynolds number at the point of transition has been used as a correlation parameter. When the transition Reynolds numbers from all the X-17 flights are compared, it is found that independently of whether the surface is rough or smooth, Re_{θ_T} covers the same range. This indicates, therefore, that Re_{θ} is probably not the best choice for a correlation number, since it tends to obscure the physical facts.

The above fact is clearly illustrated in Fig. 9, which summarizes the minimum free-stream transition Reynolds number and the corresponding

Re_{θ_T} 's obtained on hemispheres. The minimum value of Re_{θ_T} does not occur at the minimum free-stream transition Reynolds number since Re_{θ} is a function of body position.

Transition occurred on the R-9, R-22, and R-26 roughness patches at a much lower free-stream Reynolds number than on the smooth surfaces and on the 6-microin. rms patch on the R-11 flight. The Re_{θ_T} 's obtained on the same roughness patches, however, fall into the same band as those obtained on the smooth surfaces. One reason for this behavior is that at high Mach numbers the momentum-thickness Reynolds number is almost proportioned to the square root of the free-stream Reynolds number at a given body position.

Another reason is that the momentum-thickness Reynolds number at transition is also highly dependent on the body location at which transition is detected. As an example, on flight R-11 transition occurred at practically the same time in the trajectory on both the smooth run and the 6-microinch rms roughness run, but the transition momentum-thickness Reynolds numbers were 720 and 550, respectively. This is because transition occurred at the 70-degree location on the smooth run and at the 50-degree location on the roughness patch.

The free-stream Reynolds number, however, which is independent of the body location, demonstrates quite clearly that surface roughness causes early transition.

RE-ENTRY TEMPERATURE DATA

The raw temperature data obtained during re-entry are presented in Figs. 10 to 32. Points which were discarded in the computations are indicated.

An examination of the data at thermocouple D indicates that the thermocouple probably malfunctioned and that the data, therefore, are not valid. As indicated in the table below, the temperatures registered by thermocouple D were several hundred degrees lower than those indicated by neighboring thermocouples.

Time	Temperature (°F)		
	C	D	E
315	1100	650	1000
315.5	1320	830	1300
316	1470	1000	1560

The temperature distributions along the surface of the nose at various times during re-entry are shown in Figs. 33 and 34. The data were smoothed by hand to obtain values for these figures. The temperature profiles on the two major thermocouple runs, Fig. 33, indicate laminar flow to approximately 314.5 seconds. By 315 and 315.5 seconds there is clear evidence of transition on both runs at thermocouples aft of 50 degrees. At later times the temperature profiles on both runs are still roughly similar, although consistently higher temperatures are recorded along run O-W in regions where the flow was turbulent.

At 317.0 seconds temperatures in excess of the melting point of copper were indicated by thermocouples S, T, and U. It is of interest to note that at 317.0 seconds the nose internal pressure shows a discontinuous jump to higher levels (See Fig. 63). These events suggest the possibility

that shortly after the melting point was reached a hole was burned through the nose, increasing the internal pressure in the nose. If this actually did occur, it would not have had any influence on the results of the experiment, since the transition events as well as the major portion of the heating were completed before 317.0 seconds.

The raw temperature data obtained from thermocouples K, L, M, and N in the short control run show distinct changes in slope at about 316 seconds, indicating transition. The corresponding temperature profiles are shown in Fig. 34. The profile obtained from thermocouples located beneath the largest roughness patch are included in this figure for comparison. The data show quite clearly that considerably more turbulent flow occurred on the rough patch than on the smooth control run.

RE-ENTRY HEAT RATES

The heat-rate plots for re-entry are presented in Figs. 35 through 44. Observed heat rates are compared with laminar and turbulent predictions. Observed heat rates obtained by a two-dimensional analysis are presented for the majority of the thermocouples comprising the two roughness runs.

The heat rates are discussed below by comparing results at each geometrical location. The location is identified by the angle between a normal to the surface and the free-stream direction. Reference should be made to the drawing of the nose (Fig. 8) and the list of thermocouple locations in Table II.

Thermocouple A, 0° (Figure 35)

At the stagnation point a one-dimensional heat-conduction analysis was made to obtain the observed heat rates for the two cases of variable and constant thermal properties. For the variable thermal-properties case, the variation of the nose-cone thermal properties with temperature is given in the 'Methods of Analysis' section.

Accounting for the variable thermal properties decreases the observed heat rates by about 10 percent in the vicinity of peak heating.

A two-dimensional constant thermal-properties analysis was also made at the stagnation point to obtain the observed heat rates. The two-dimensional analysis, which accounts for body-curvature effects and lateral conduction, yields observed heat rates about 12 percent below those obtained by a one-dimensional analysis.

If it is assumed that the effects of variable thermal properties are the same for a one- and two-dimensional analysis, the observed heat rates obtained by a two-dimensional variable thermal-properties solution can be estimated. This estimated observed heat rate, shown as a broken line in Fig. 35, is between 10-15 percent higher near peak heating than the laminar prediction.

Thermocouples B And O, 15° (Figure 36)

The observed heat rates at thermocouples B and O are in good agreement with each other at all times data were obtained. The laminar prediction is about 25 percent below the observed heat rates in the neighborhood of peak heating.

A comparison of the observed heat rates at this location with those at the stagnation point indicate that the boundary layer was laminar at the time of peak heating. The heat rates indicate that transition occurred at both thermocouple locations between 316.8 and 317.0 seconds.

Thermocouples C And P, 22.5° (Figure 37)

The observed heat rates at thermocouple C and P are in good agreement with each other. The laminar prediction at this location also underestimates the observed heat rates.

At this and subsequent locations, two turbulent predictions are shown. One is due to Denison (Reference 8) and the other is due to Bromberg, Fox, and Ackerman (Reference 10). The latter is referred to as the R-W prediction for convenience. Transition to turbulence is indicated at both thermocouple locations between 316.4 and 316.7 seconds. The turbulent heat rates are slightly higher than the R-W prediction, which is in turn slightly above the Denison turbulent prediction.

Thermocouples D, K, And Q, 30° (Figure 38)

A two-dimensional analysis was performed at thermocouple Q only. The temperature data at thermocouple D is questionable, as pointed out in the discussion of re-entry temperatures, and was eliminated in the two-dimensional analysis of thermocouple run A-J since they would affect the results at the neighboring thermocouples. On the short control run, K-N, there were an insufficient number of thermocouples to perform a satisfactory two-dimensional analysis.

A comparison of the heat rates at thermocouple Q and the preceding location indicate that transition occurred sometime after 314.3 seconds. The heat rates after this time are considerably less than both turbulent predictions and much higher than the laminar prediction, which suggests the possibility that the boundary layer was in transition. After 317 seconds the observed heat rates fall between the two turbulent predictions, indicating fully developed turbulent flow.

Transition occurred at thermocouple K on the control run between 316.0 and 316.4 seconds, considerably more than one second after transition had occurred at thermocouple Q, which had a 45-microin. rms roughness surface. During the time the flow was laminar at thermocouple K, the laminar prediction underestimated the observed heat rates. After transition the observed heat rates at K were higher than both turbulent predictions.

Since the heat rates at thermocouple D are questionable, they will not be discussed.

Thermocouples E, L, And R, 37.5° (Figure 39)

The observed heat rates at thermocouples E and L are in good agreement with each other at early times. The observed heat rates at thermocouple R are somewhat below those at E and L. The laminar prediction is in fair agreement with the observed heat rates at these times.

Transition occurred first at thermocouple R sometime after 314.4 seconds. The boundary appears to have been in transition until about 316.4 seconds, when the observed heat rates begin to agree very closely with the turbulent prediction of Denison.

Transition occurred at thermocouple E at about 315 seconds and between 315.7 and 315.9 seconds at thermocouple L. The turbulent observed heat rates at E lie between the two turbulent predictions, while those at L are somewhat higher than both turbulent predictions.

Thermocouples F, M, And S, 45° (Figure 40)

The observed heat rates at early times oscillate about the laminar prediction. Transition occurred at thermocouples F and S at approximately 314.4 seconds. It appears that transition occurred at thermocouple S slightly before thermocouple F. Transition occurred at thermocouple M on the control run at about 315.9 seconds, considerably after transition occurred at the two thermocouples located on the roughness runs.

After 316.8 seconds, the observed turbulent heat rates are in fair agreement with the turbulent predictions. Thermocouple F is in good agreement with the Denison prediction, while thermocouple M is in fair agreement with the R-W prediction. In other words, the spread in the data was just about equal to the spread in the two predictions.

Thermocouples G, N, And T, 52.5° (Figure 41)

Before 314.4 seconds the observed heat rates at the three thermocouple locations oscillate about each other and are, on the average, above the laminar prediction. Transition occurred at thermocouples G and T, located on the roughness runs, at about 314.4 seconds. Transition at thermocouple N, located on the control run, occurred at 315.9 seconds.

The turbulent heat rates fall between the two turbulent predictions. Valid temperature data at thermocouple T was prematurely lost just before 316 seconds.

Thermocouples H And U, 60° (Figure 42)

The observed heat rates indicate that transition occurred at thermocouple U at approximately 314.2 seconds and at 314.5 seconds at thermocouple H. Immediately after transition the observed heat rates oscillated between the two turbulent predictions. At later times the observed heat rates at thermocouple H agreed very well with Denison's turbulent prediction. Valid data was prematurely lost at thermocouple U, and no real comparison can be made with the turbulent predictions.

Thermocouples I And V 67.5° (Figure 43)

Transition occurred at thermocouples I and V between 314.3 and 314.5 seconds. Transition occurred slightly earlier at V than at I. The turbulent observed heat rates at thermocouple V oscillate between the two turbulent predictions. The turbulent heat rates at thermocouple I are of questionable validity after 315.4 seconds. Before 315.4 seconds the observed heat rates cross the band of the two turbulent predictions.

Thermocouples J And W 75° (Figure 44)

At early times the observed heat rates obtained by a one-dimensional analysis oscillate about each other. The average values of the heat rates

are higher than the laminar prediction. Transition appears to have occurred at thermocouple W shortly after 314 seconds and at approximately 314.4 seconds at thermocouple J.

The observed heat rates after transition are slightly higher than the R-W prediction. A two-dimensional analysis will lower the observed heat rates and improve the agreement between the observed and predicted heat rates.

The non-dimensional heat-transfer distributions during re-entry are shown in Figs. 45 and 46. On thermocouple run B-J transition is clearly indicated at 315 seconds at the 37.5-degree location. By 317.2 seconds the transition front had moved forward to the 15-degree location. Transition is also indicated on run O-W at 314.5 seconds at the 37.5-degree body location. The transition front then moved forward to the 15-degree location by 317.2 seconds.

On the control run (Fig. 46) transition is indicated at 316.5 seconds at the 30-degree location.

Before transition occurred, the heat rate distributions on all three thermocouple runs scatter about the high Mach-number laminar prediction.

BEHAVIOR OF TRANSITION PARAMETERS

The transition times, momentum-thickness Reynolds numbers, and values of δ/θ on the roughness runs at transition are shown in Fig. 47. It is seen that transition first occurred practically simultaneously at thermocouple locations between 45 and 75 degrees on the two roughness runs at approximately 314.4 seconds. The momentum-thickness Reynolds number at the 45-degree location at this time was 350. The 45-degree location is in the roughened area of both runs. Transition appears to have occurred slightly earlier on thermocouple run O-W, which had the longest roughness run, than on thermocouple run A-J. The transition front then moved forward on both runs well into the polished region to the 15-degree body location. The momentum-thickness Reynolds number at the 15-degree location at this time was 200. The extent of the roughness areas did not control the forward movement of the transition front.

Transition appeared simultaneously on the entire control run, thermocouples K-N, approximately 1.5 seconds after transition was first detected on the two roughness runs. The momentum-thickness Reynolds number at the most forward thermocouple location on this run (30-degree location) at the time of transition was 370.

A comparison of the transition results from the rough and smooth runs shows that roughness caused transition to occur earlier in the trajectory but with no significant change in the momentum-thickness Reynolds number. It should be pointed out, however, that the smooth control run was not

completely instrumented, as thermocouples were located only between the 30- and 52.5-degree body locations. It is possible that the transition front was well ahead of the 30-degree location when transition was detected on the control run, and this would result in a significant decrease in the transition Reynolds number.

A qualitative picture of the cooling experienced by the boundary layer is obtained from the ratio of the wall enthalpy to the local free-stream enthalpy. This ratio is presented as a function of time at several thermocouple locations in Fig. 48. A cross plot of Fig. 48 is presented in Fig. 49. Transition began when this ratio was at an average of about 0.09.

EXIT TEMPERATURES, REYNOLDS NUMBER, AND ACCELERATIONS

The magnitude of the temperatures during the exit trajectory is generally low in comparison to the total bandwidth of the telemetering channel; hence, the accuracy of the data is limited by resolution errors.

The quality of the exit-temperature data was below average on this flight. A typical temperature-time history during exit is shown in Fig. 50. Temperature profiles on the nose during exit are shown in Figs. 52 and 53. The exit heat rates obtained by fairing the raw temperature data and a thin-skin analysis are of doubtful validity and are not presented.

The temperature profiles on the two major roughness runs (Fig. 52) indicate that transition occurred early in the exit trajectory at the 30-degree body location. On thermocouple run O-W the temperature profiles indicate a forward movement of the transition front to the 15-degree

location. It should be pointed out that this apparent forward movement of the transition front took place while the momentum-thickness Reynolds number was decreasing. This can be seen by an examination of the momentum-thickness Reynolds-number history during exit, presented in Fig. 54.

The temperature profiles on the smooth control run (thermocouples K-N) indicate that transition occurred at the 30-degree body location late in the exit trajectory when the Reynolds number had decreased to a value well below its maximum.

The longitudinal accelerations experienced during exit are presented in Fig. 51. A maximum acceleration of approximately 12g's was obtained at 23.4 seconds. The normal and lateral accelerations, which are not presented, were no more than 1g.

PRESSURE MEASUREMENTS

Pressure measurements were made at 5-degree intervals at body angles of 55 to 90 degrees. Pressures were measured with respect to the pressure inside the nose cone, which was monitored separately by an absolute pressure gage. Gage pressure measurements were converted to absolute pressures by adding the nose internal pressure.

The actual pressure data during re-entry are shown in Figs. 55 to 63. These data were used in combination with the trajectory information (altitude and velocity) and an NACA standard atmosphere to compute the ratio of the measured static pressure at each orifice location to the stagnation pressure.

This pressure ratio, which is nearly independent of Mach number at high Mach numbers, is plotted as a function of body angle in Fig. 64 and compared with the following predictions:

1. Modified Newtonian law for high Mach numbers

$$\frac{P}{P_{t2}} = \cos^2 \theta.$$

2. Combination of modified Newtonian and Prandtl-Meyer pressures with $\gamma_e = 1.4$. The Prandtl-Meyer flow is matched to the Newtonian law at a point where value and derivative of pressure with respect to angle are identical.

The results are presented in Fig. 64, which shows that the data are in good agreement with both prediction methods (which are nearly equal) between 55 and 65 degrees. At larger body angles the modified Newtonian law falls below the data by increasing amounts, while the combined Newtonian -- Prandtl Meyer prediction overestimates the data slightly. It should be pointed out that the raw data in the time interval from 317 to 318 seconds contained oscillations which were faired to obtain the results shown on Fig. 64. It is of interest to note that although the nose internal-pressure data showed a sharp jump at 317.0 seconds the data obtained after this time correlated just as well as earlier data.

The result that the pressures at body angles greater than 65 degrees follow the combined Newtonian -- Prandtl-Meyer law better than the Newtonian law alone was also obtained on previous X-17 flights (Reference 1.)

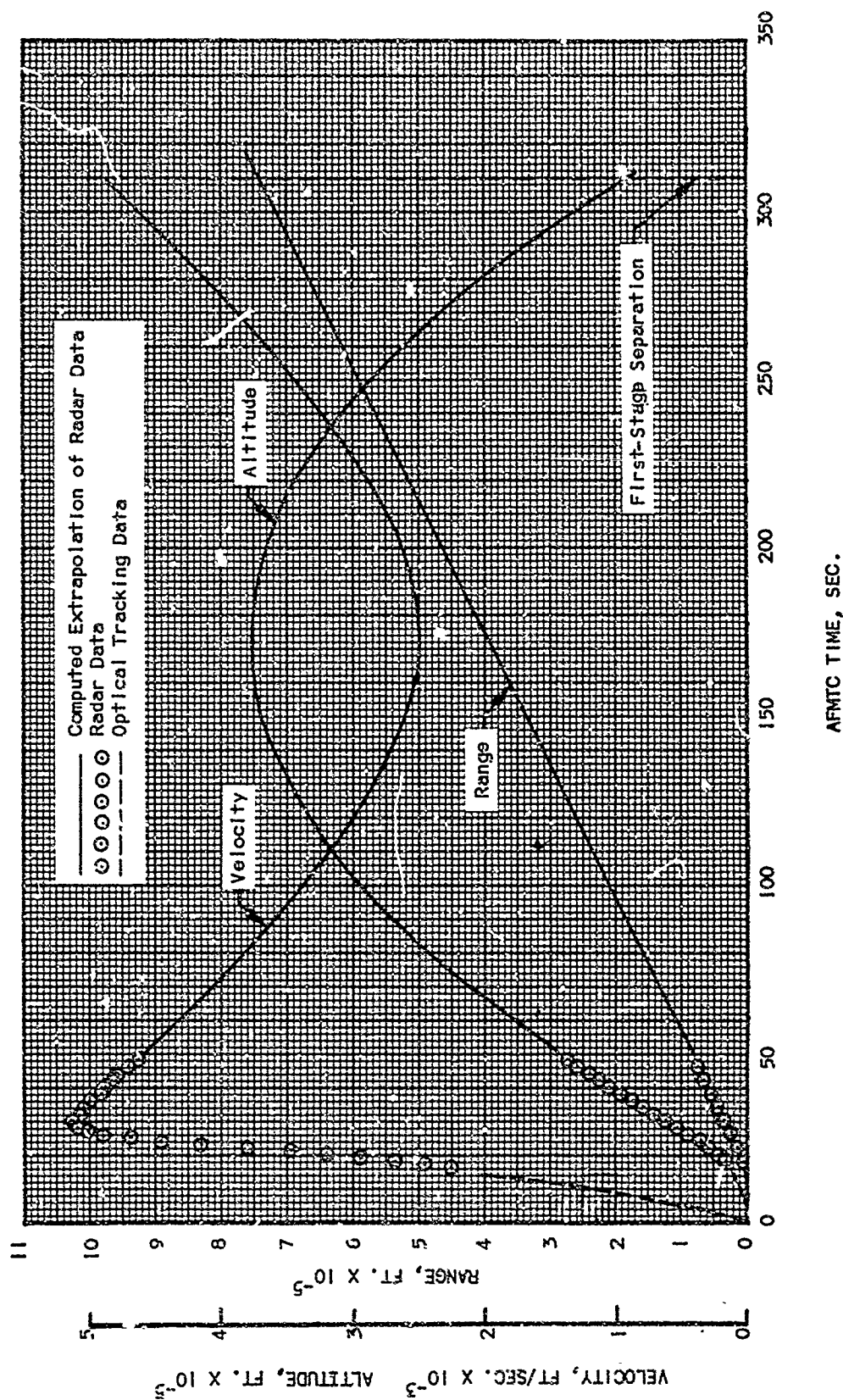


Fig. 1. R-26 Flight Trajectory, First Stage

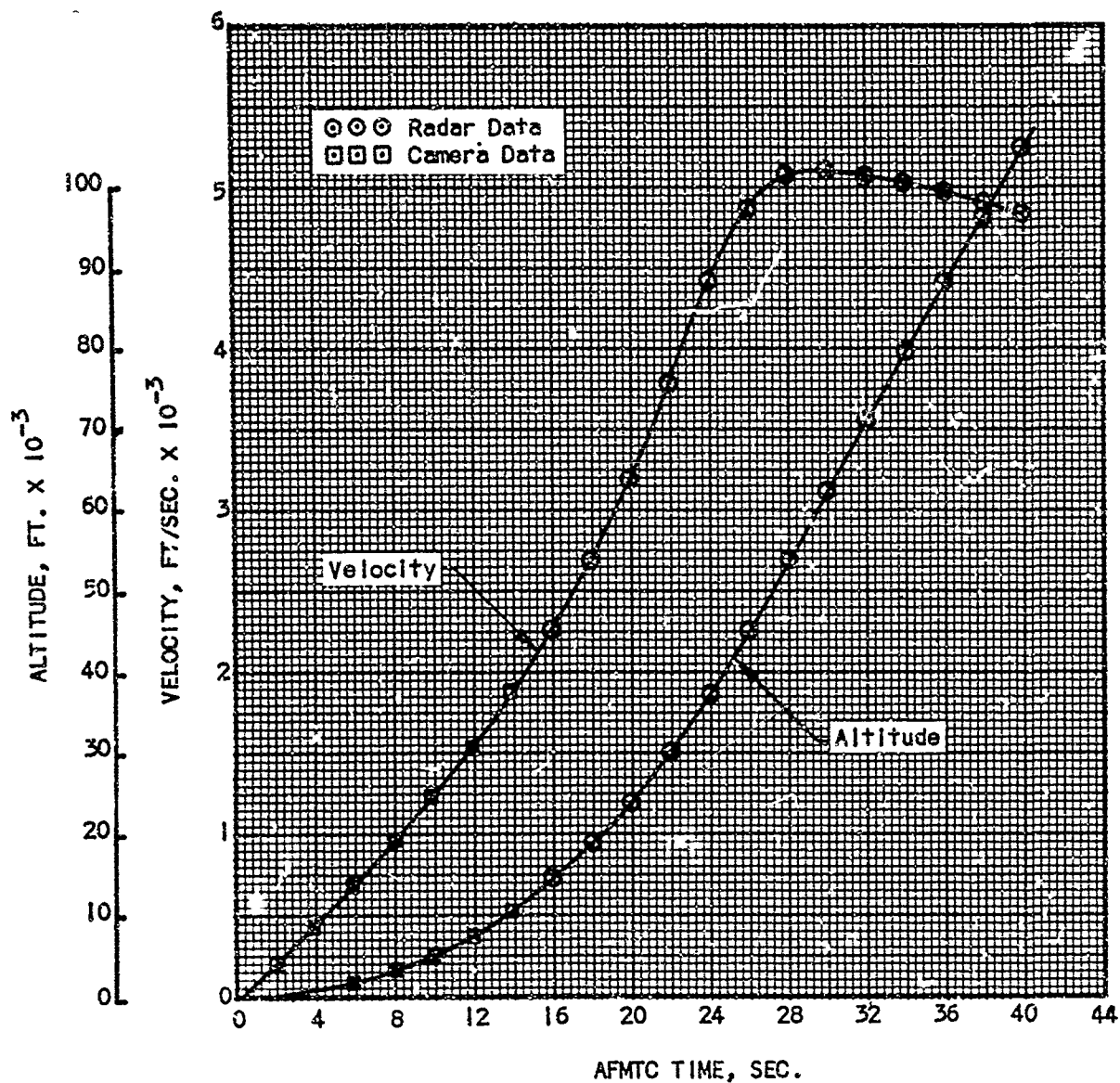


Fig. 2. R-26 Velocity and Altitude Histories, First-Stage Boost

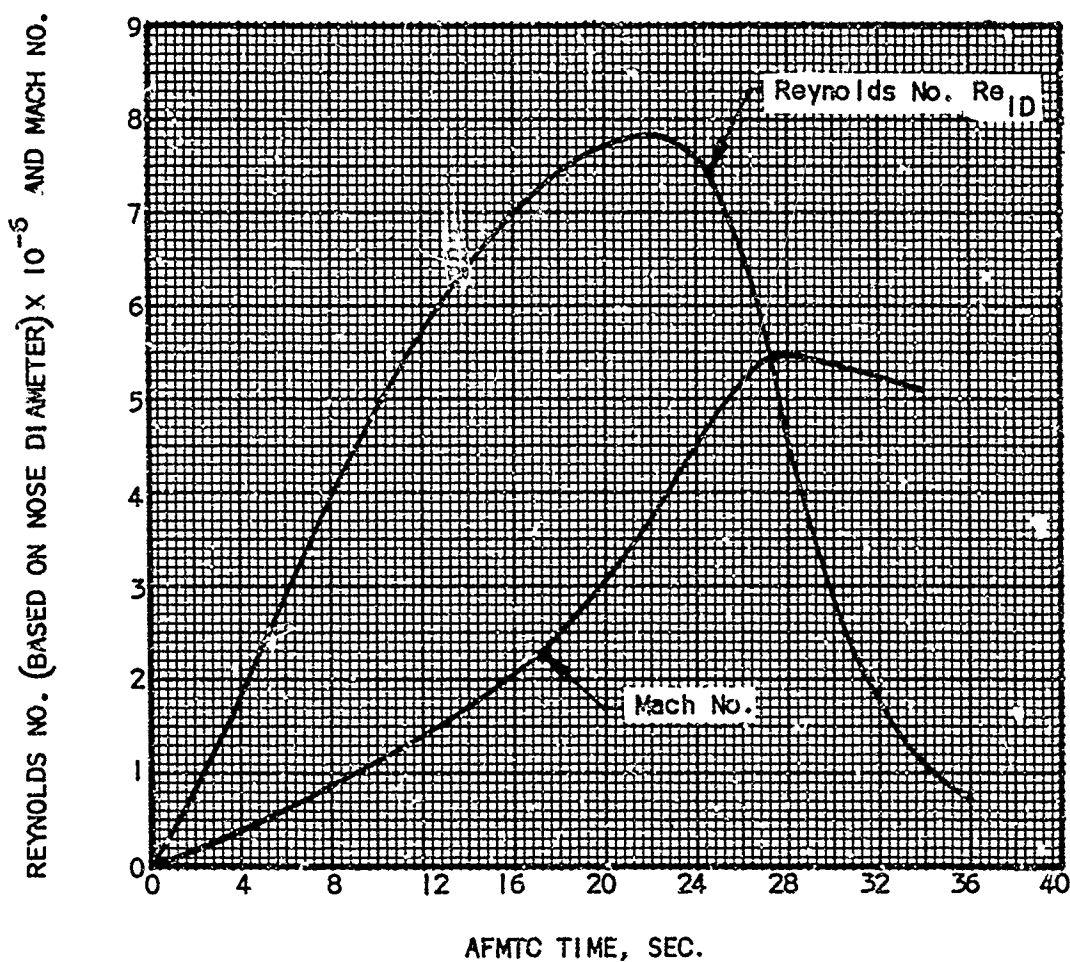


Fig. 3. R-26 Reynolds-Number and Mach-Number Time Histories during First-Stage Boost

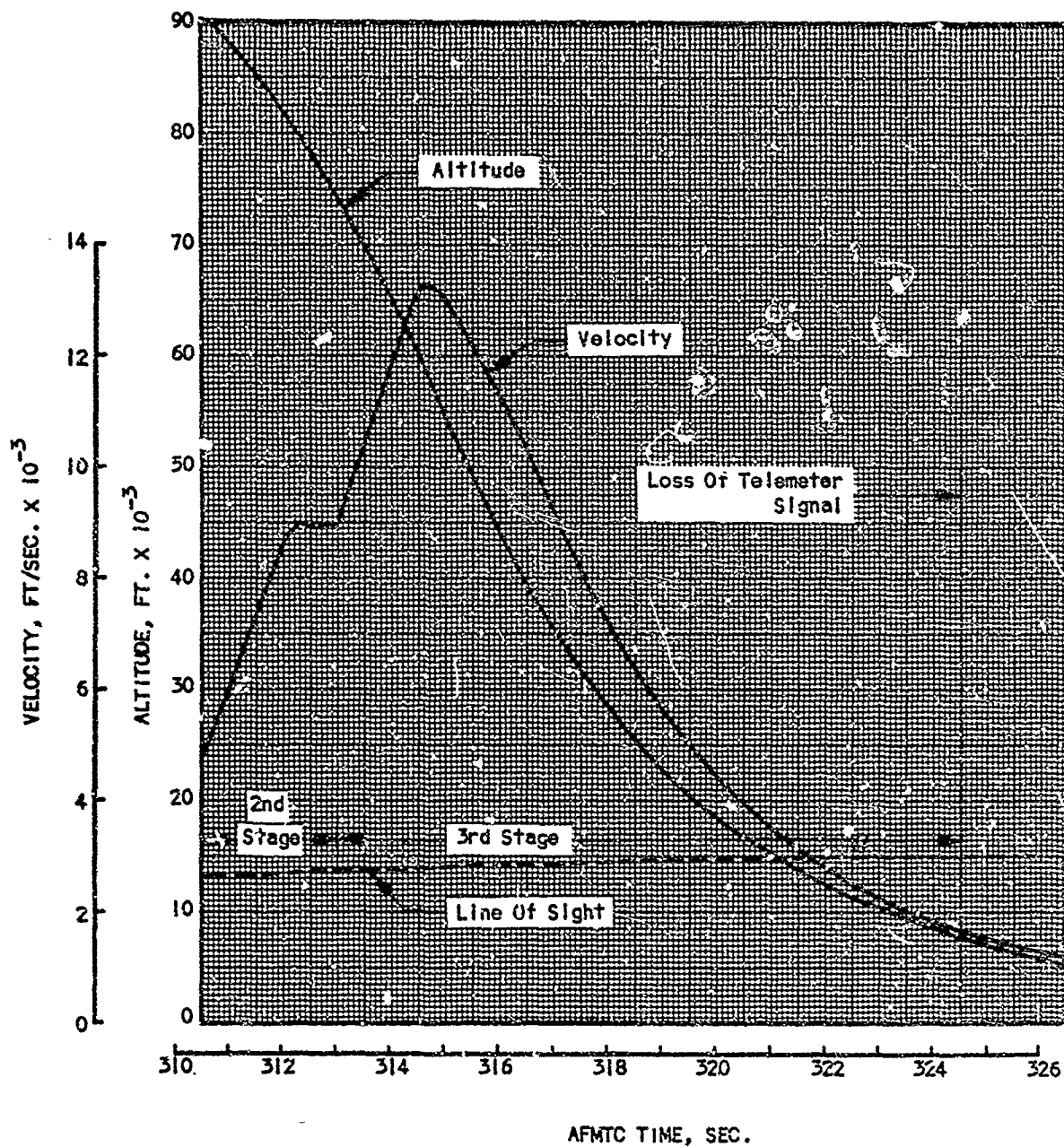


Fig. 4. R-26 Velocity and Altitude Time Histories, Second- and Third-Stage Boost

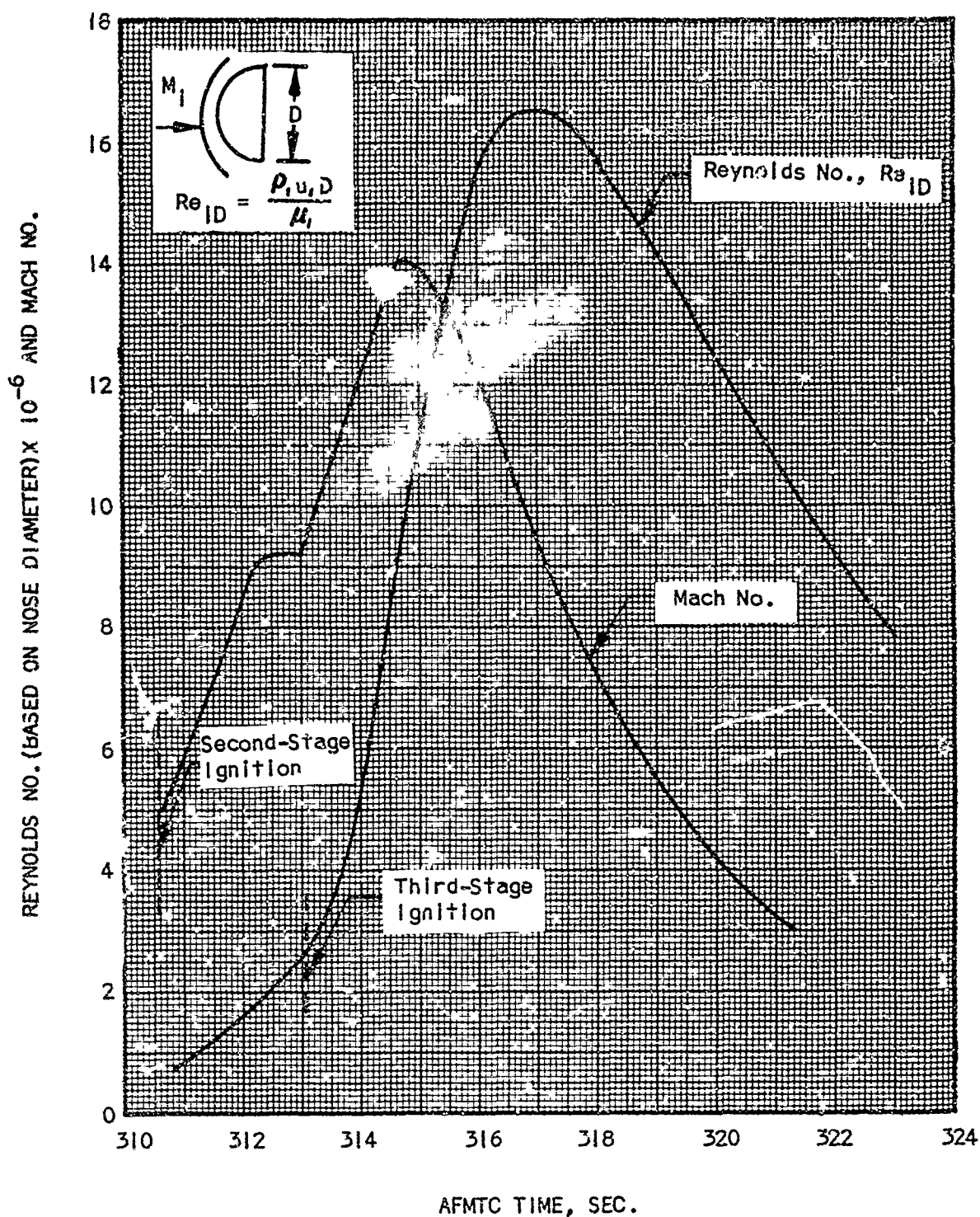


Fig. 5. R-26 Reynolds-Number and Mach-Number Histories during Second- and Third-Stage Boost

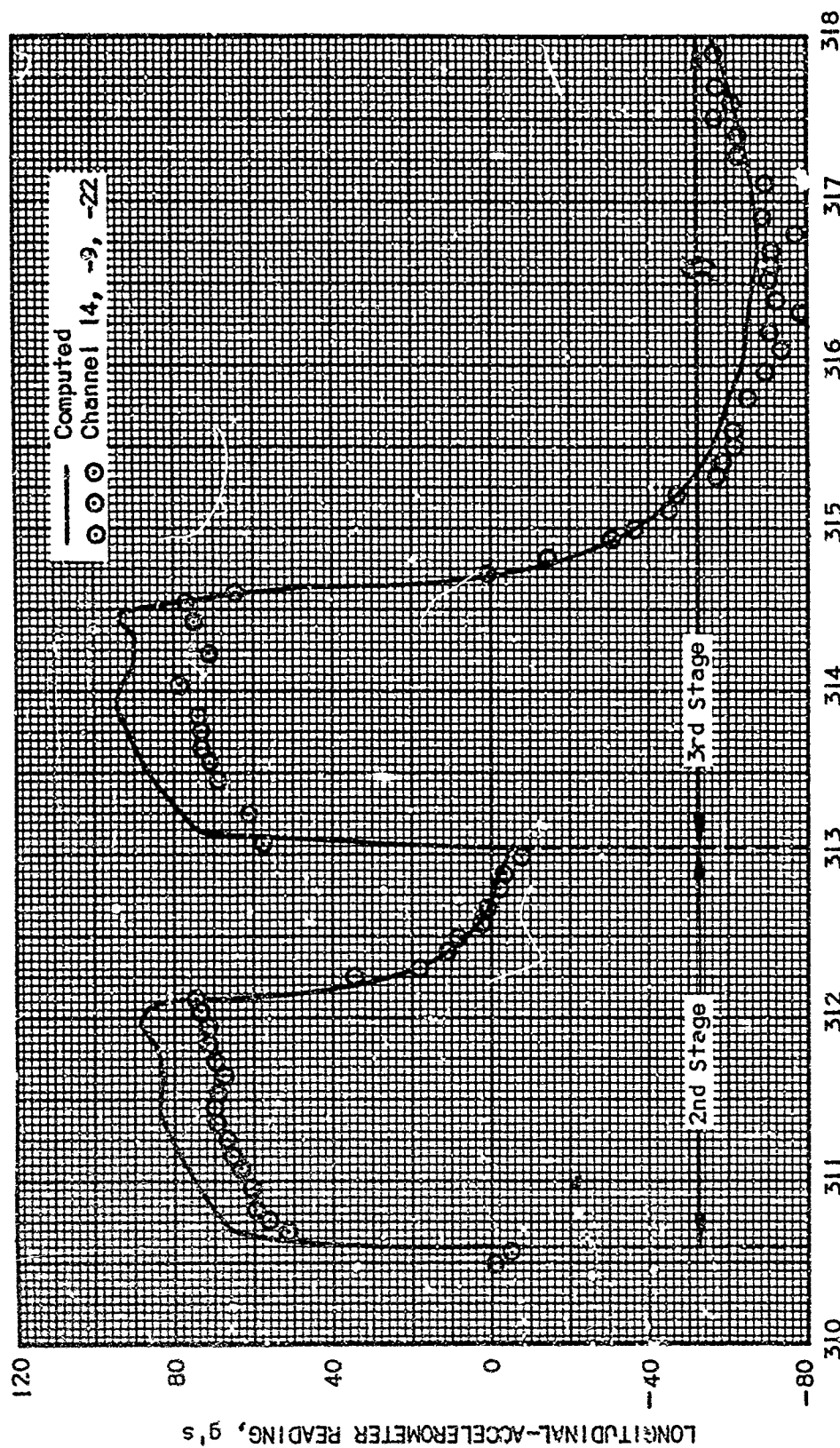


Fig. 6. R-26 Longitudinal Accelerations during Re-Entry

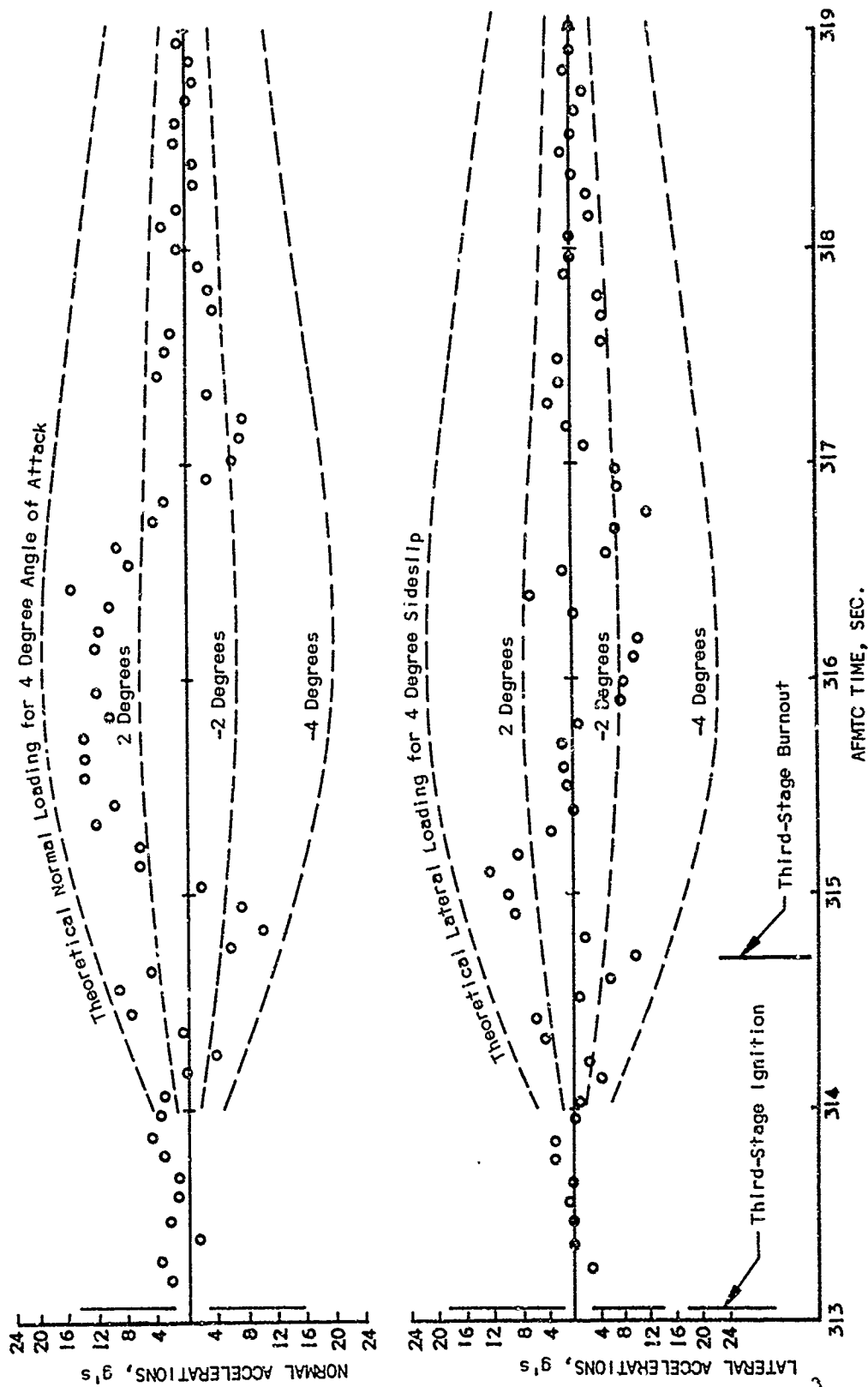


Fig. 7. R-26 Normal and Lateral Accelerations during Re-Entry

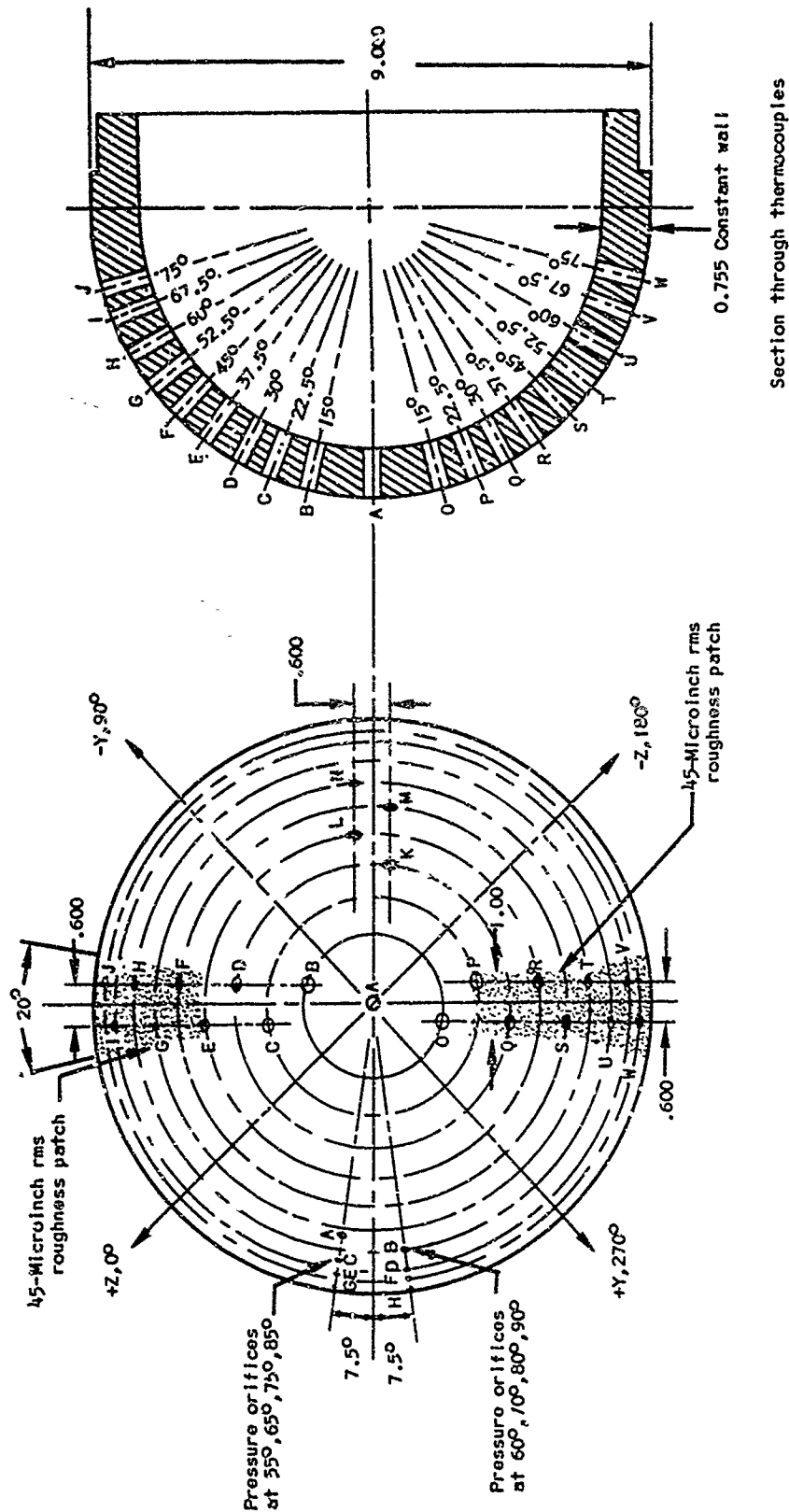


Fig. 8. R-26 Nose, Thermocouple and Pressure-Orifice Locations

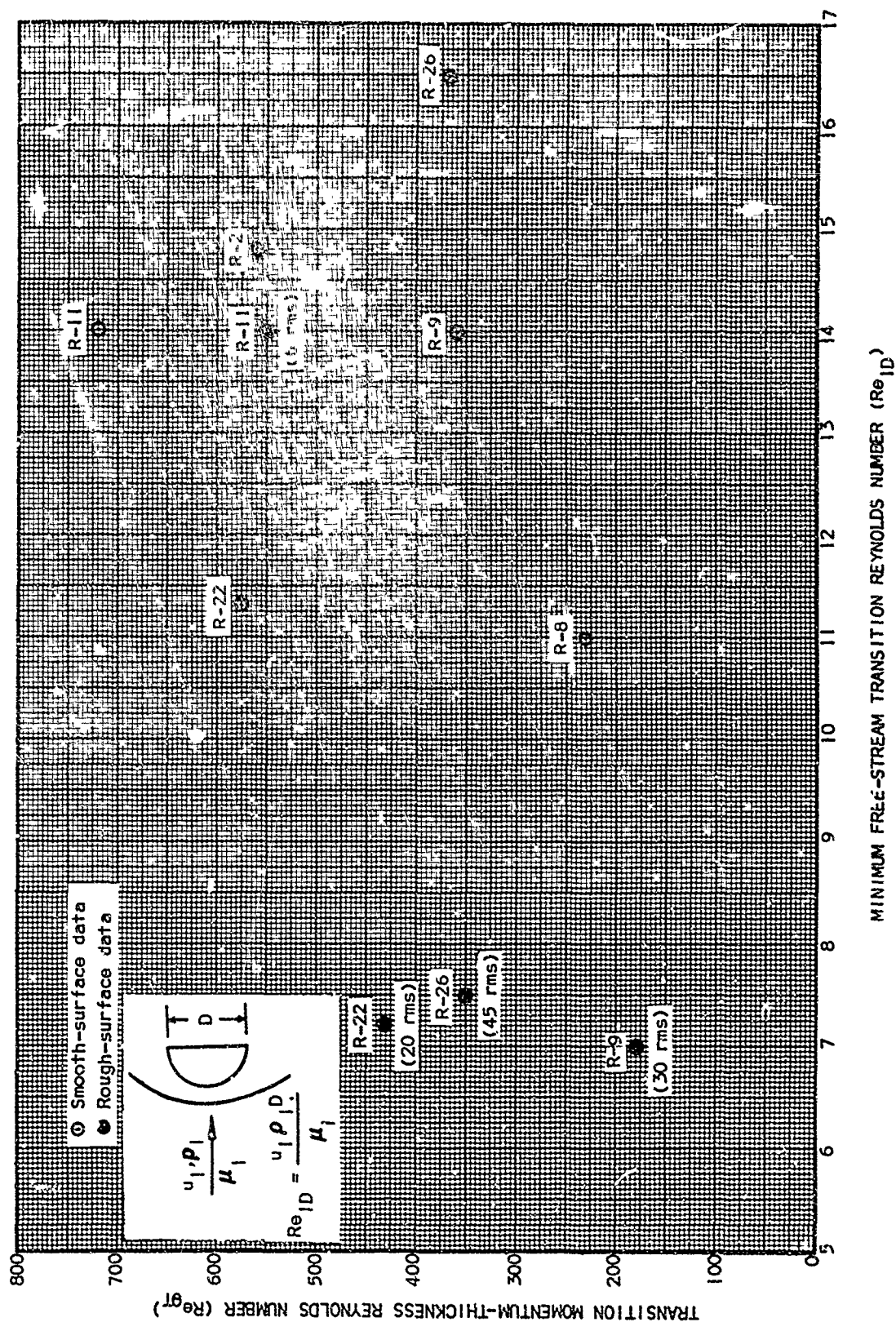


Fig. 9. Summary of X-17 Transition Reynolds Number on Hemispheres

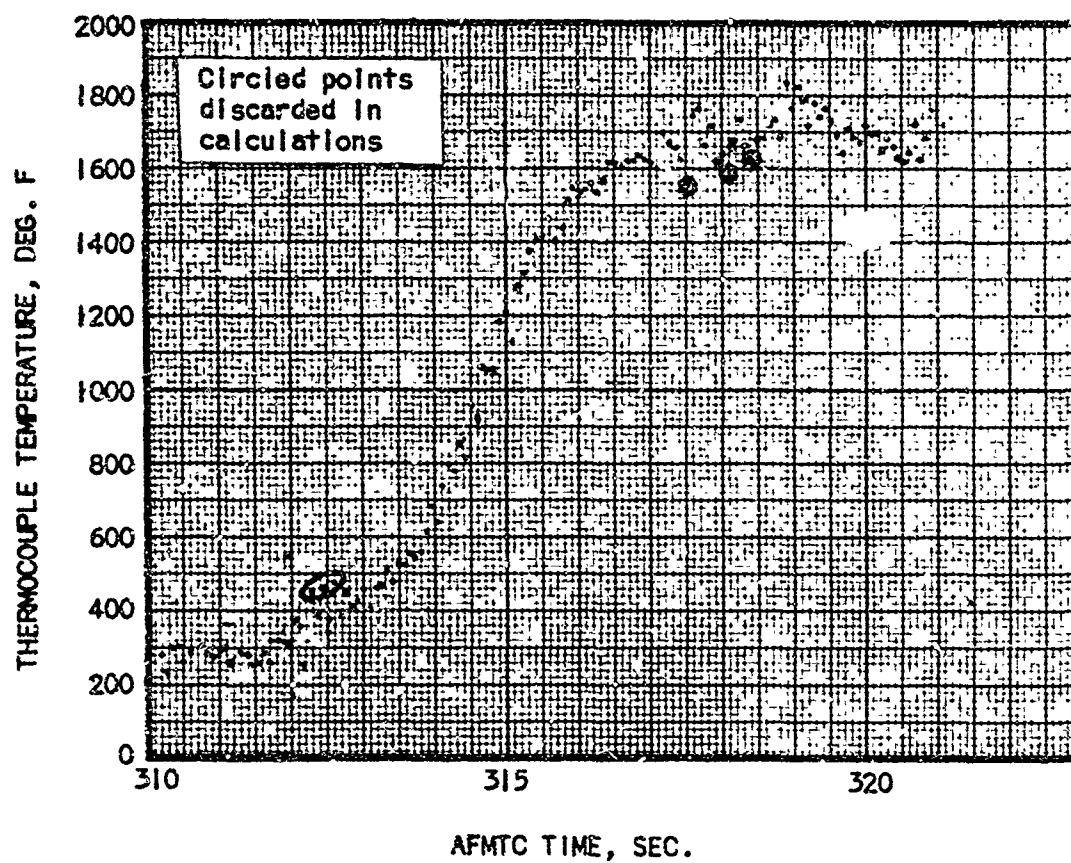


Fig. 10. Measured Temperature at Thermocouple A

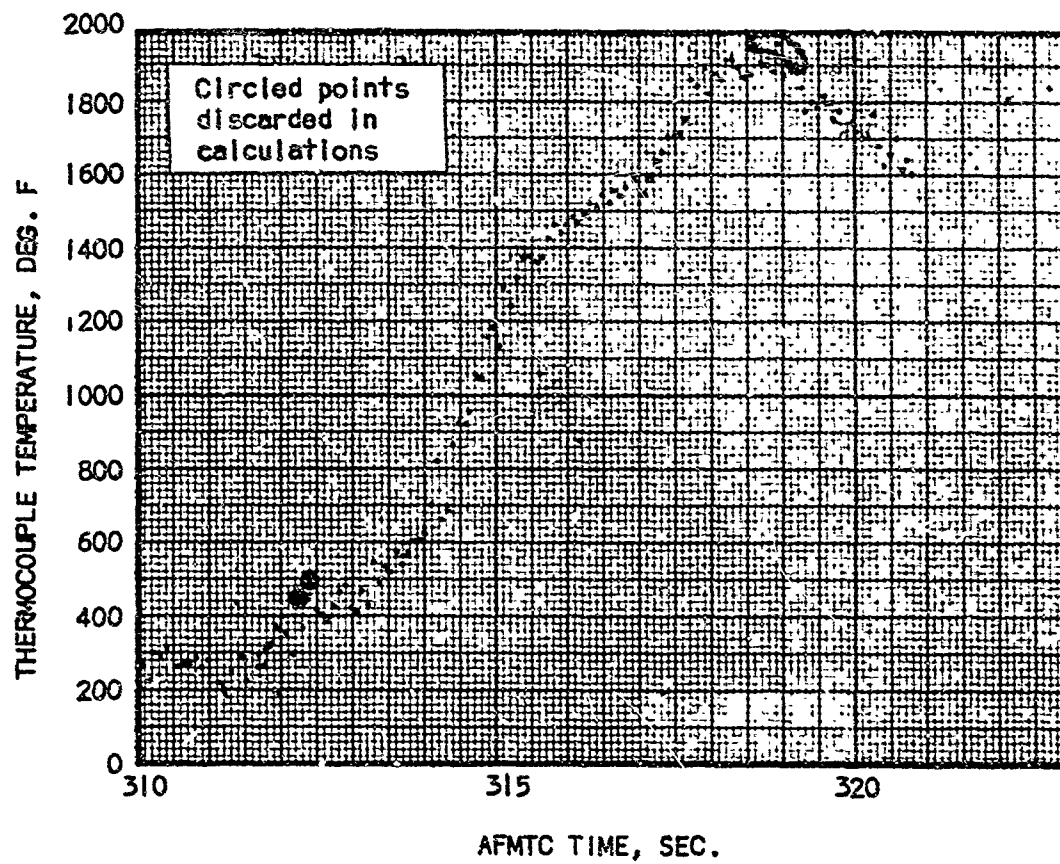


Fig. 11. Measured Temperature at Thermocouple B

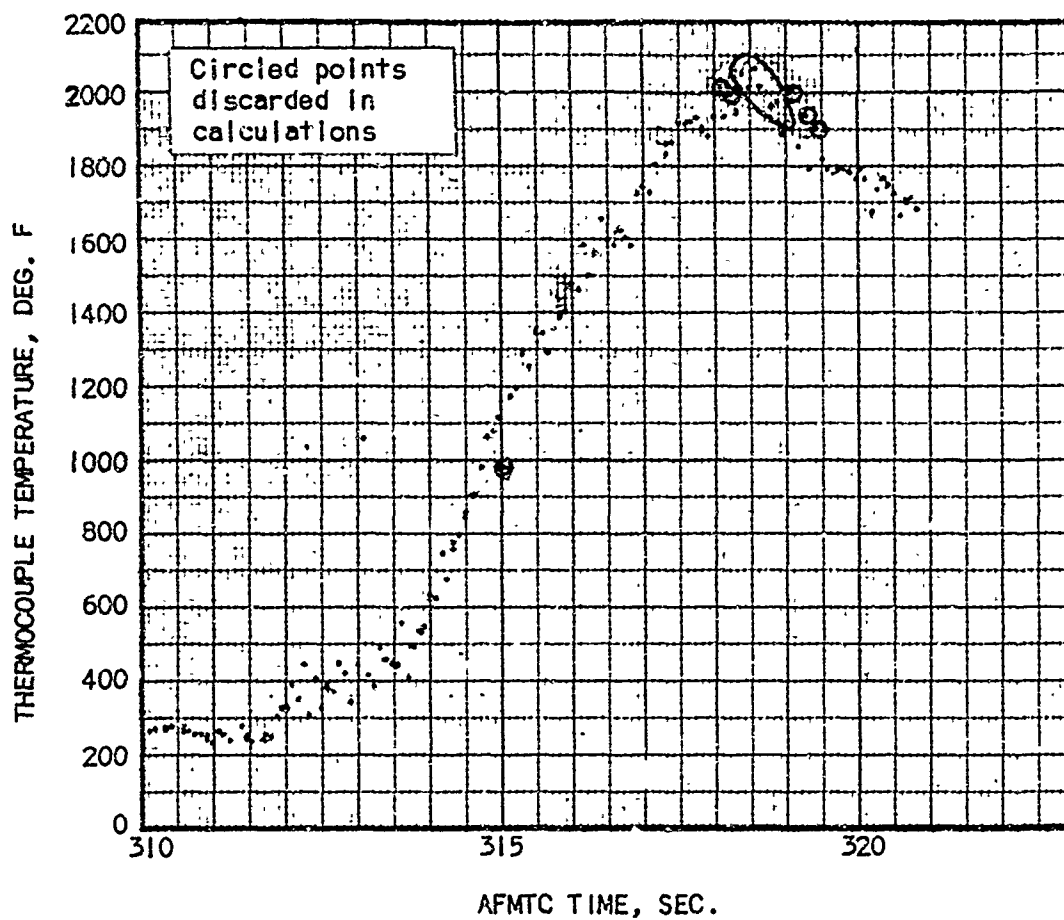


Fig. 12. Measured Temperature at Thermocouple C

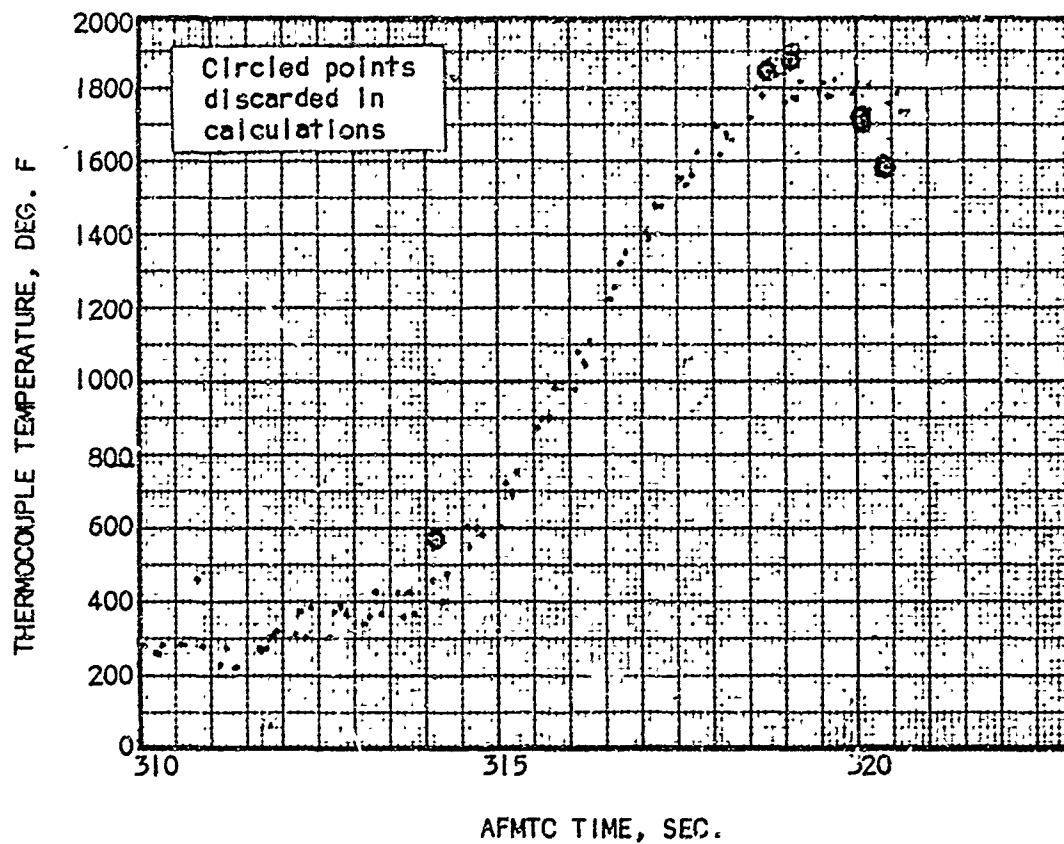


Fig. 13. Measured Temperature at Thermocouple D

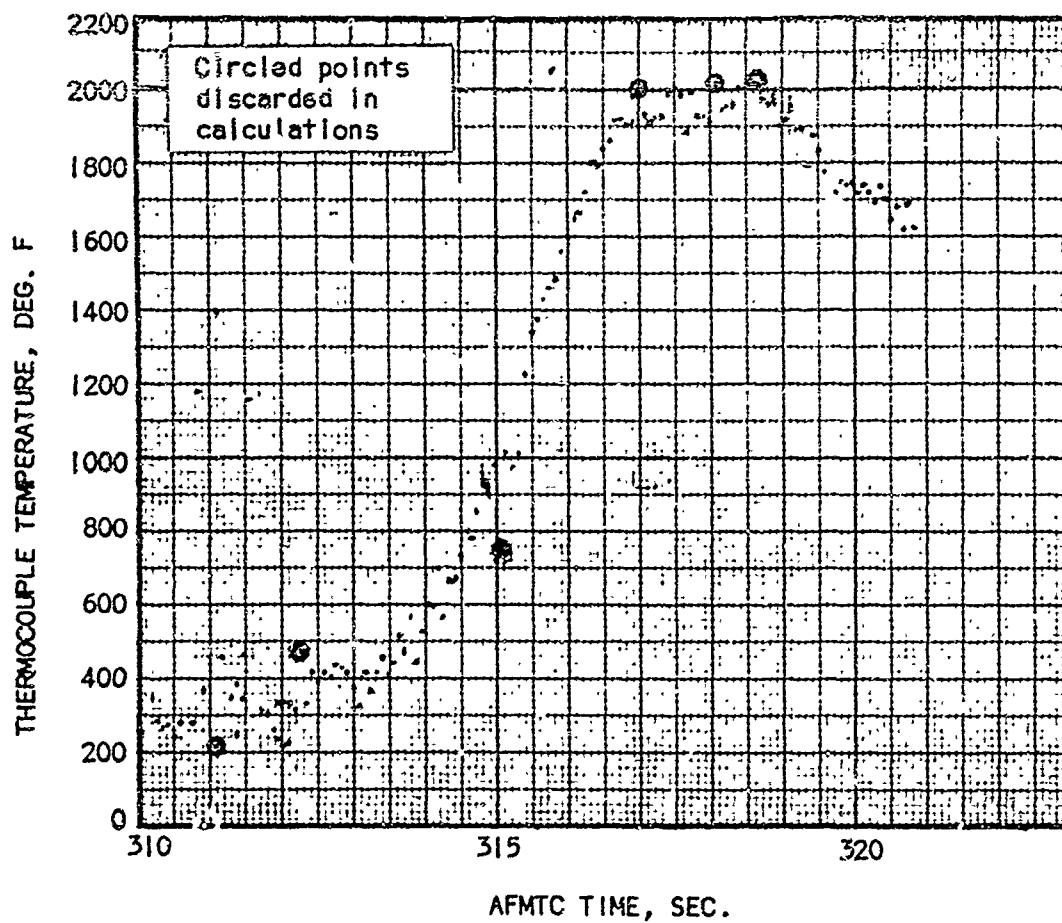


Fig. 14. Measured Temperature at Thermocouple E

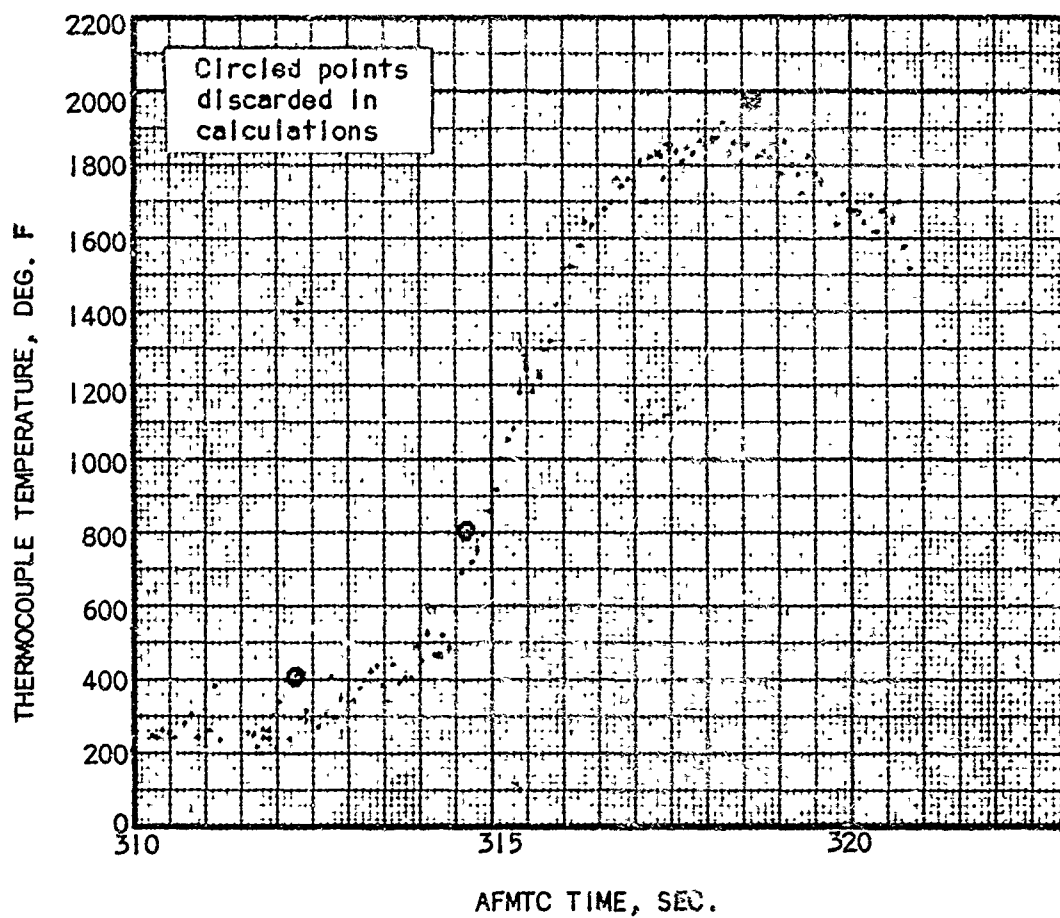


Fig. 15. Measured Temperature at Thermocouple F

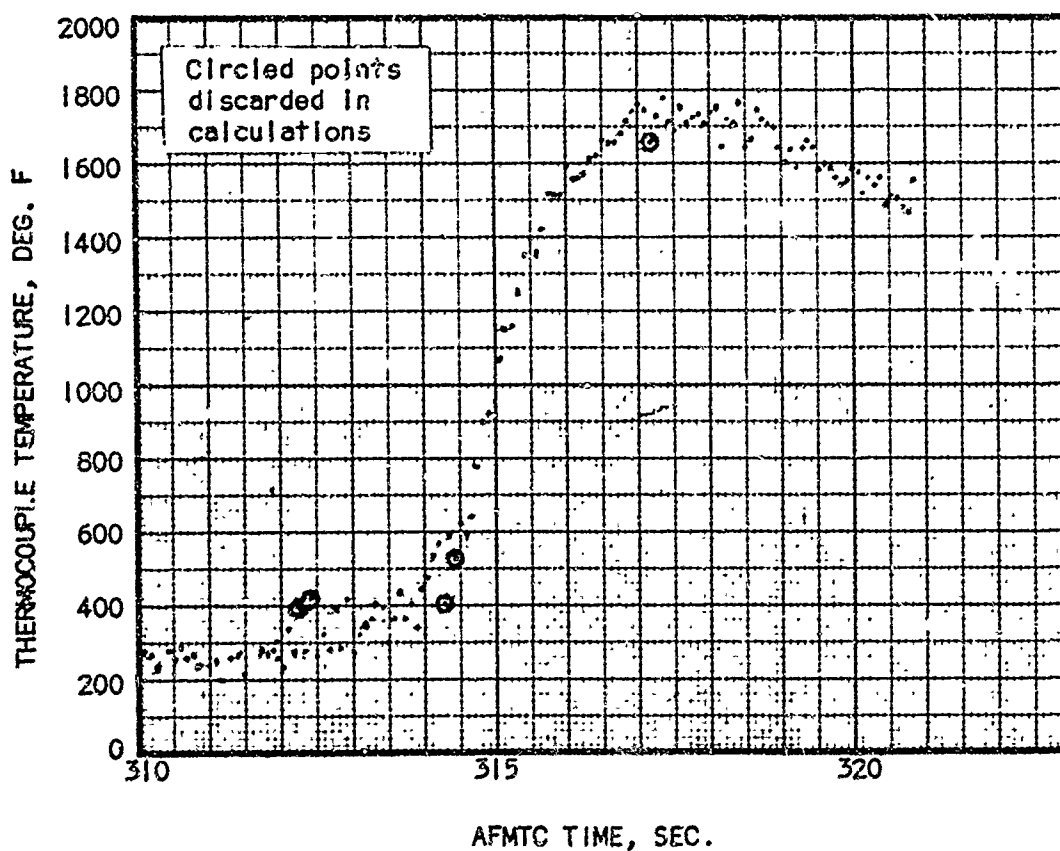


Fig. 16. Measured Temperature at Thermocouple G

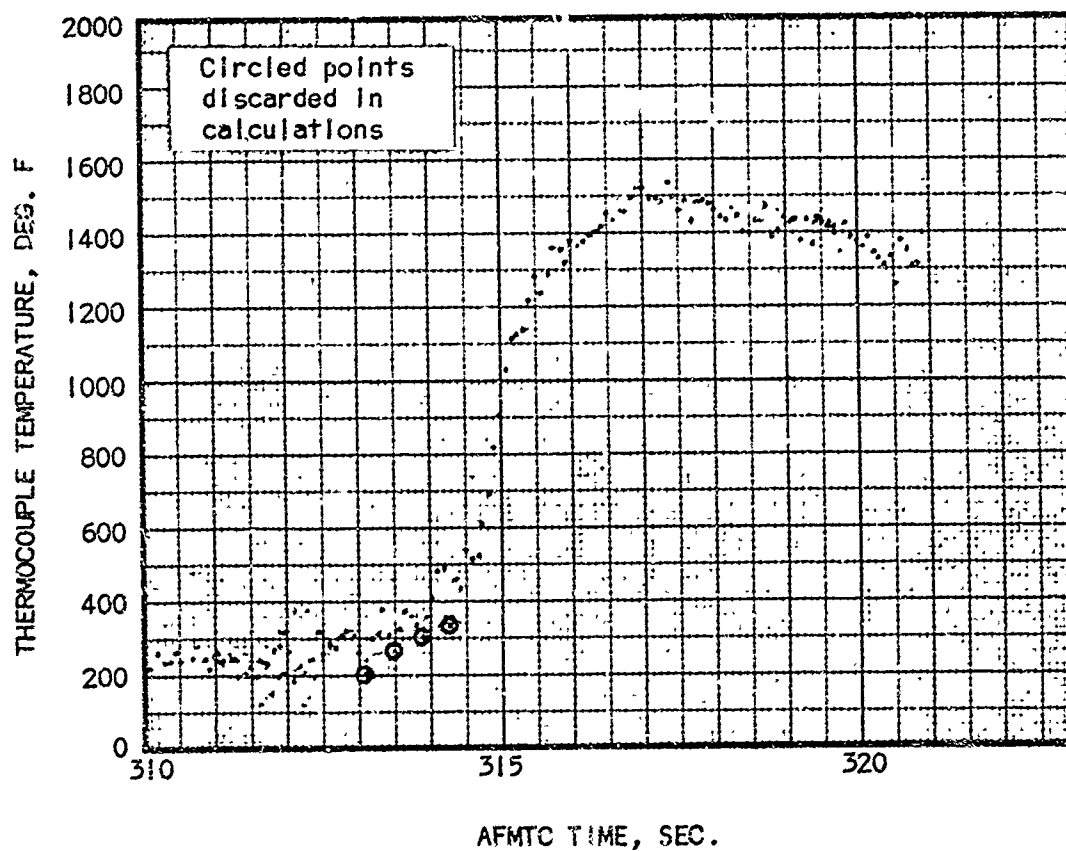


Fig. 17. Measured Temperature at Thermocouple H

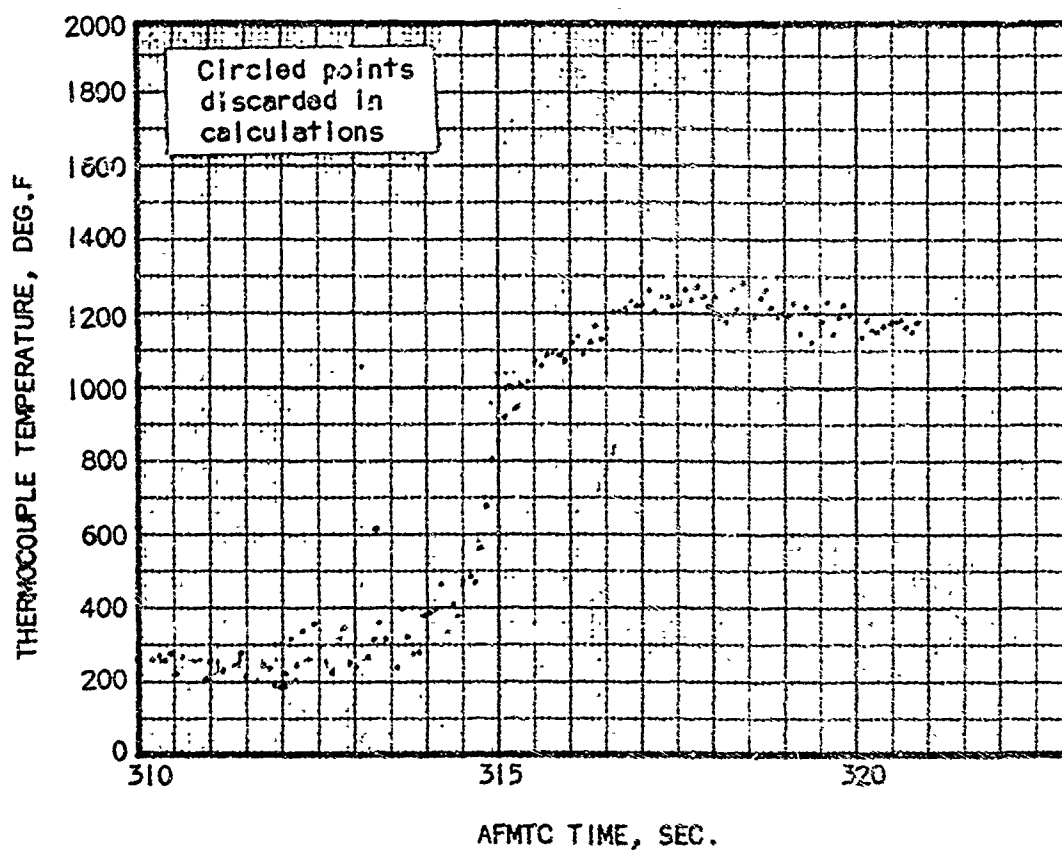


Fig. 18. Measured Temperature at Thermocouple I

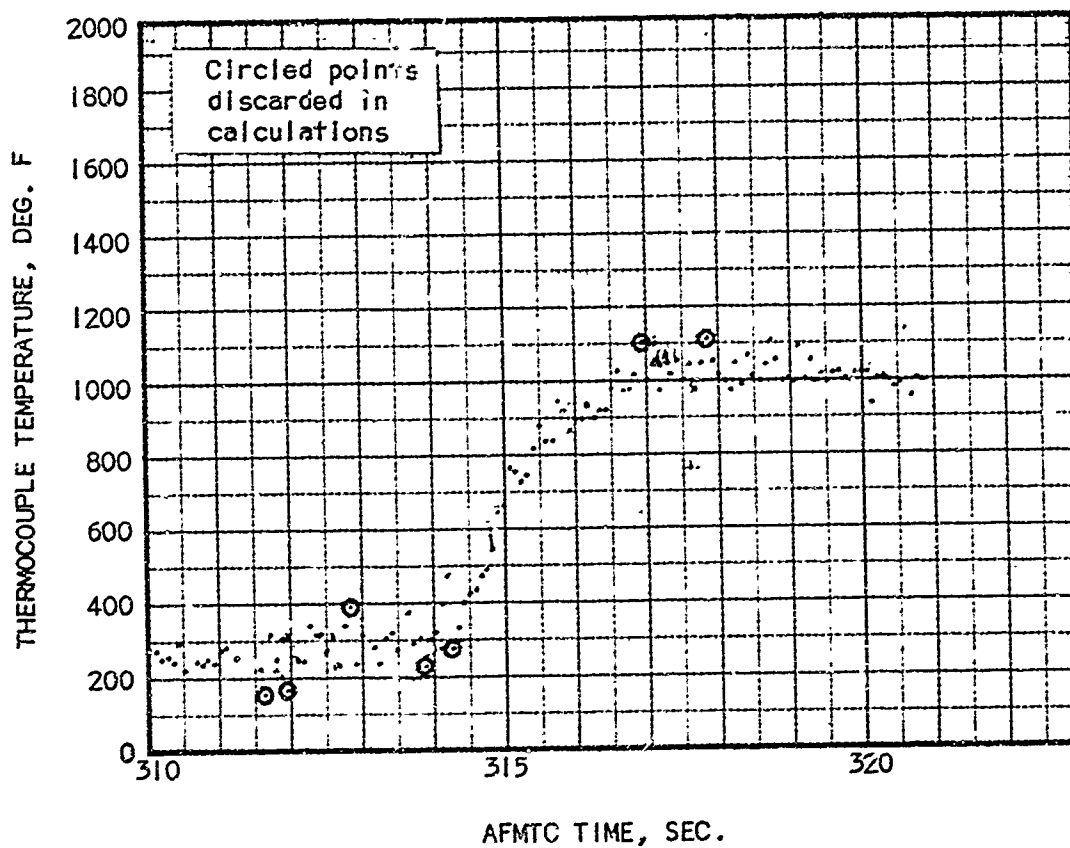


Fig. 19. Measured Temperature at Thermocouple J

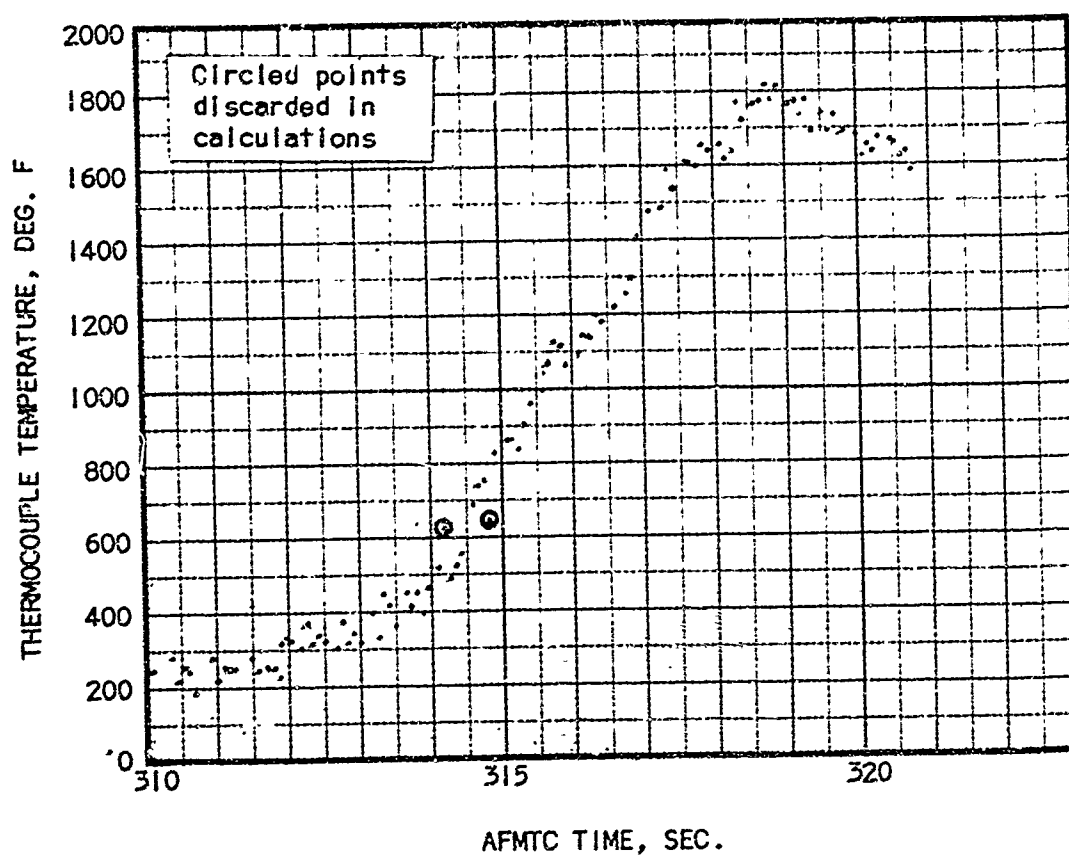


Fig. 20. Measured Temperature at Thermocouple K

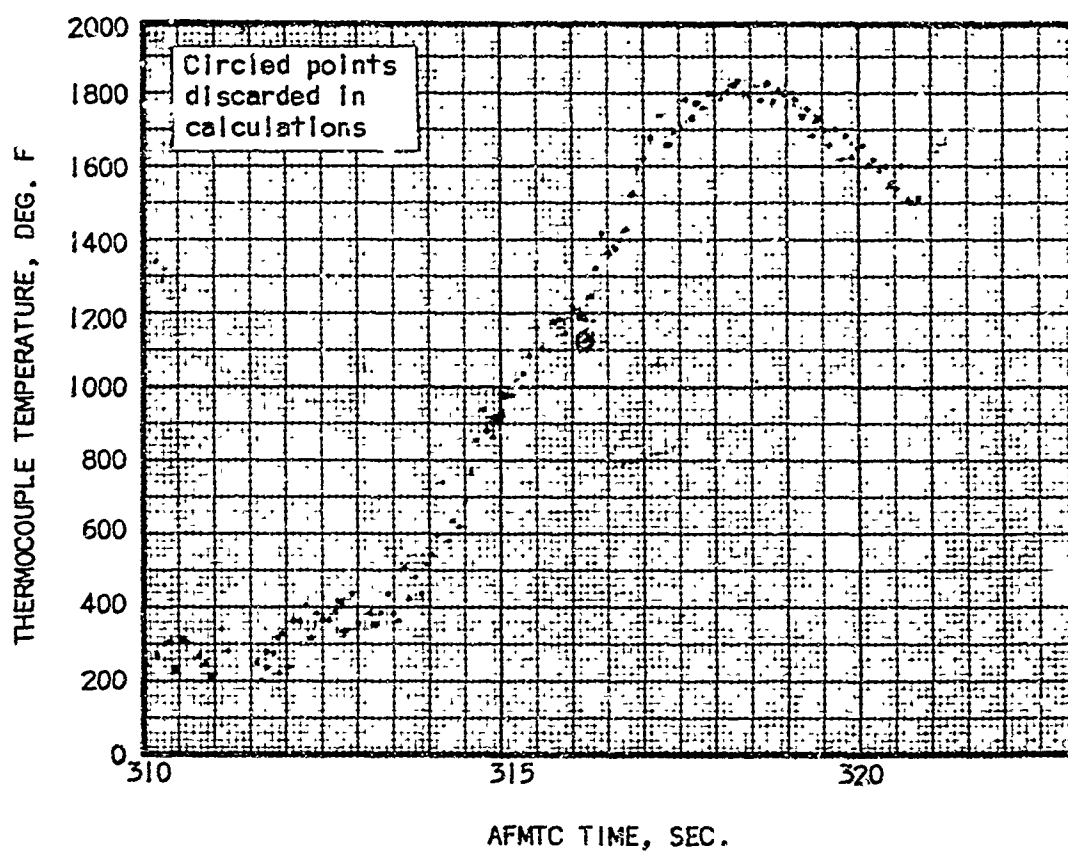


Fig. 21. Measured Temperature at Thermocouple I.

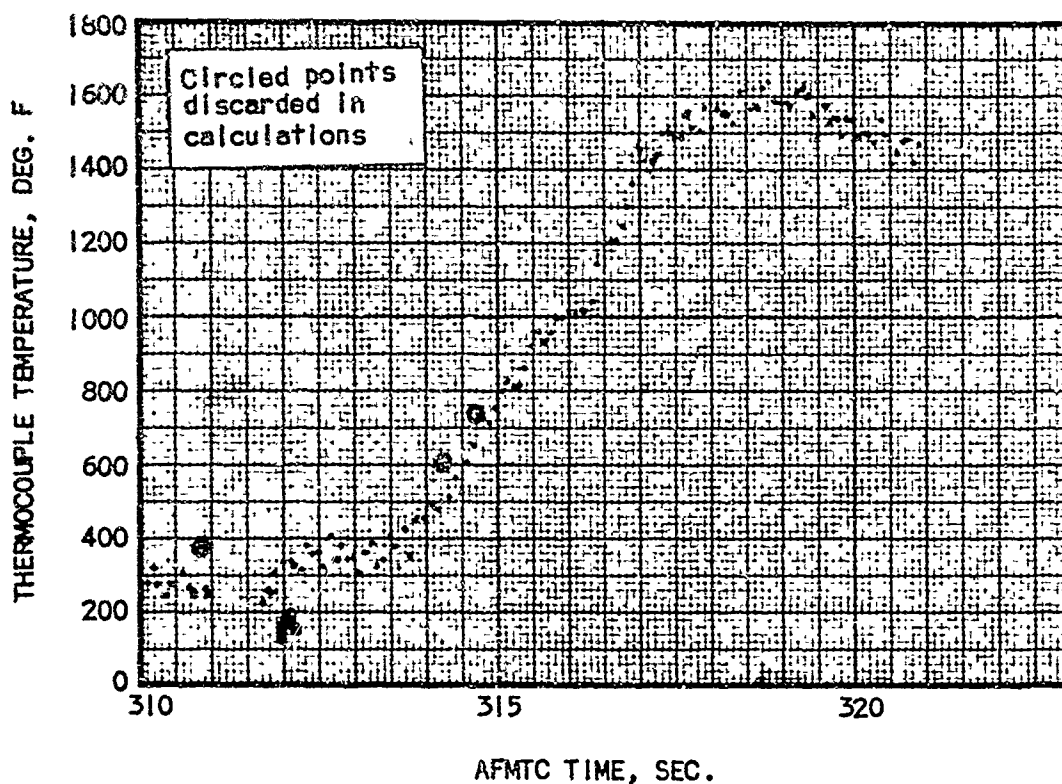


Fig. 22. Measured Temperature at Thermocouple M

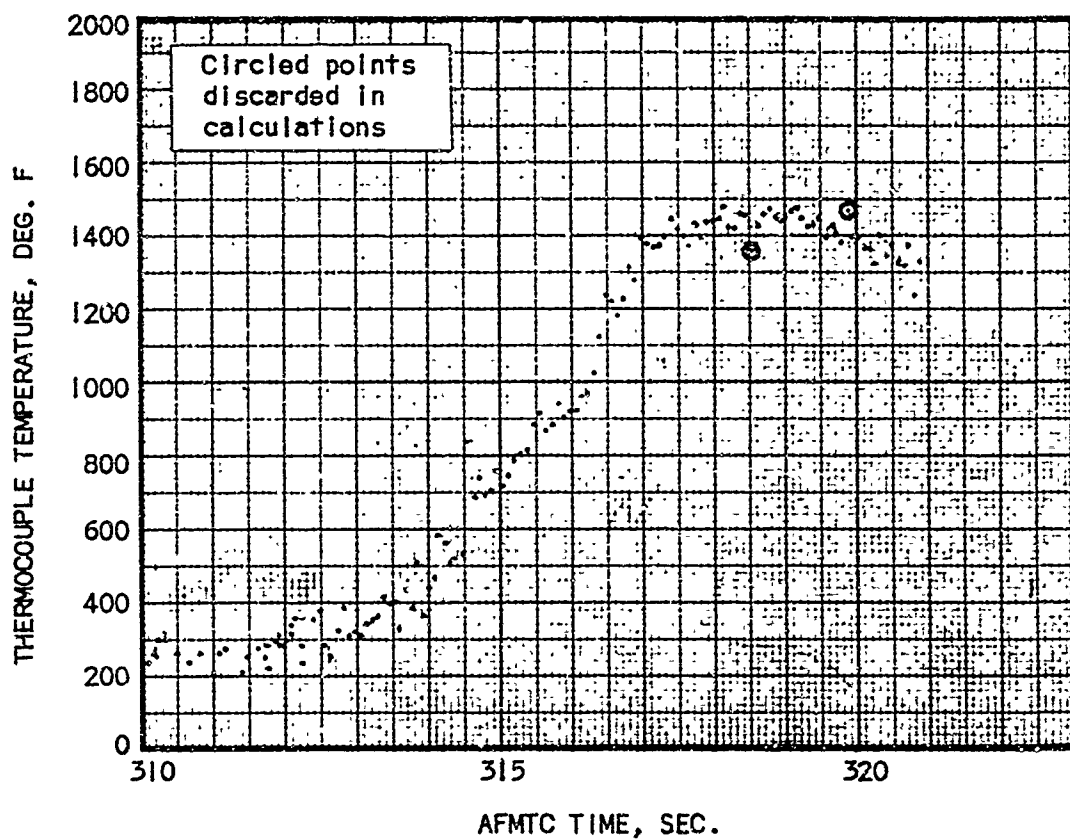


Fig. 23. Measured Temperature at Thermocouple N

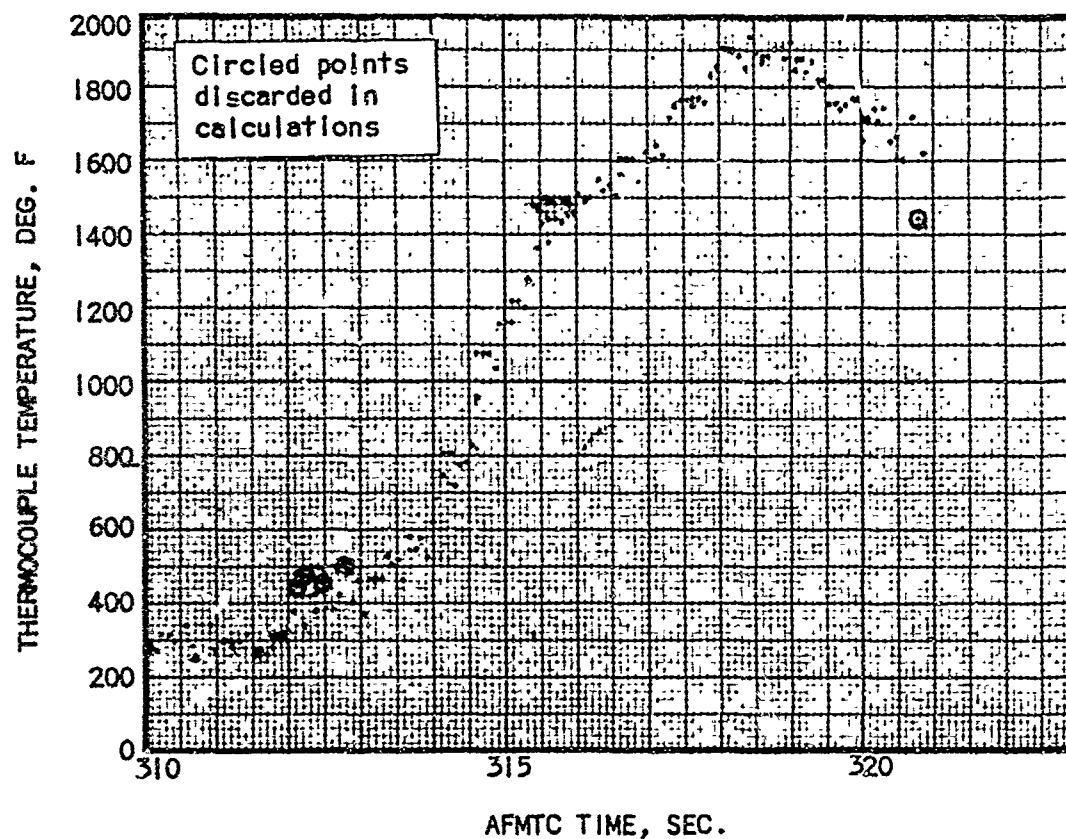


Fig. 24. Measured Temperature at Thermocouple 0

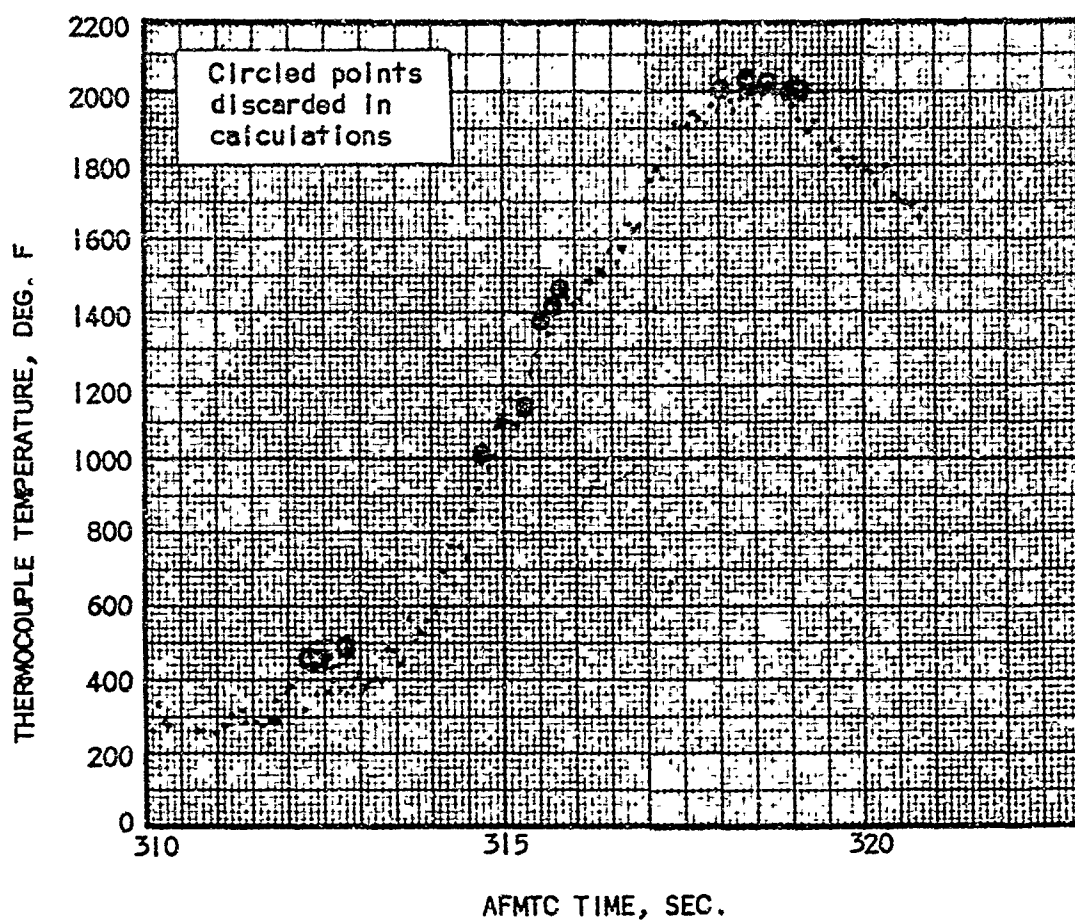


Fig. 25. Measured Temperature at Thermocouple P

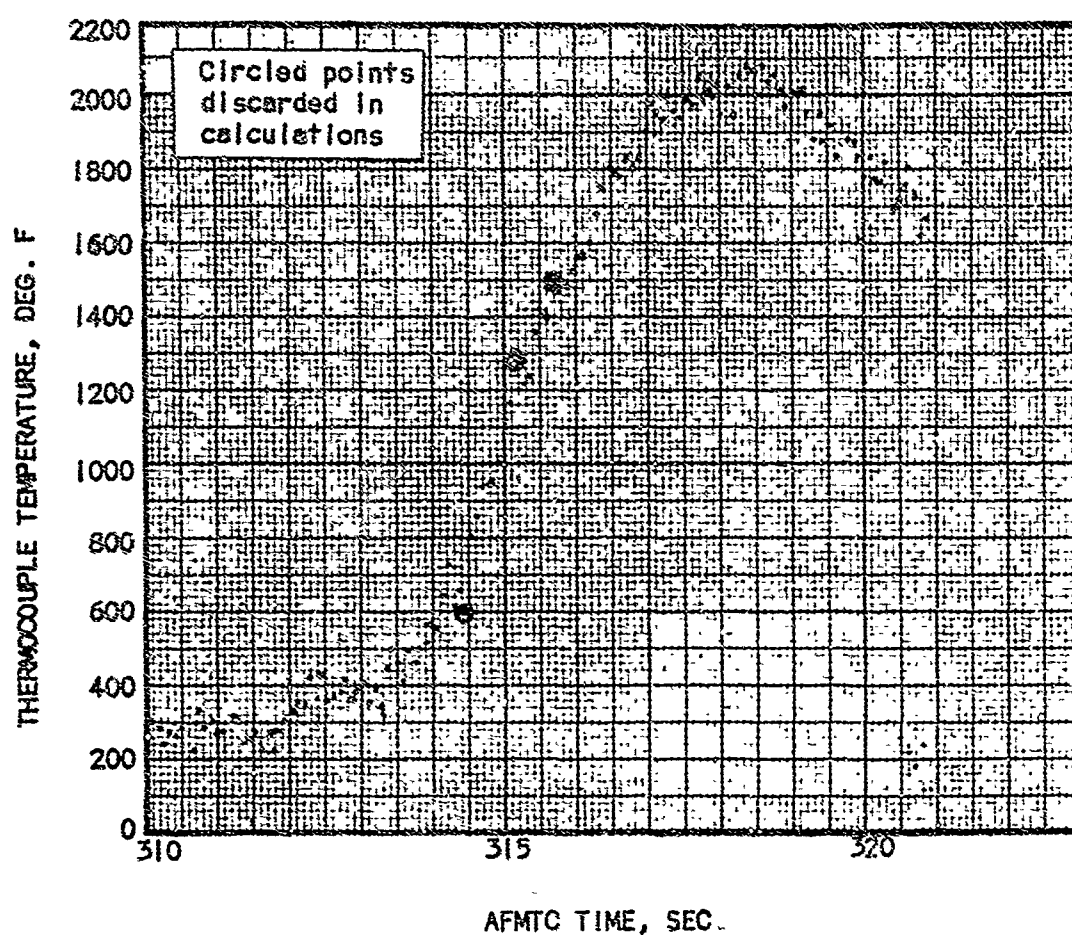


Fig. 26. Measured Temperature at Thermocouple Q

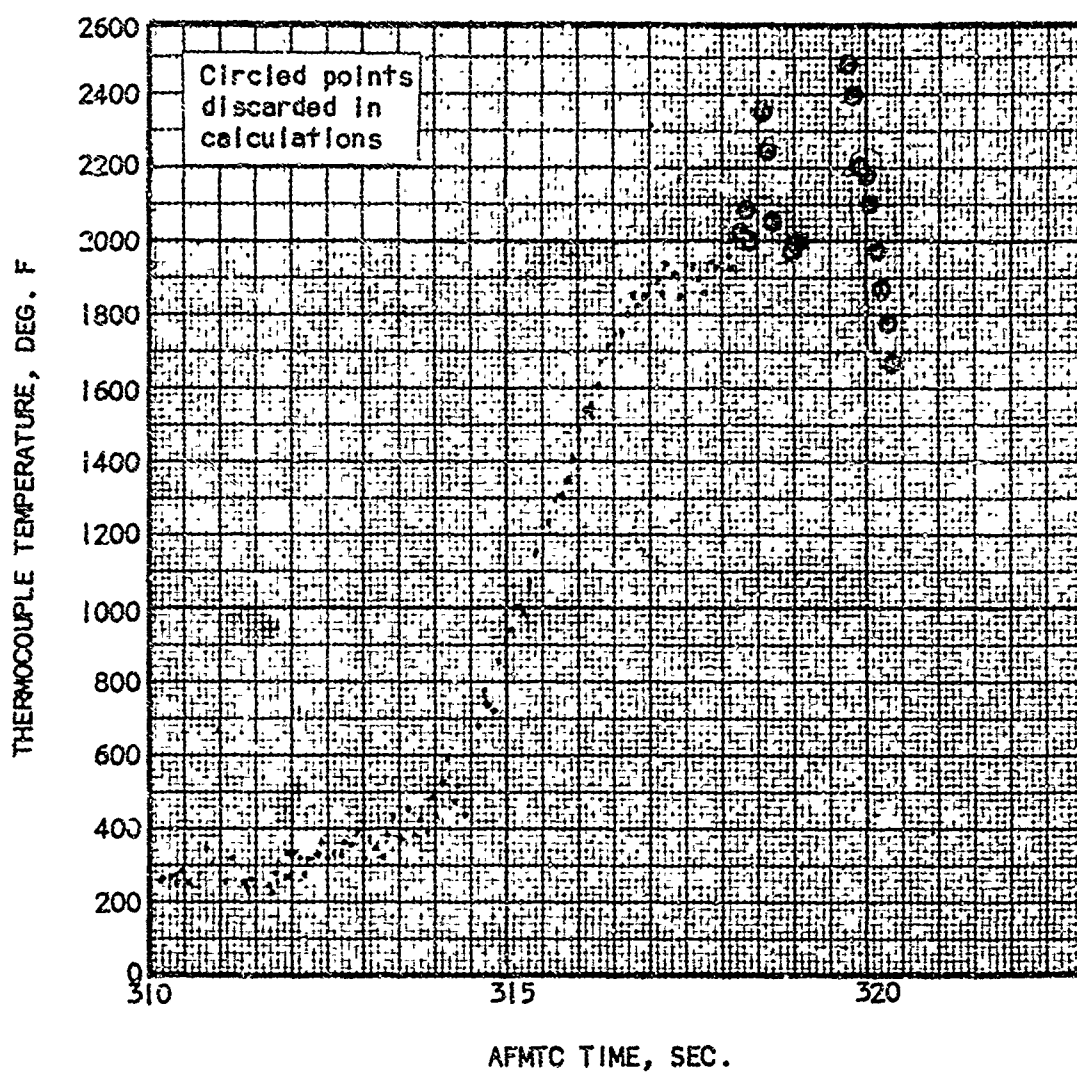


Fig. 27. Measured Temperature at Thermocouple R

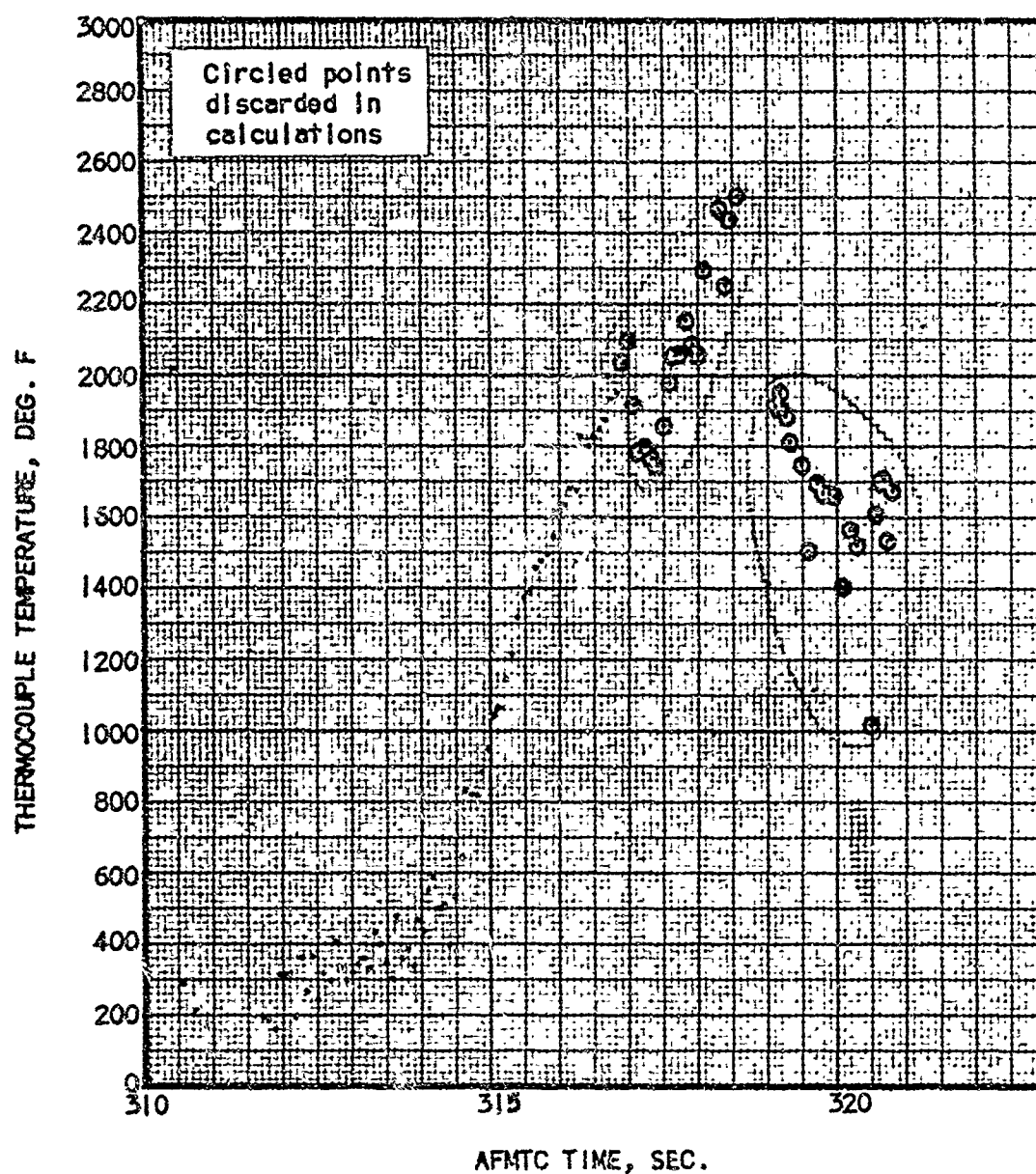


Fig. 28. Measured Temperature at Thermocouple 8

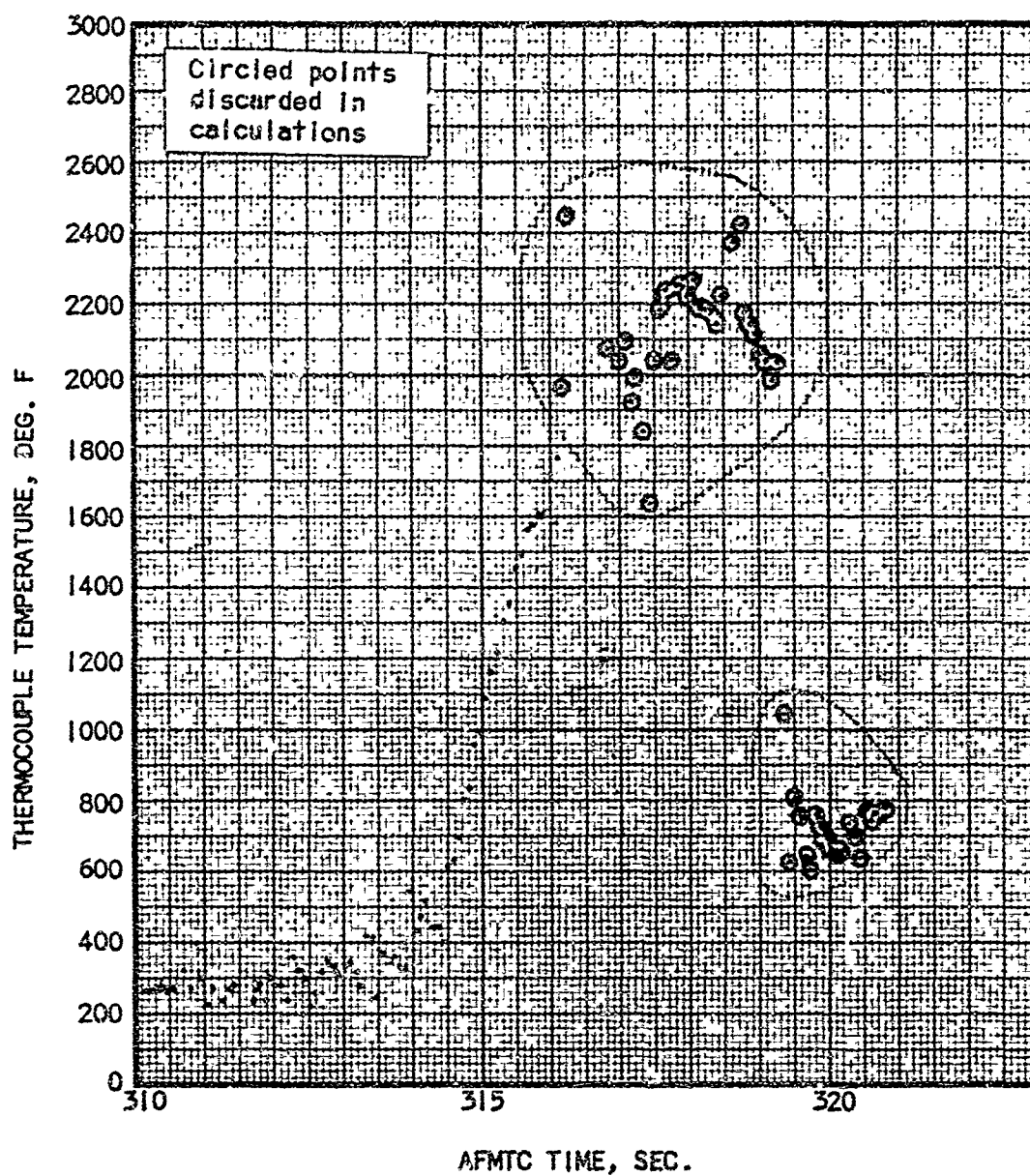


Fig. 29. Measured Temperature at Thermocouple T

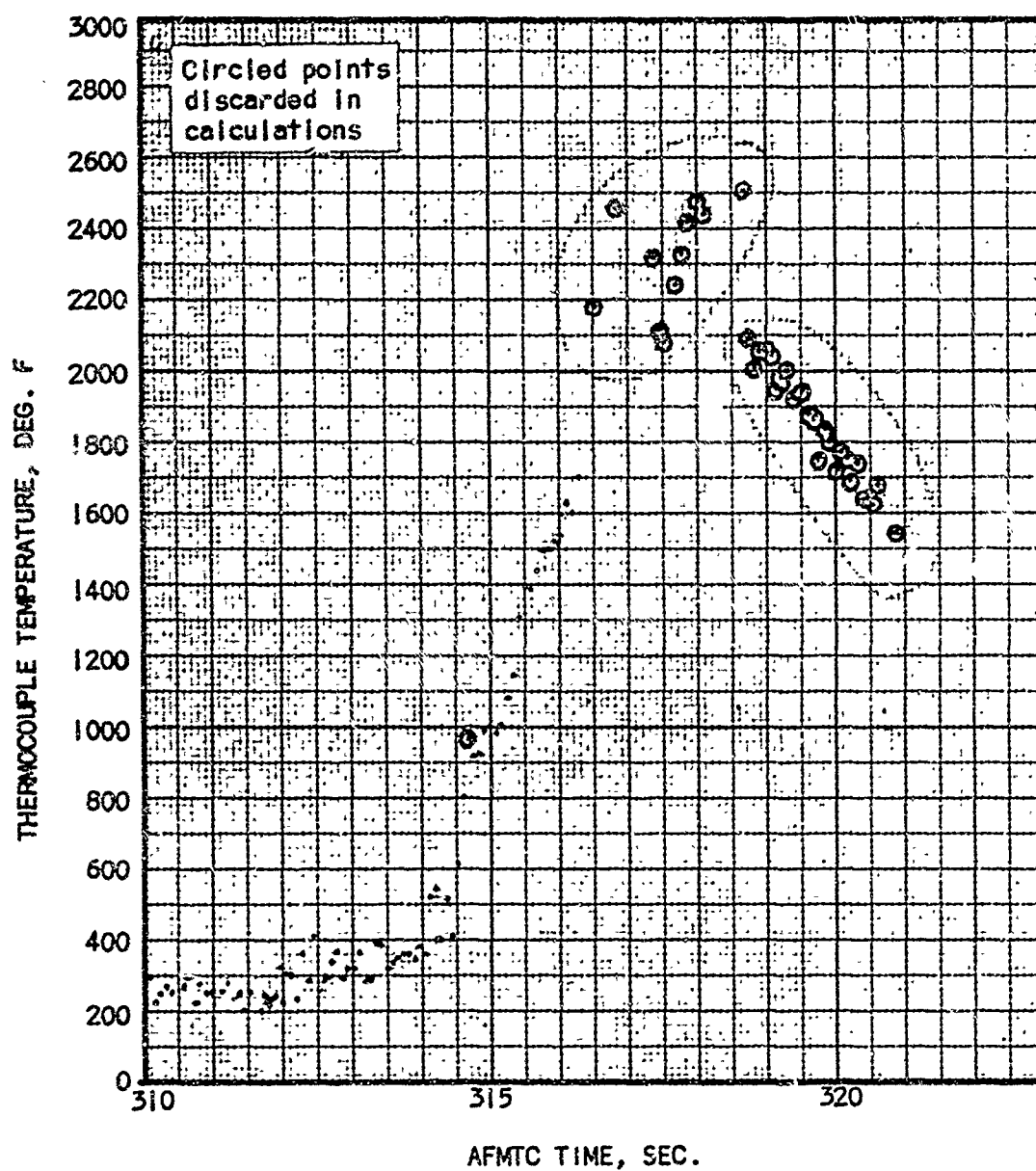


Fig. 30. Measured Temperature at Thermocouple U

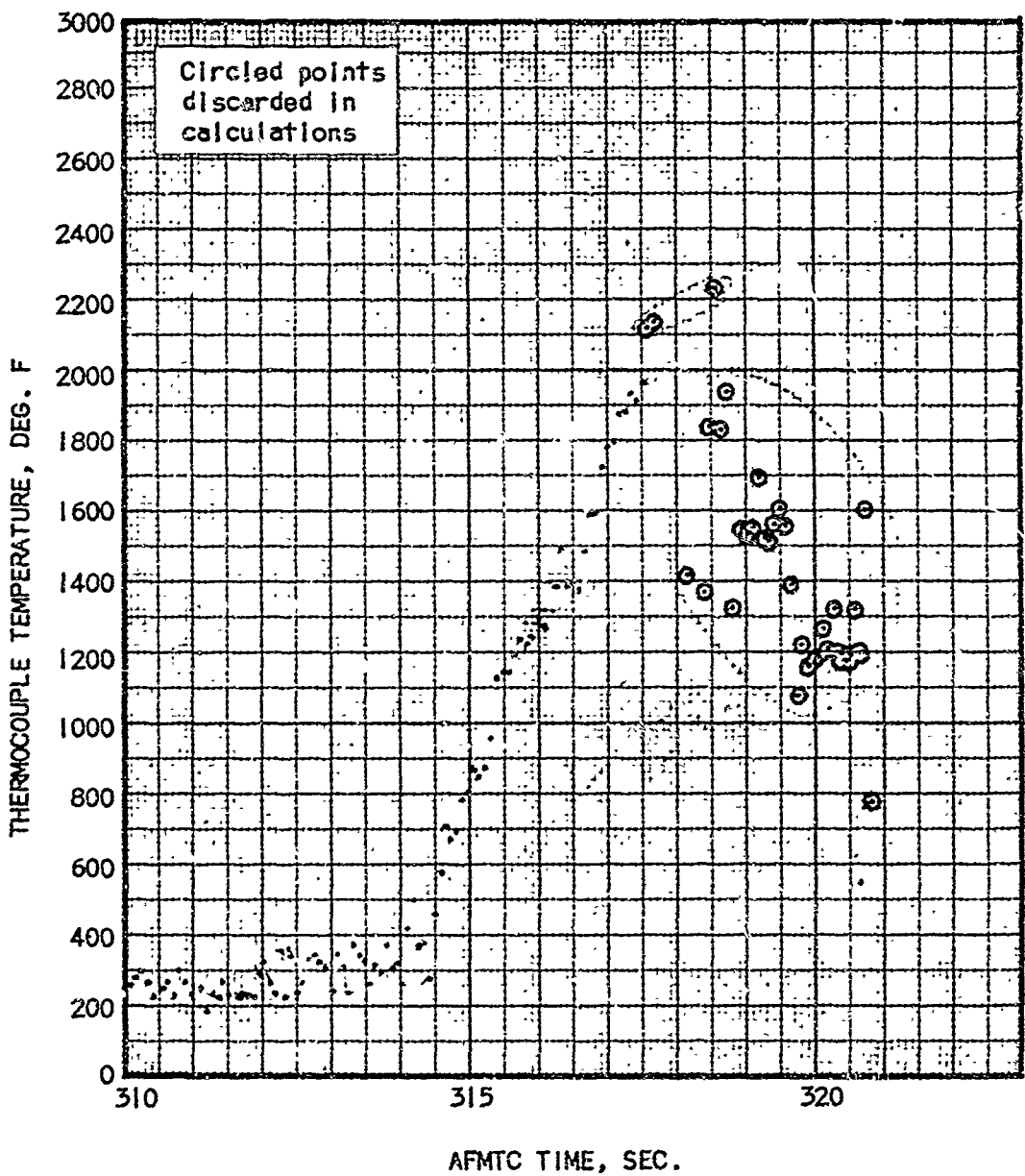


Fig. 31. Measured Temperature at Thermocouple V

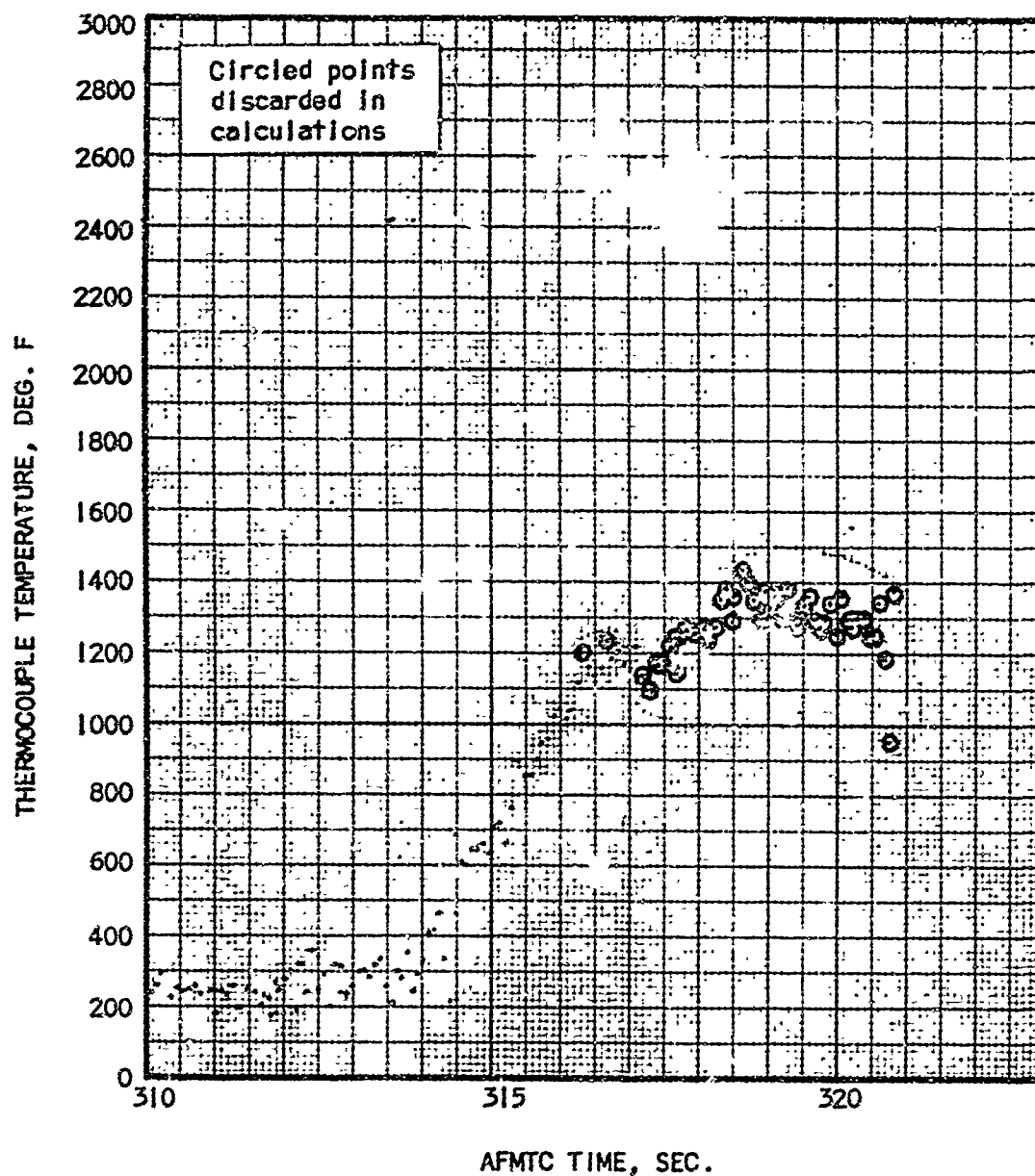


Fig. 32. Measured Temperature at Thermocouple W

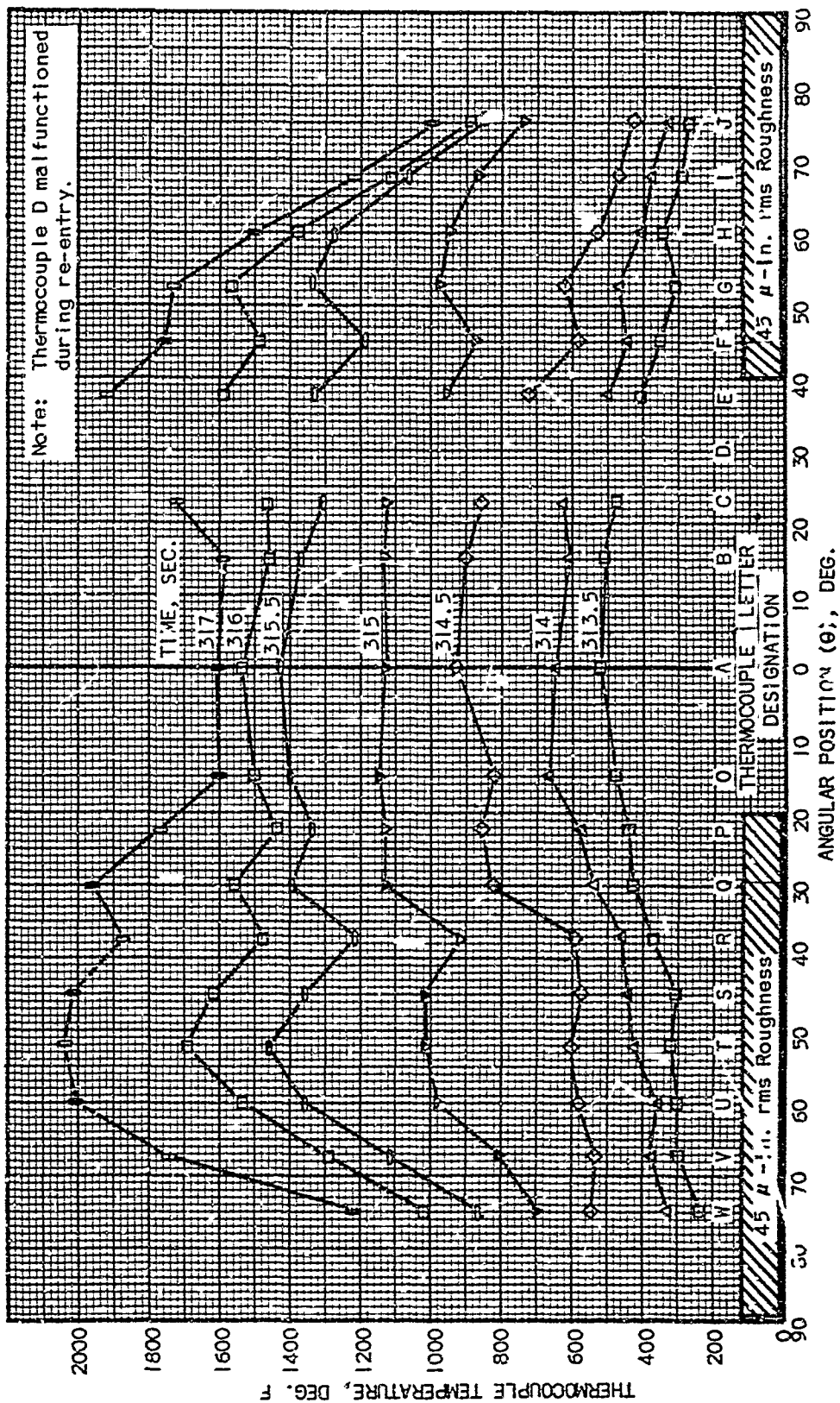


Fig. 33. Comparison of Measured Temperatures on Long and Short Roughness Runs during Re-Entry

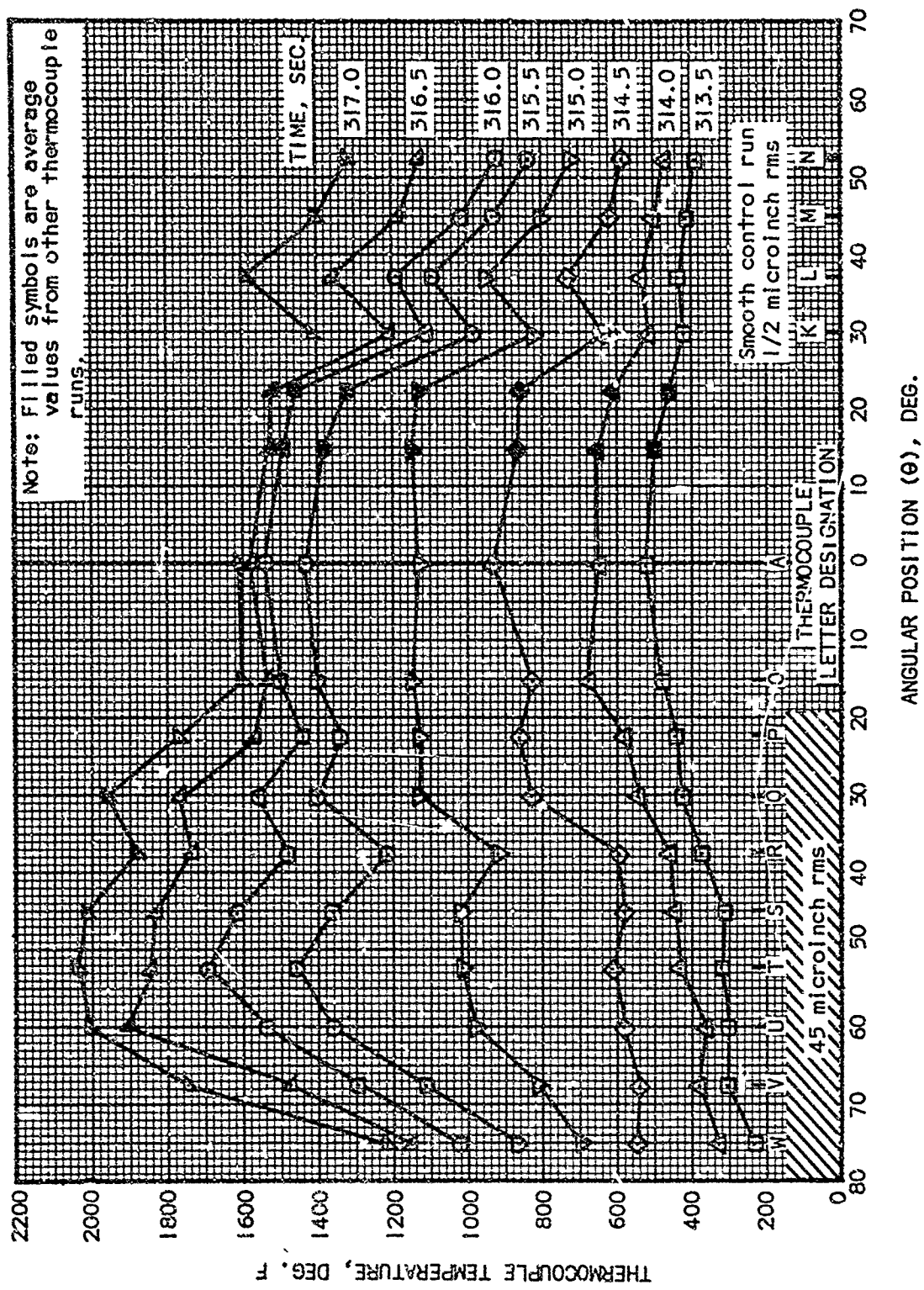


Fig. 34. Comparison of Measured Temperatures on Control Run and Long Rough Run during Re-Entry

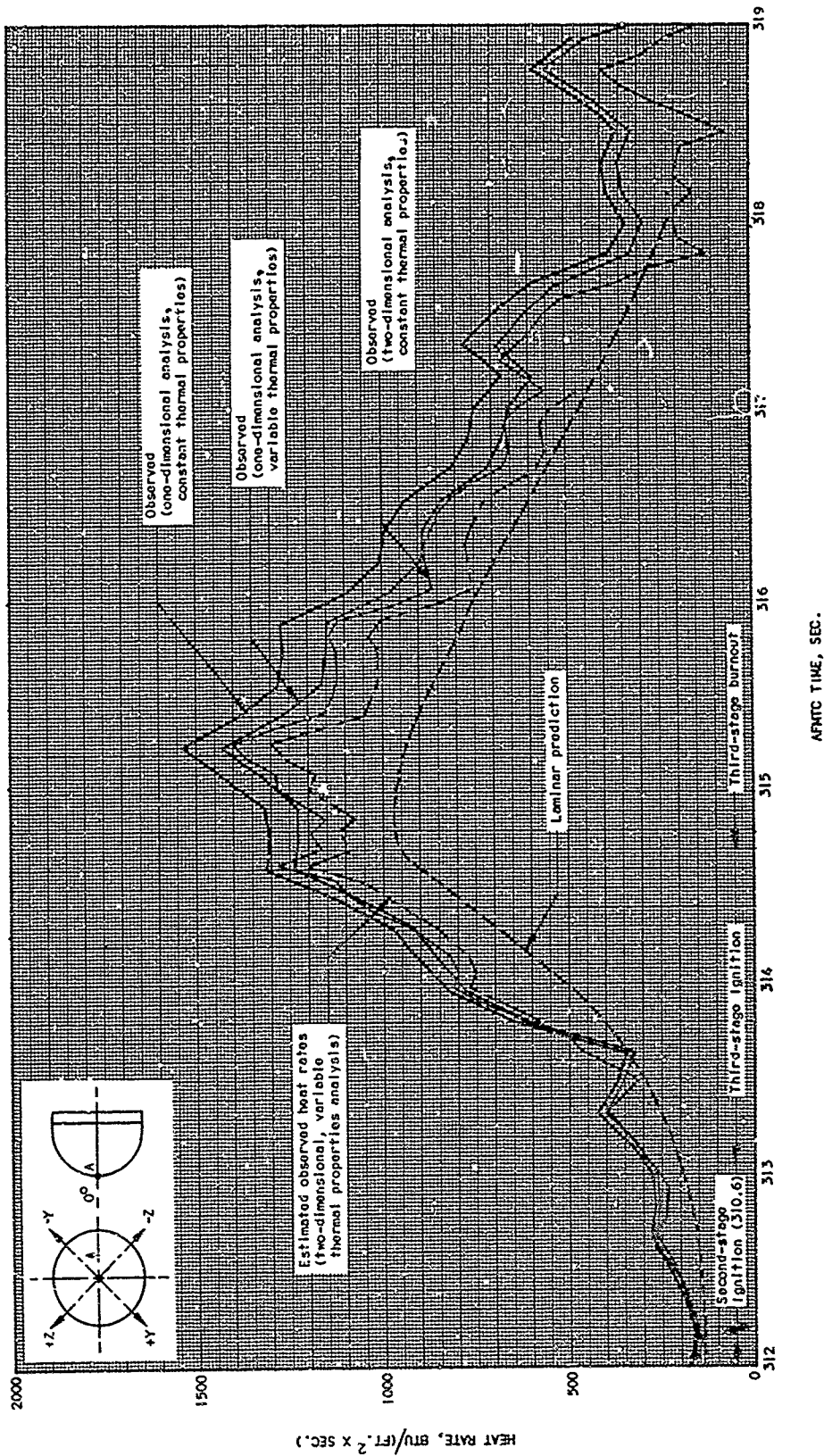


Fig. 35. Comparison of Observed and Predicted Heat Rates of Thermocouple A

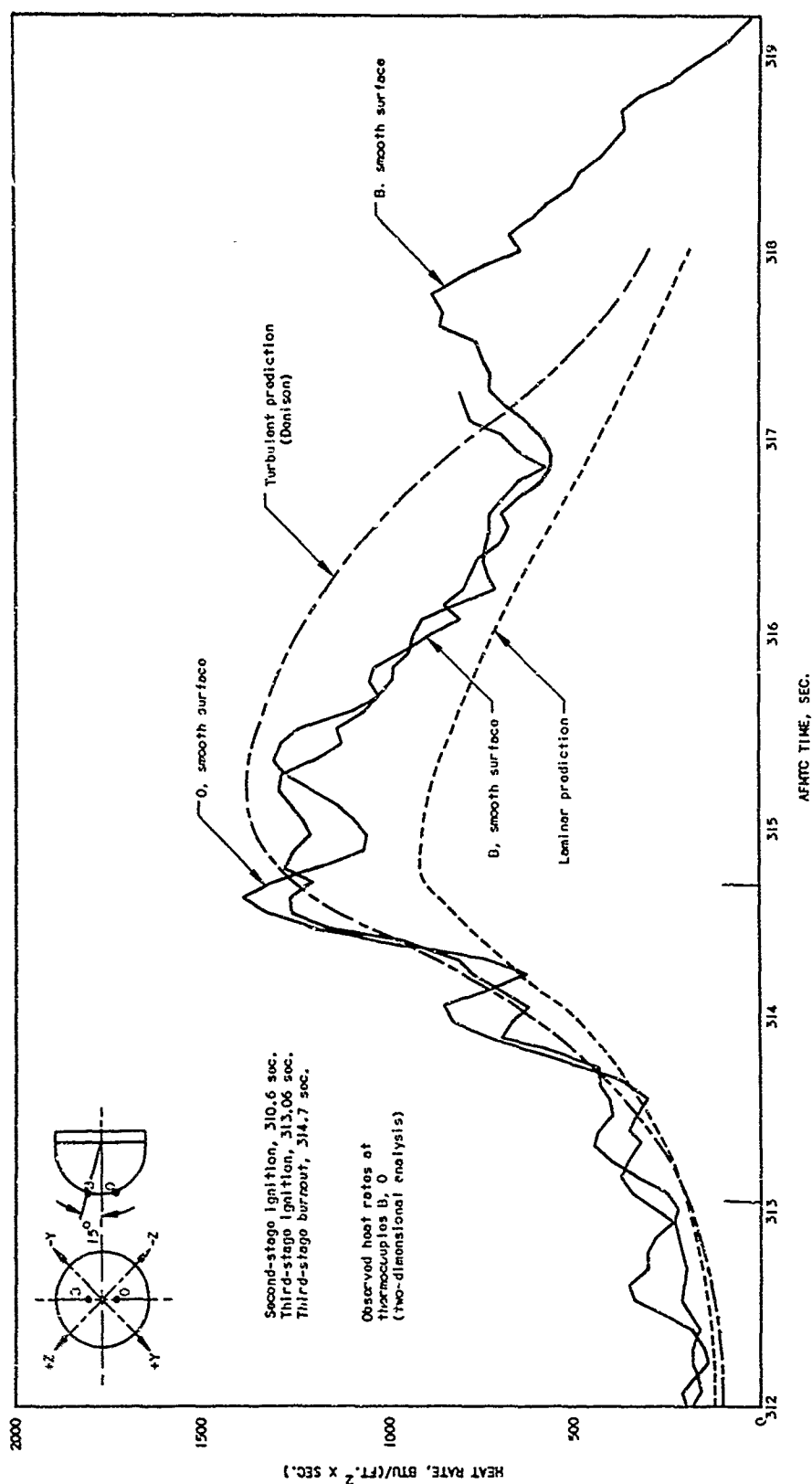


Fig. 36. Comparison of Observed and Predicted Heat Rates at Thermocouples B and O

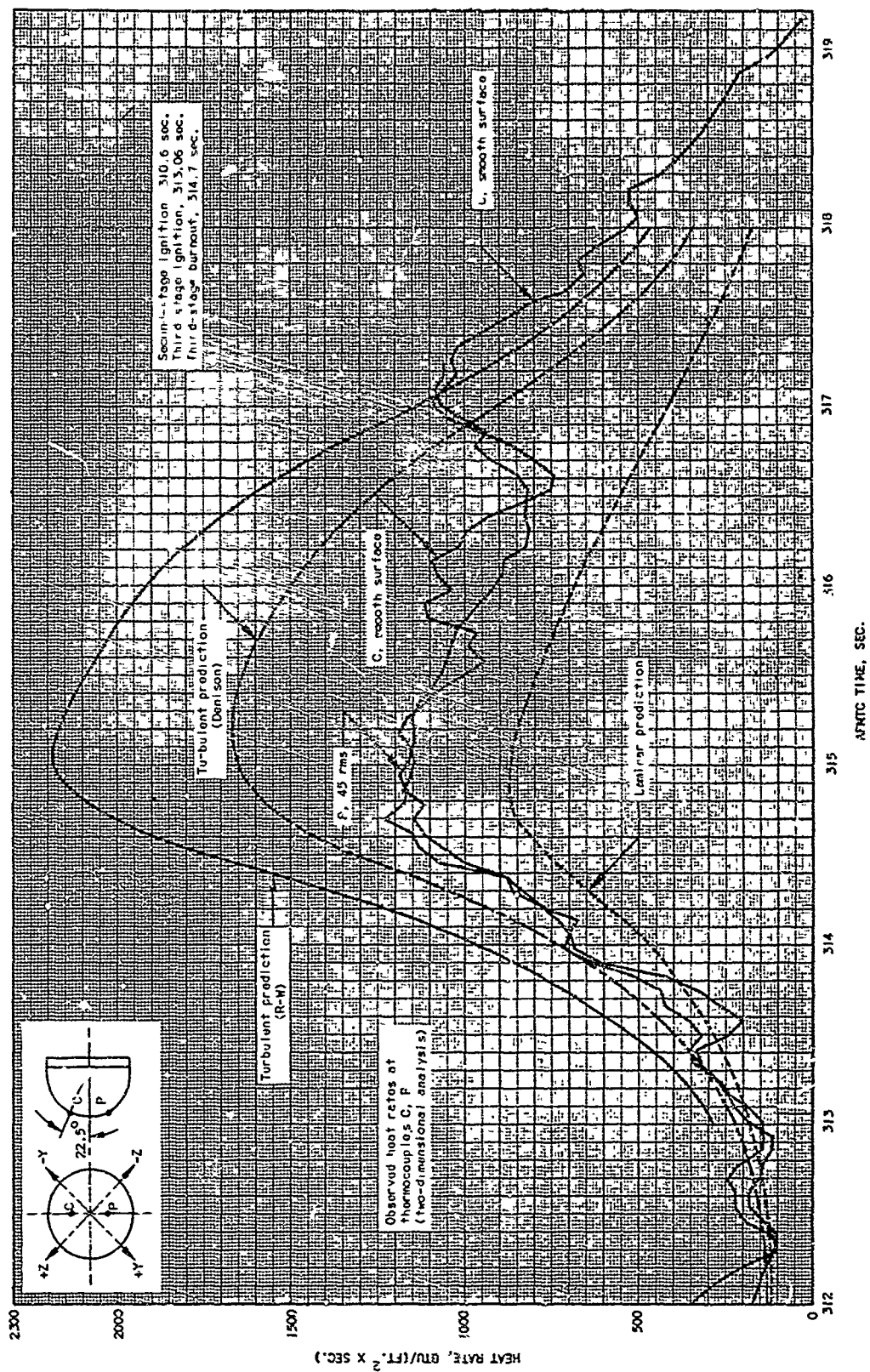


Fig. 37. Comparison of Observed and Predicted Heat Rates at Thermocouples C and P

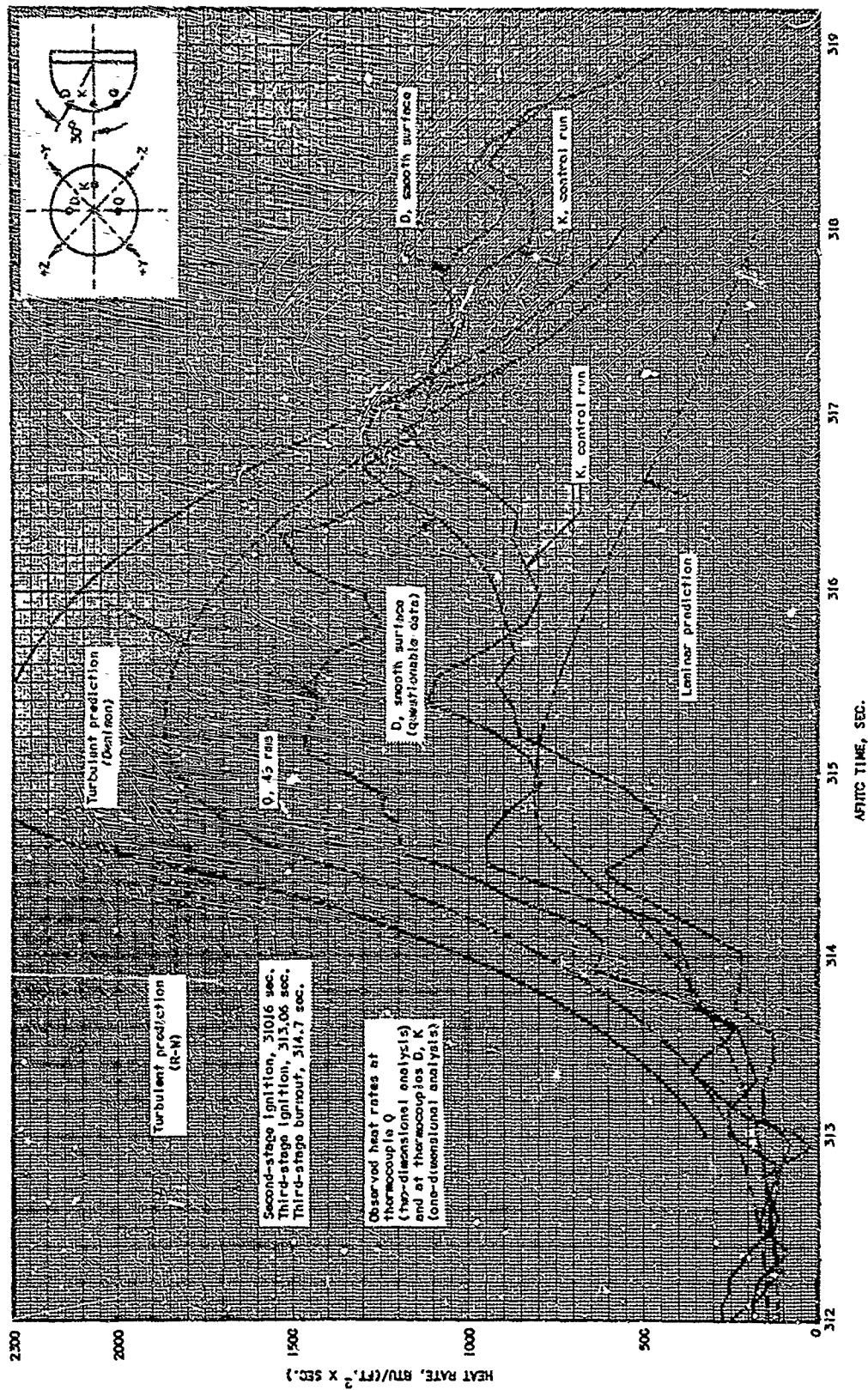


Fig. 38. Comparison of Observed and Predicted Heat Rates of Thermocouples D, K, and Q

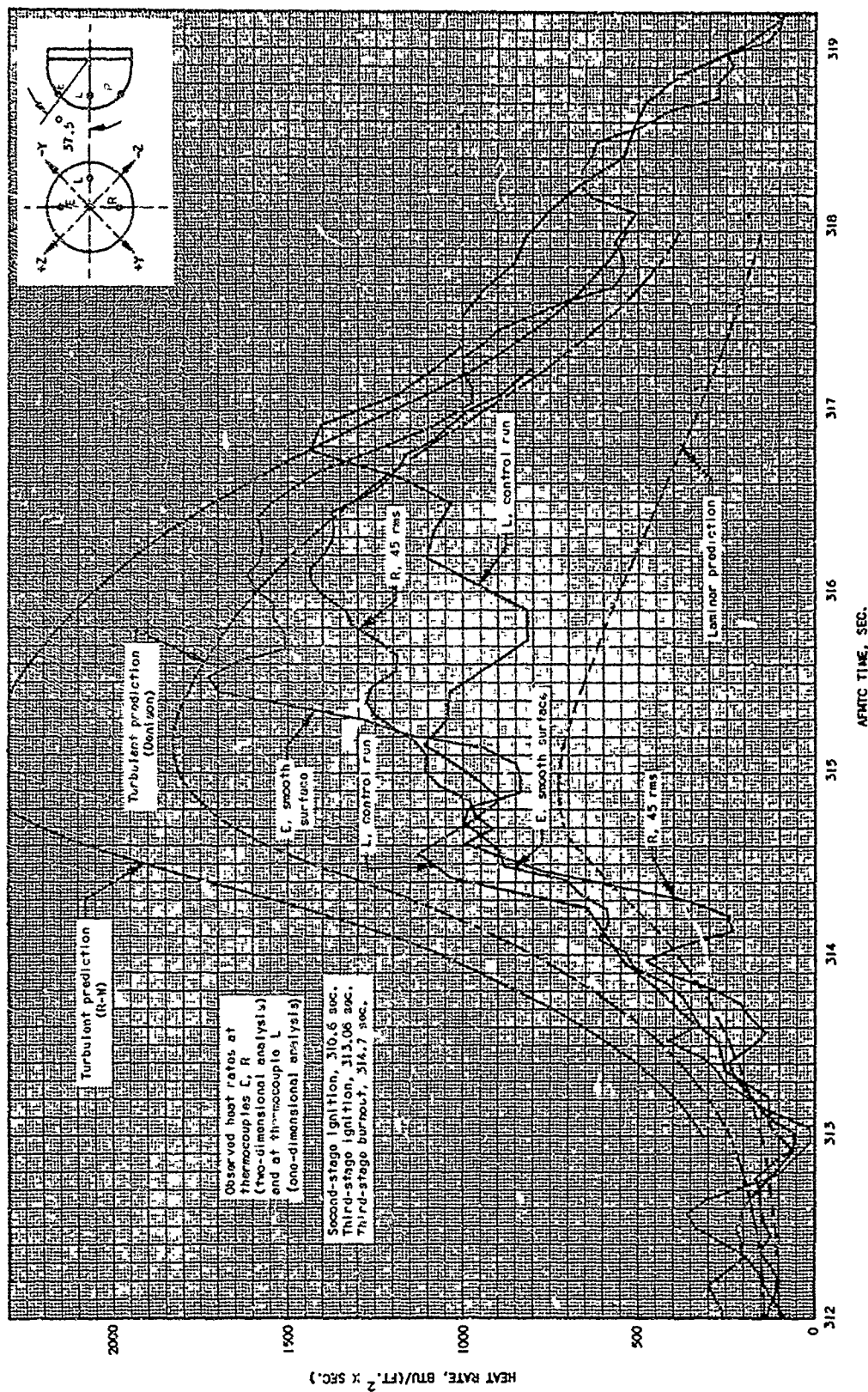


Fig. 39. Comparison of Observed and Predicted Heat Rates at Thermocouples E, L, and R

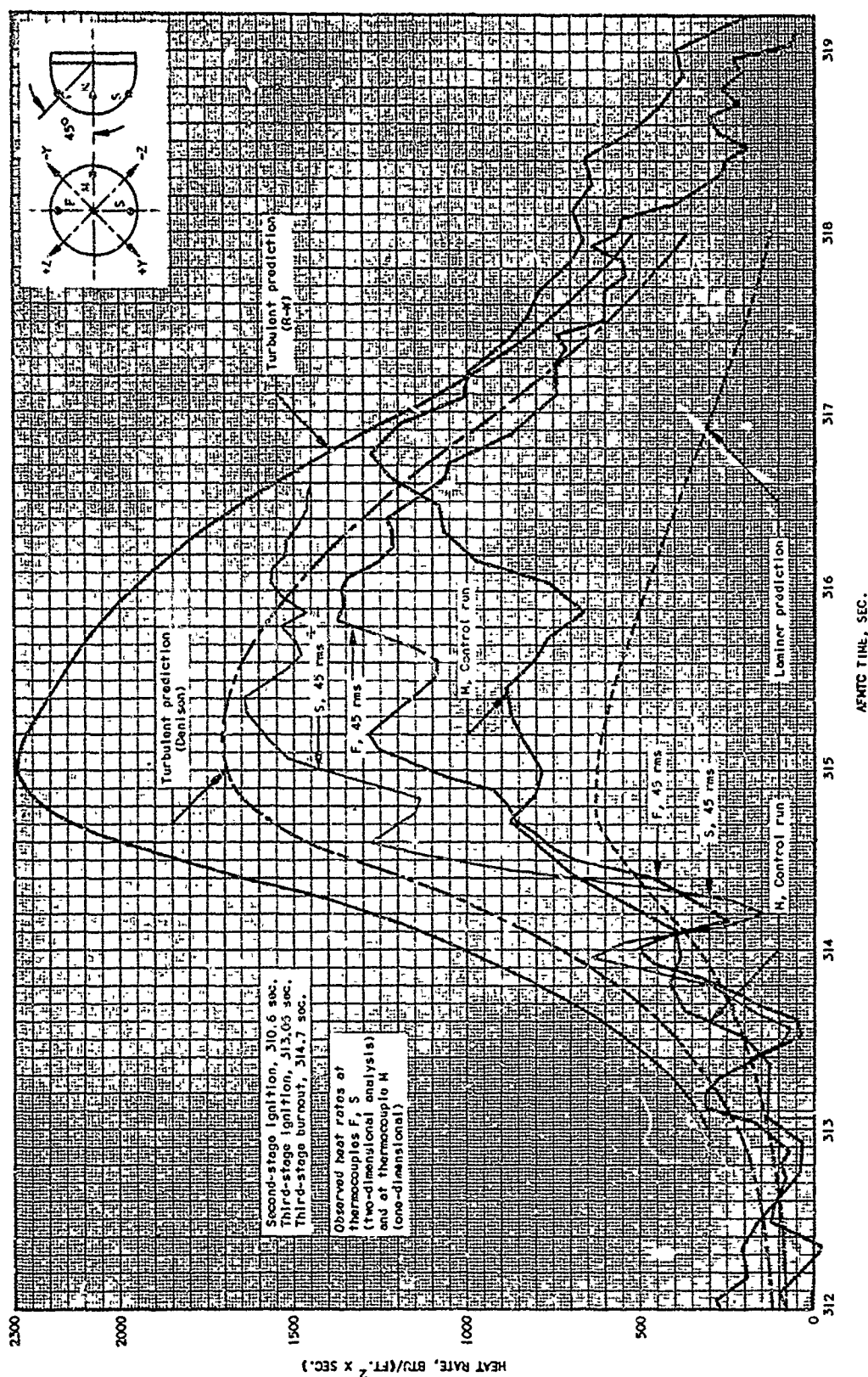


Fig. 40. Comparison of Observed and Predicted Heat Rates of Thermocouples F, M, and S

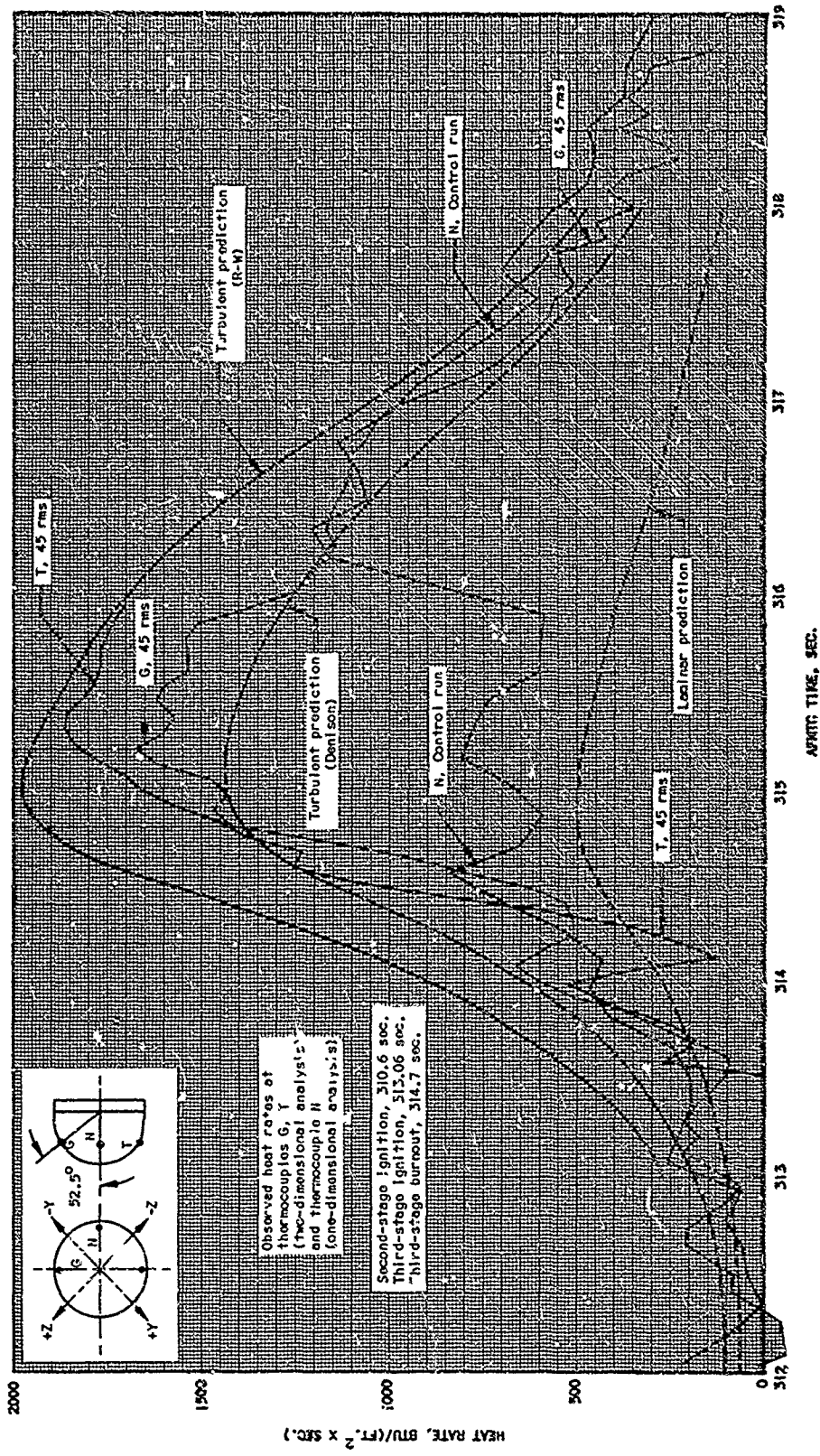


Fig. 41. Comparison of Observed and Predicted Heat Rates at Thermocouples G, N, and T

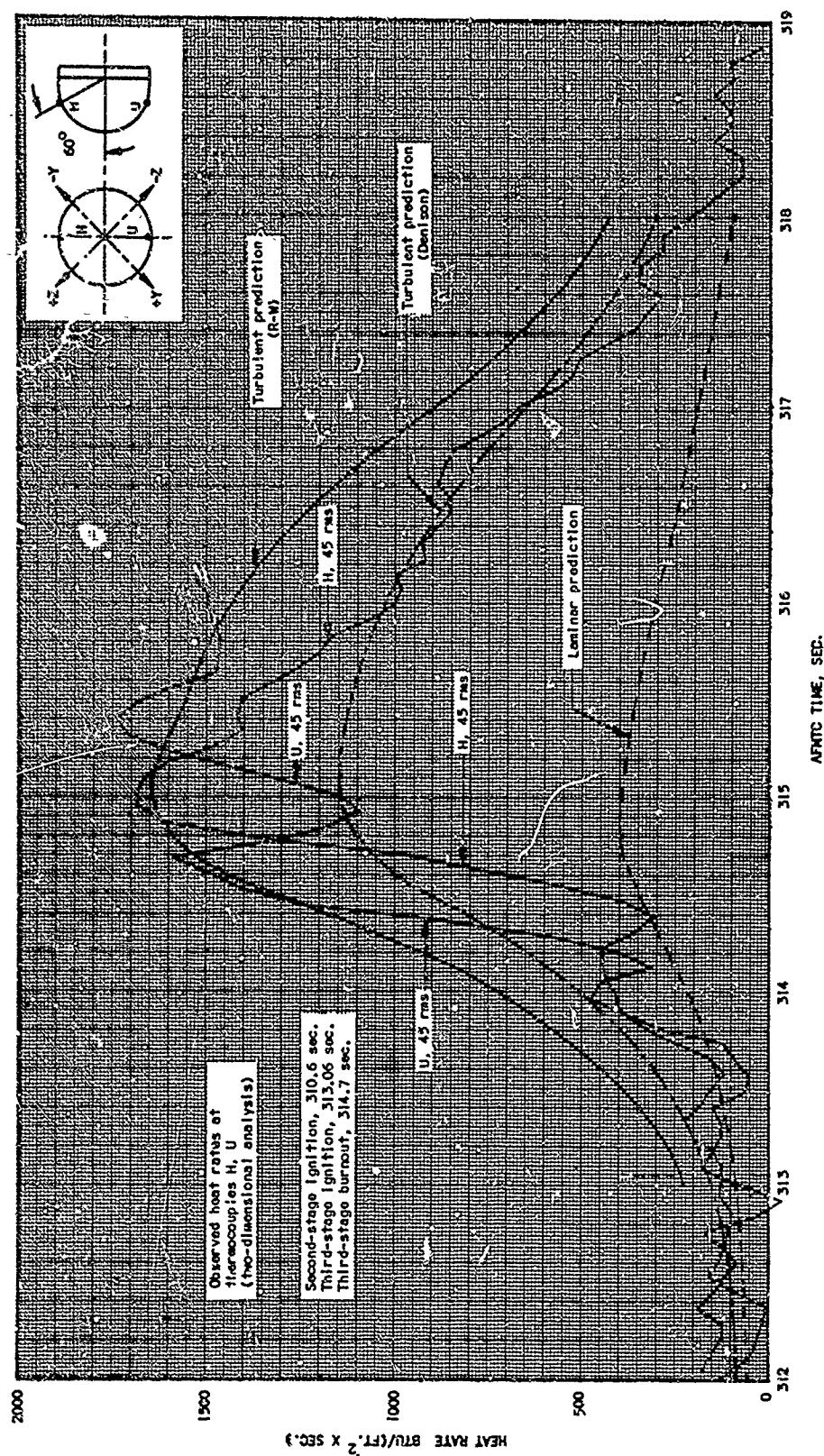


Fig. 42. Comparison of Observed and Predicted Heat Rates at Thermocouples H and U

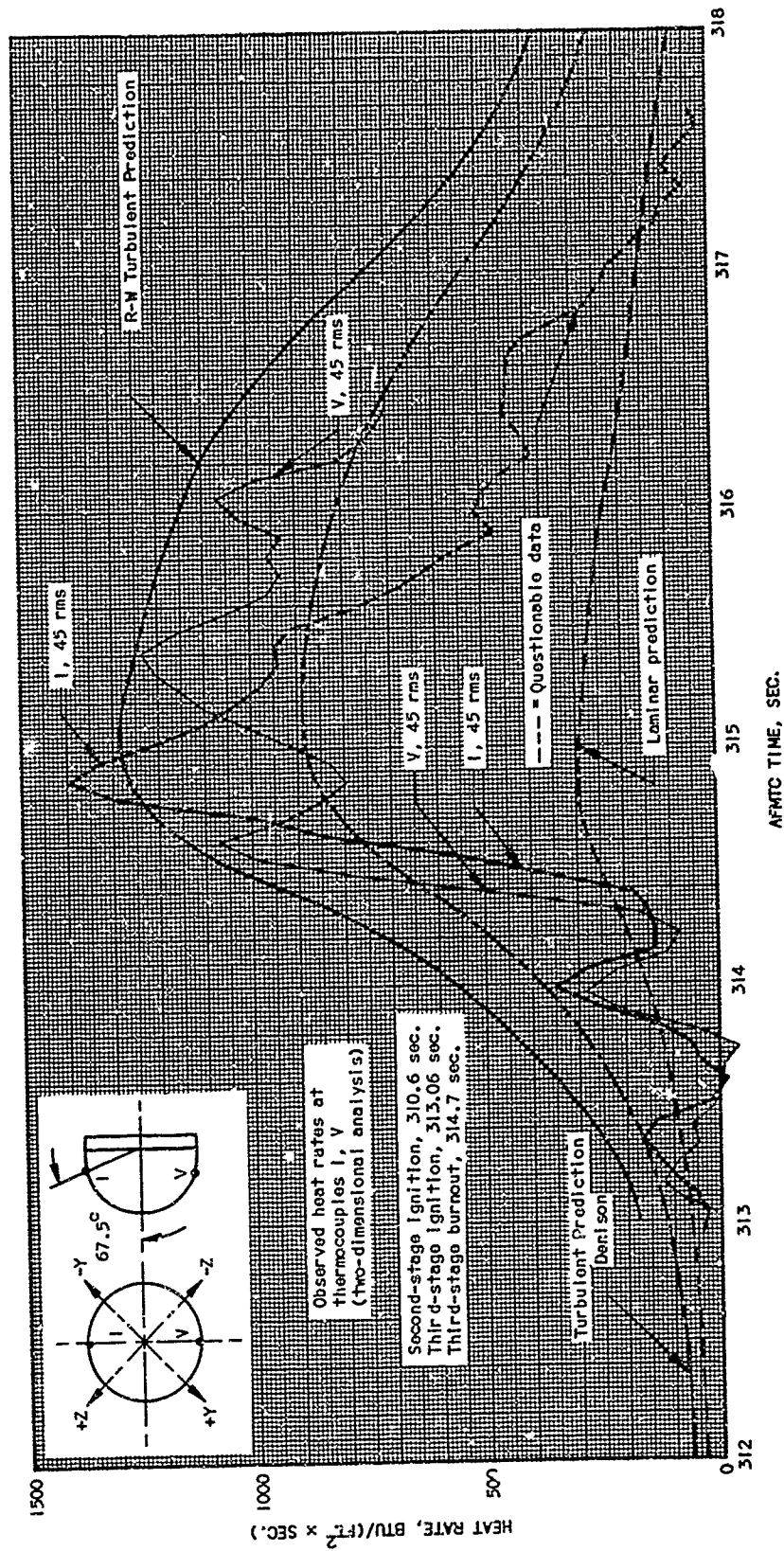


Fig. 43. Comparison of Observed and Predicted Heat Rates at Thermocouples I and V

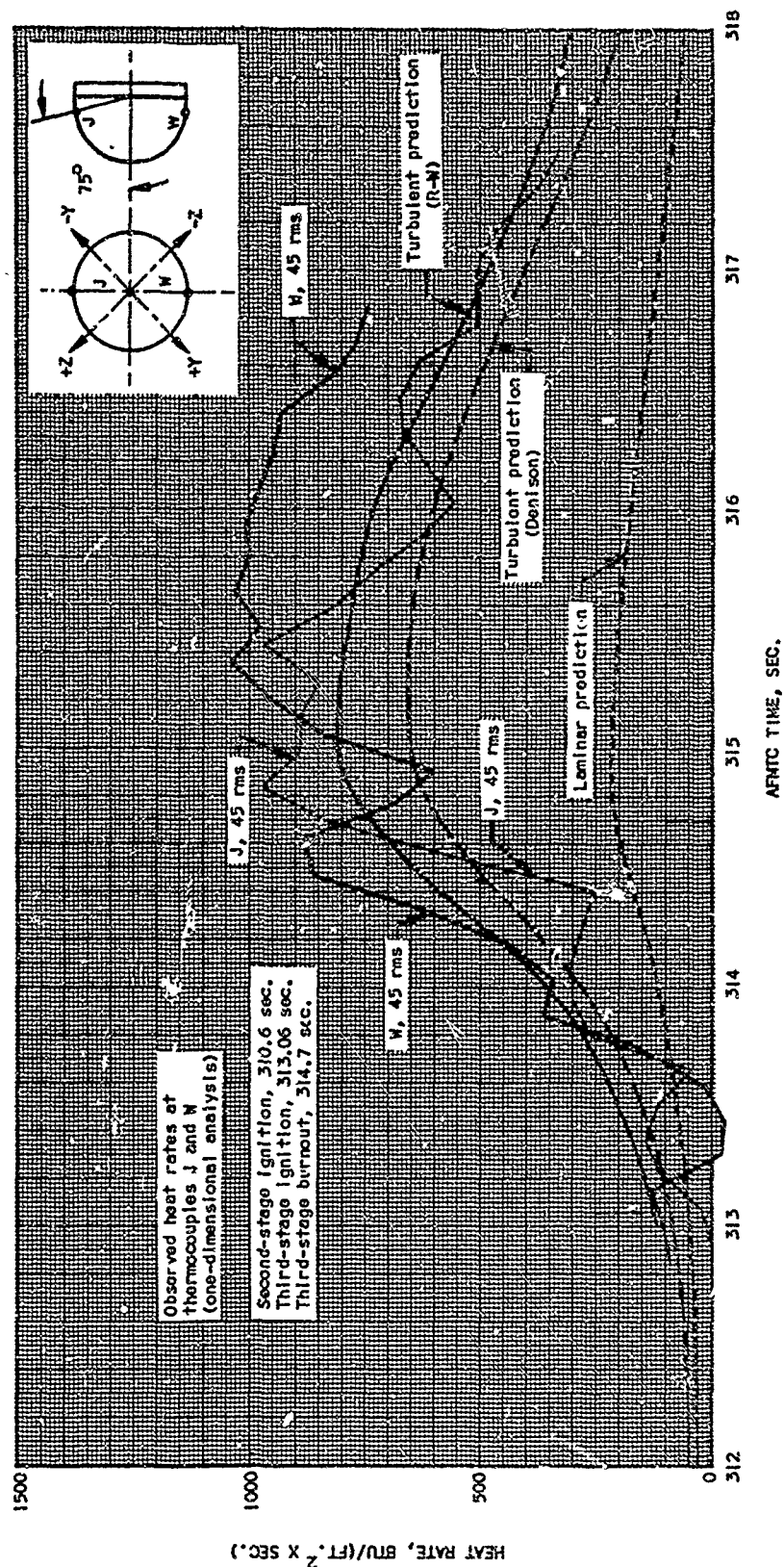


Fig. 44. Comparison of Observed and Predicted Heat Rates at Thermocouples J and W

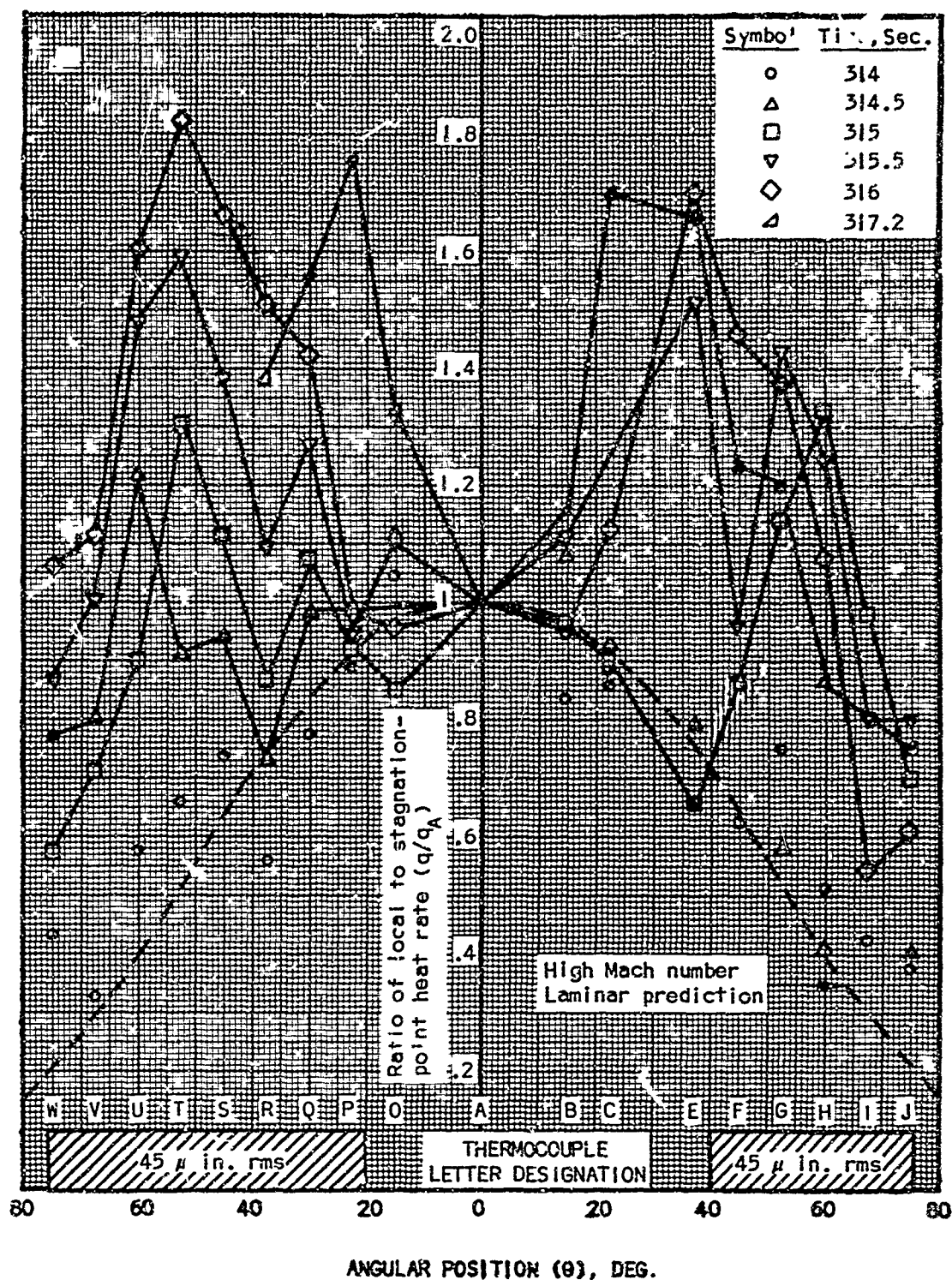


Fig. 45. Heat-Transfer Distributions on the X-17 Nose during Re-Entry, Data from Thermocouples A through J and O through W

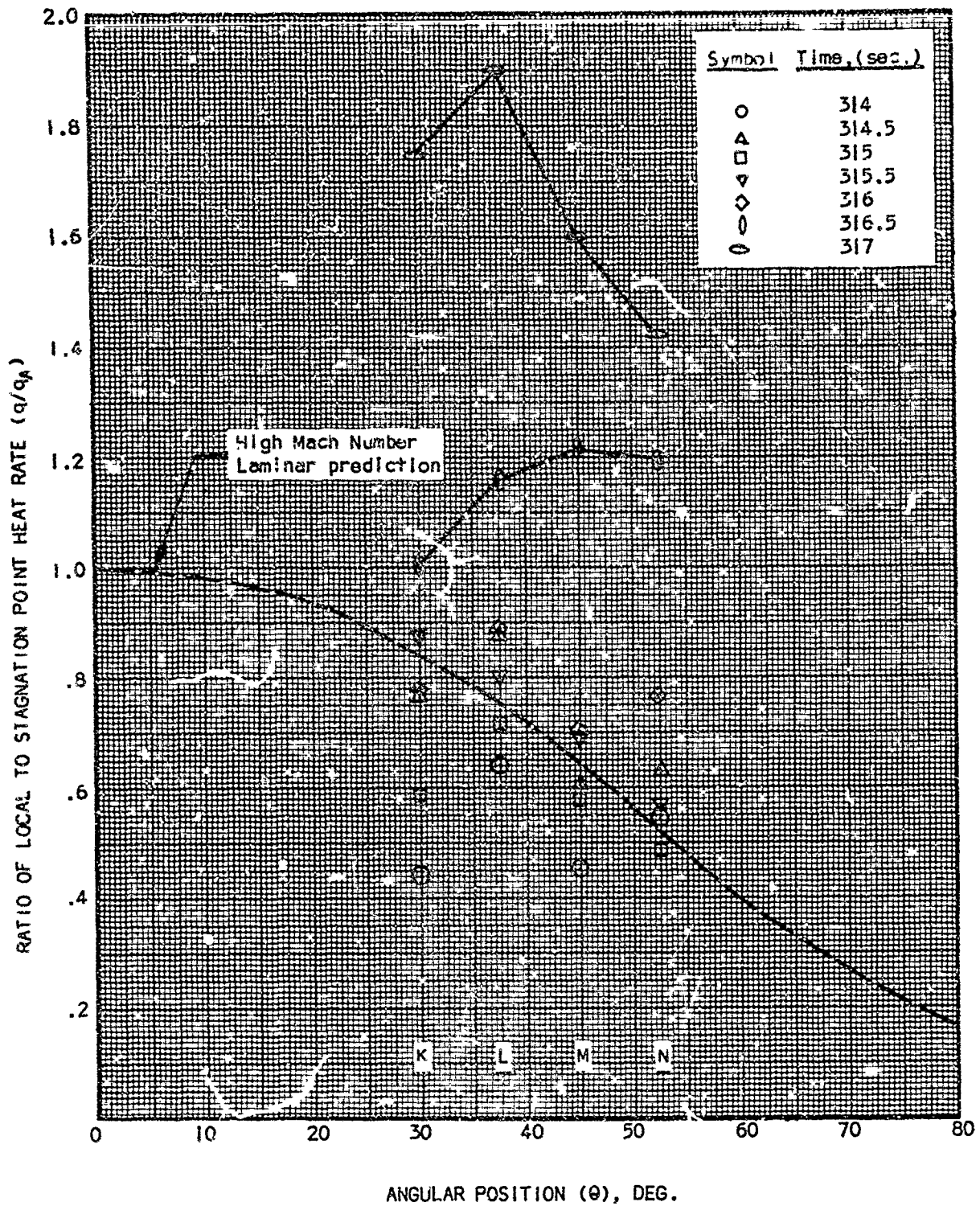


Fig. 46. Heat-Transfer Distributions on the X-17 Nose during Re-Entry, Data from Thermocouples A and K through N

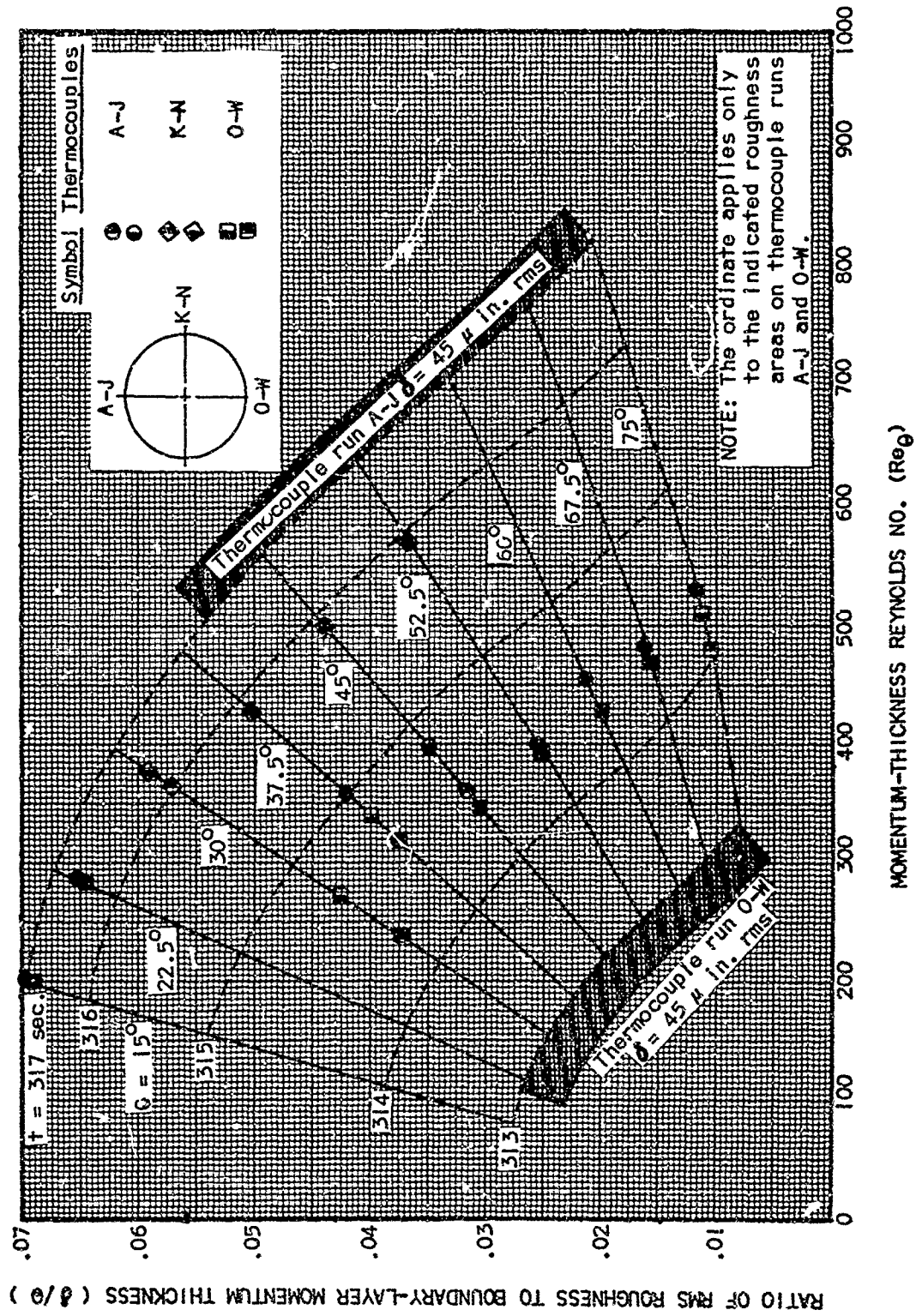


Fig. 47. Ratio of rms Surface Roughness to Momentum Thickness vs. Momentum-Thickness Reynolds Number during Re-Entry

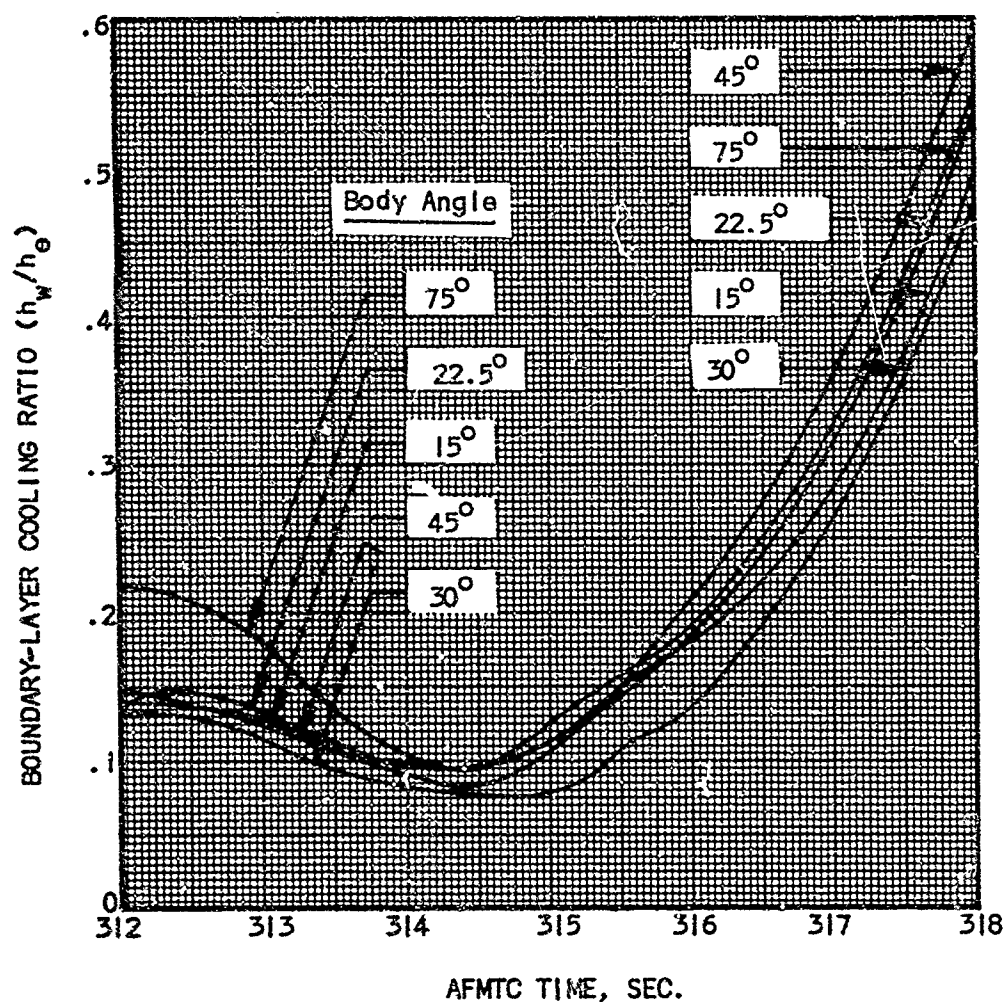


Fig. 48. Boundary-Layer Cooling Ratio during Re-Entry

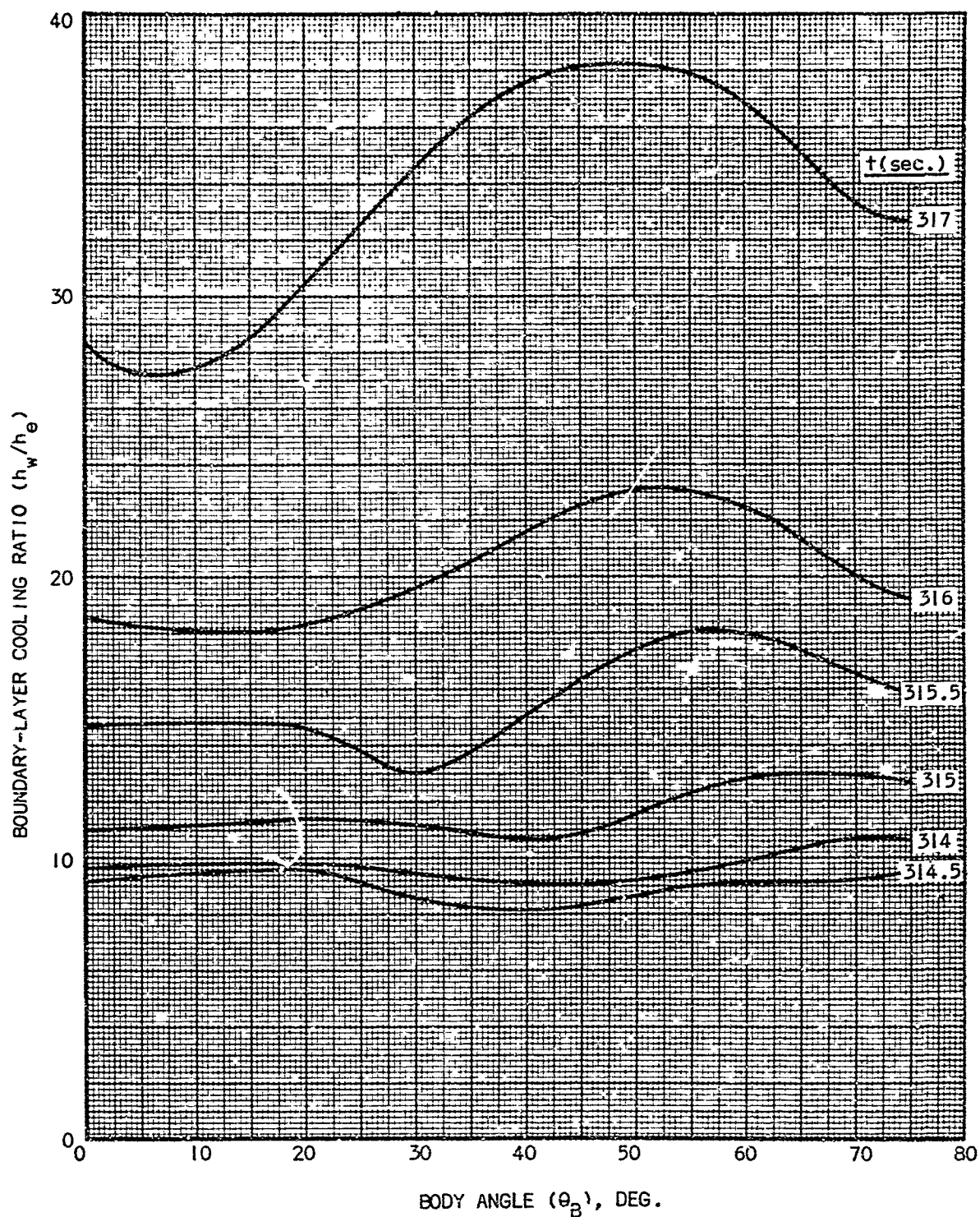


Fig. 49. Boundary-Layer Cooling-Ratio Distribution during Re-Entry

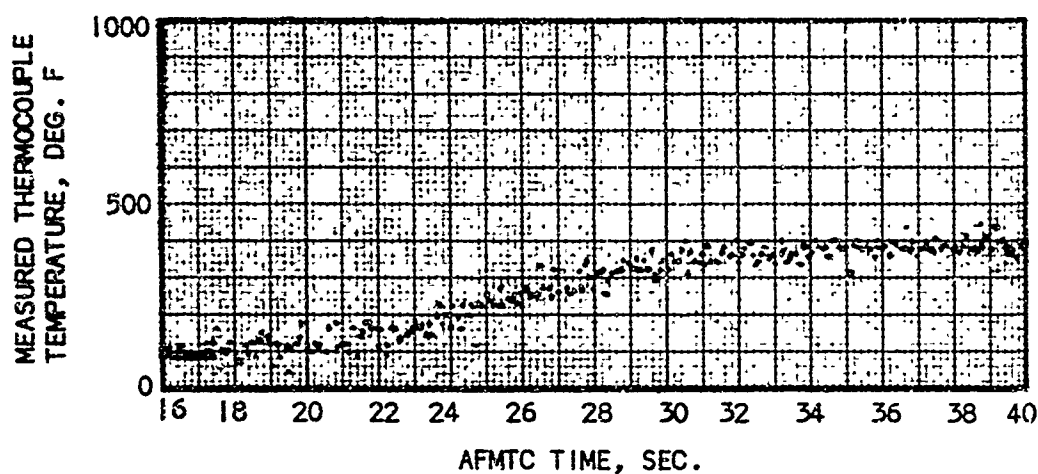


Fig. 50. Typical Temperature Time History during Exit

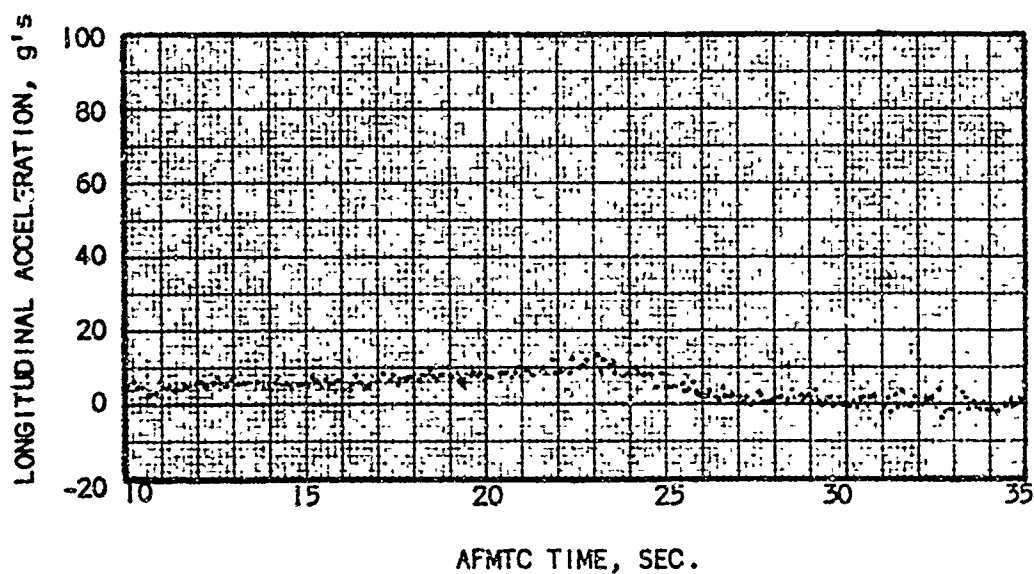


Fig. 51. Longitudinal Accelerations during Exit

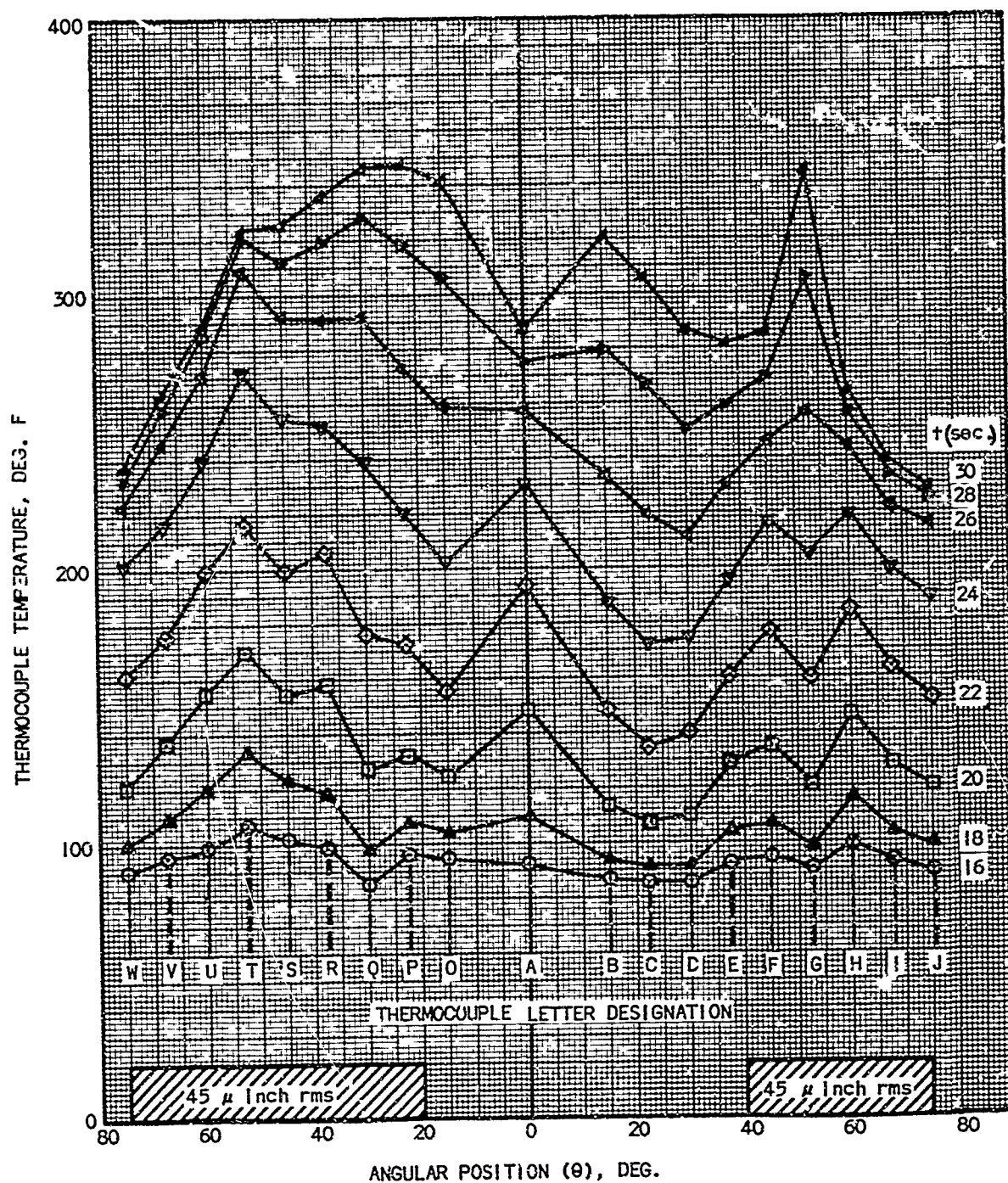


Fig. 52. Comparison of Measured Temperatures on Long and Short Roughness Runs during Exit

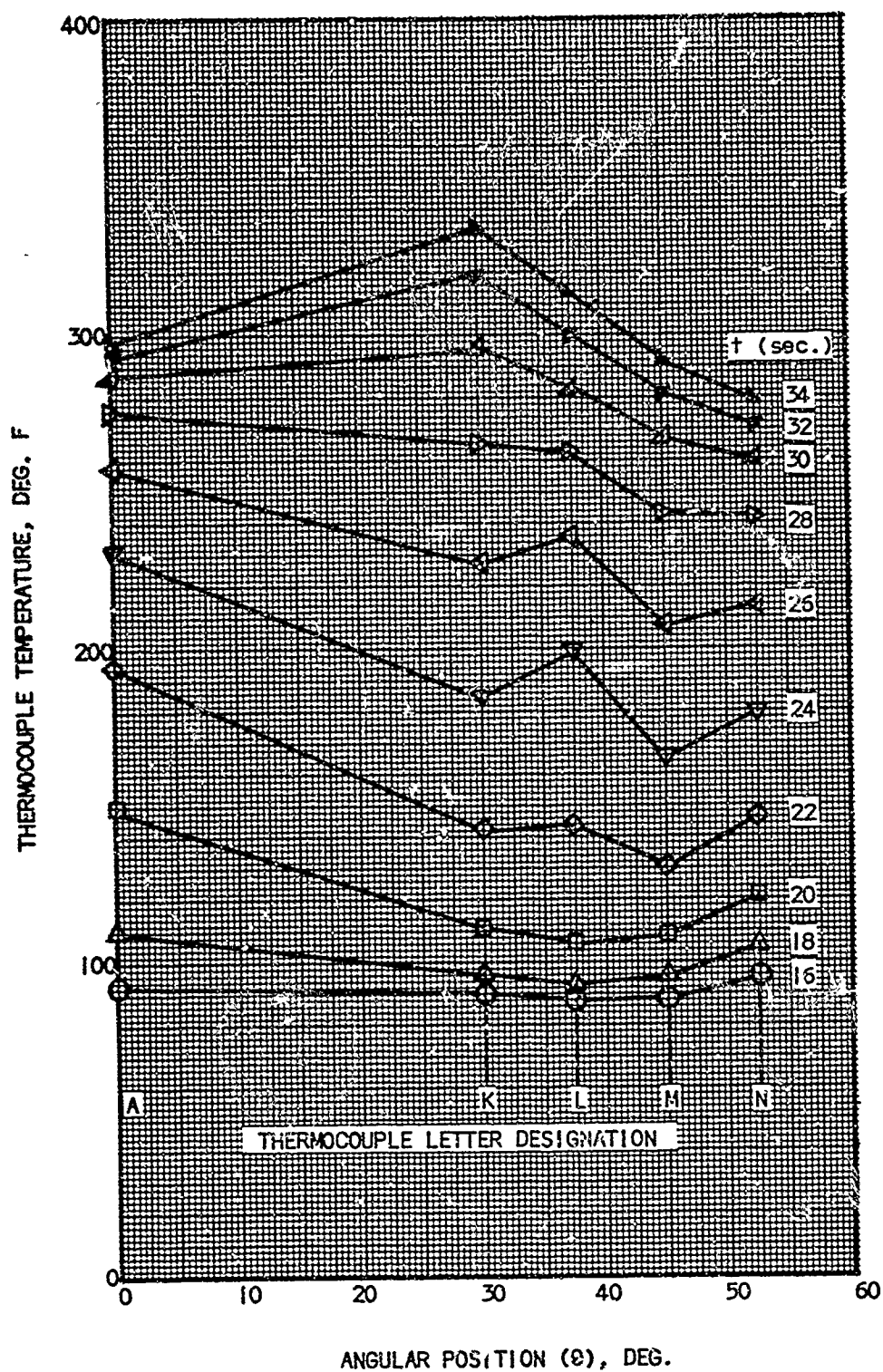


Fig. 53. Temperature Profiles on the Nose during Exit, Data from Thermocouples A and K through N

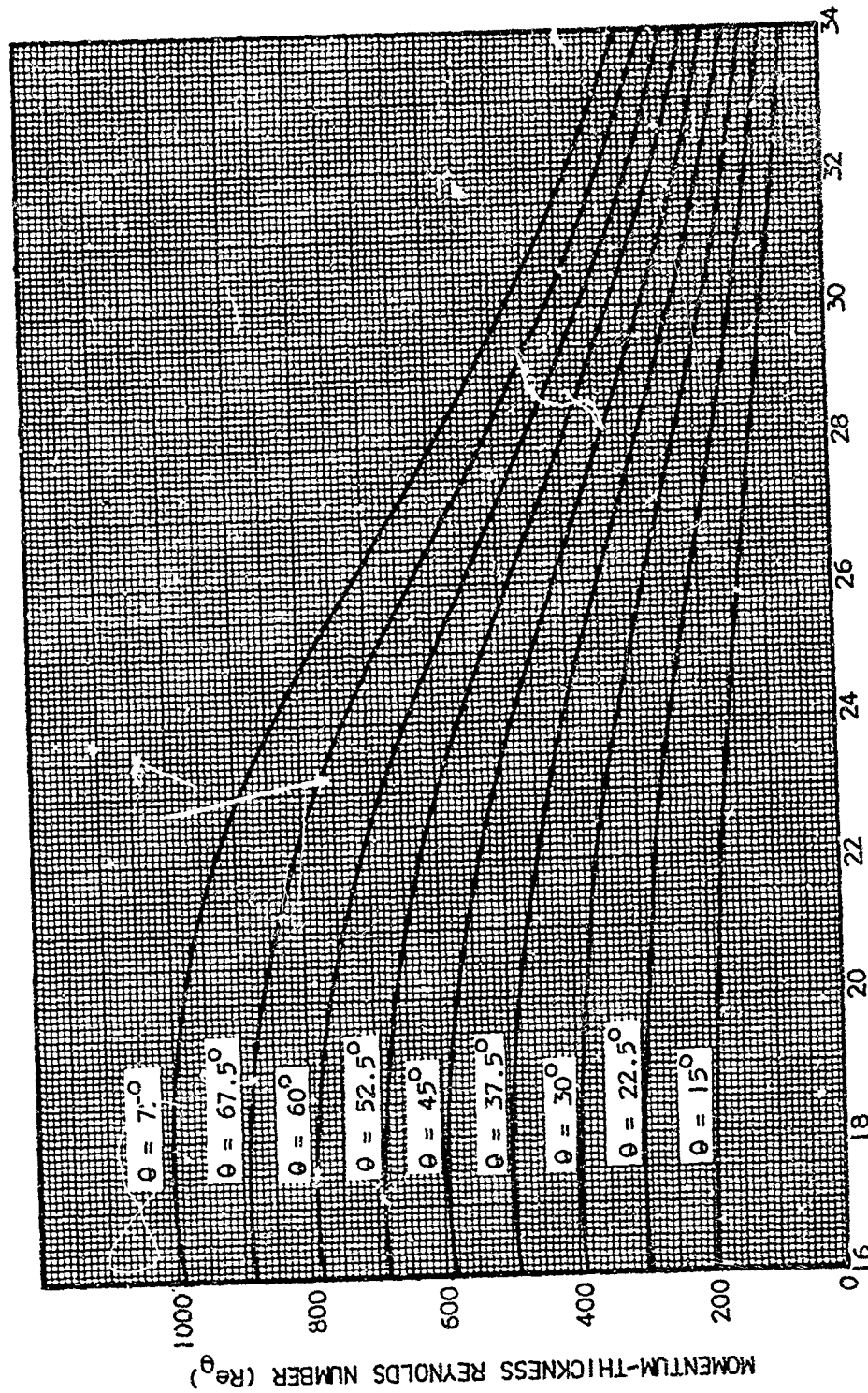


Fig. 54. Momentum-Thickness Reynolds Number during Exit

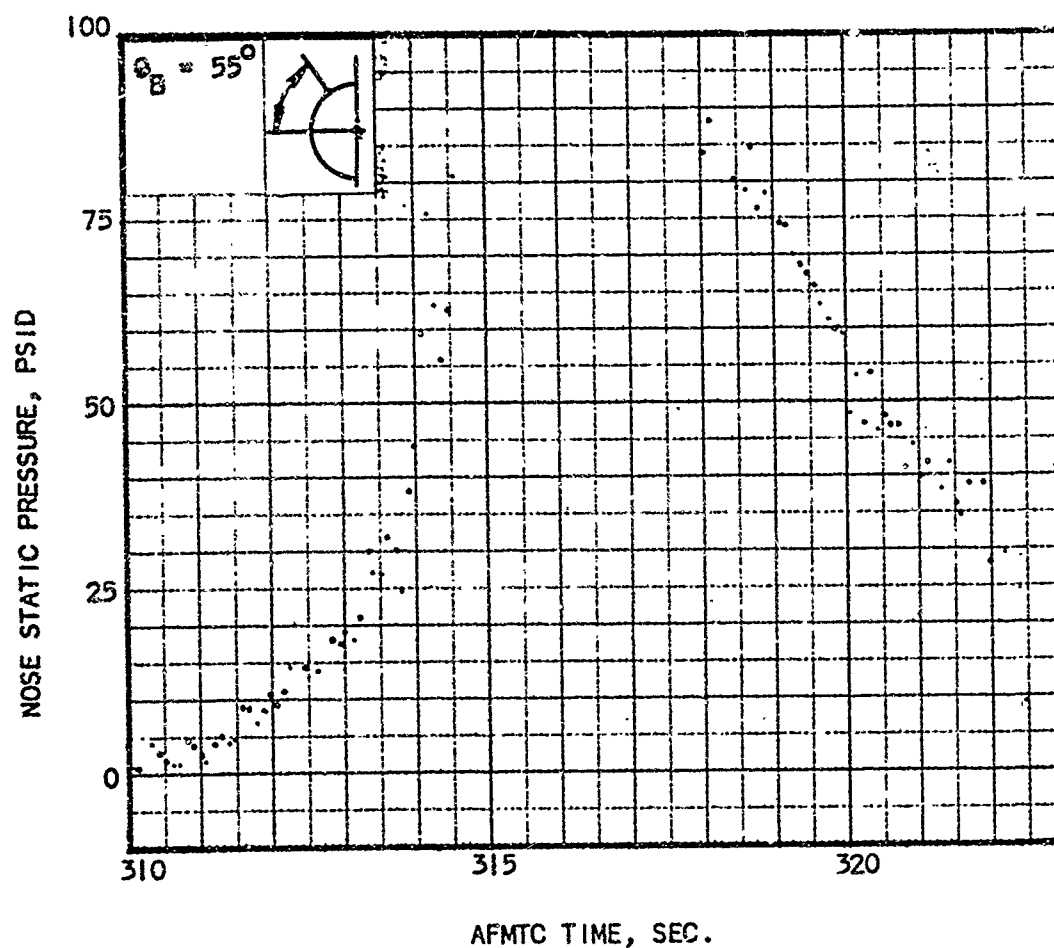


Fig. 55. Measured Pressures at R-26 Orifice Locations during Re-entry, Pressure Orifice A

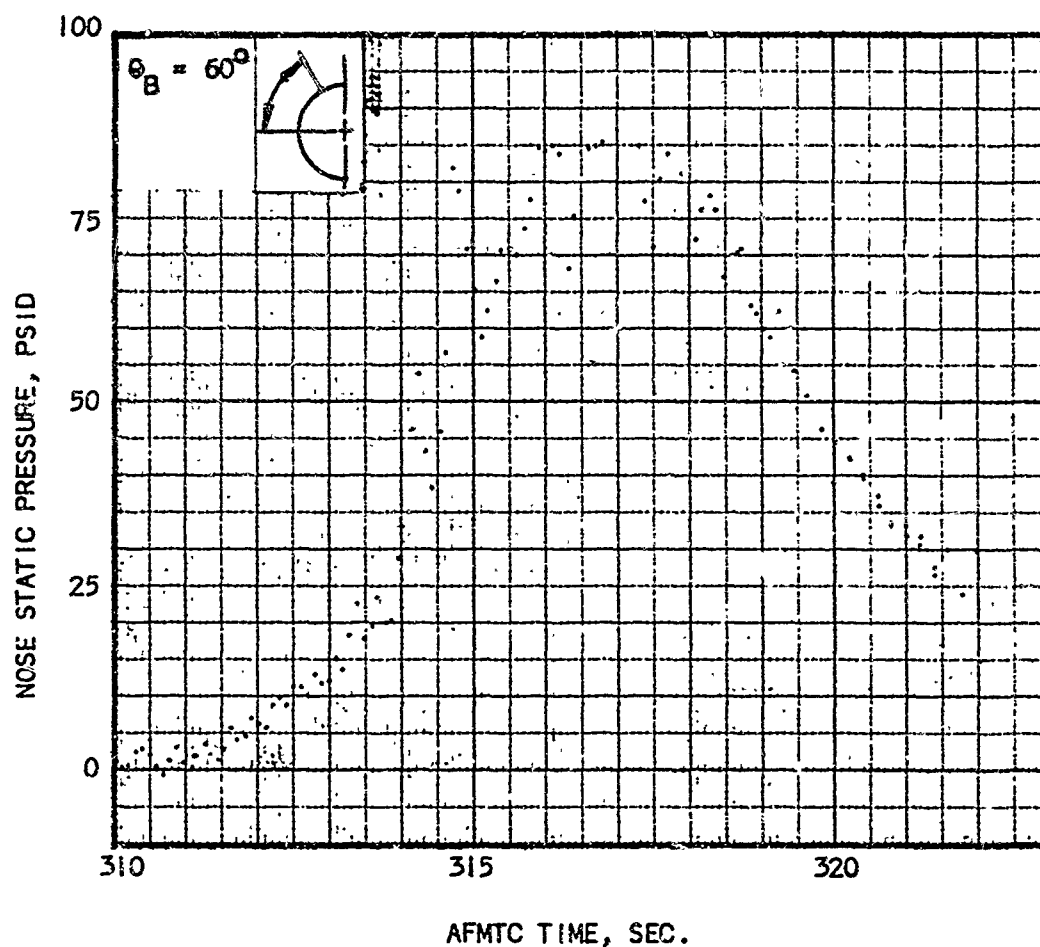


Fig. 56. Measured Pressures at R-26 Orifice Locations during Re-entry, Pressure Orifice B

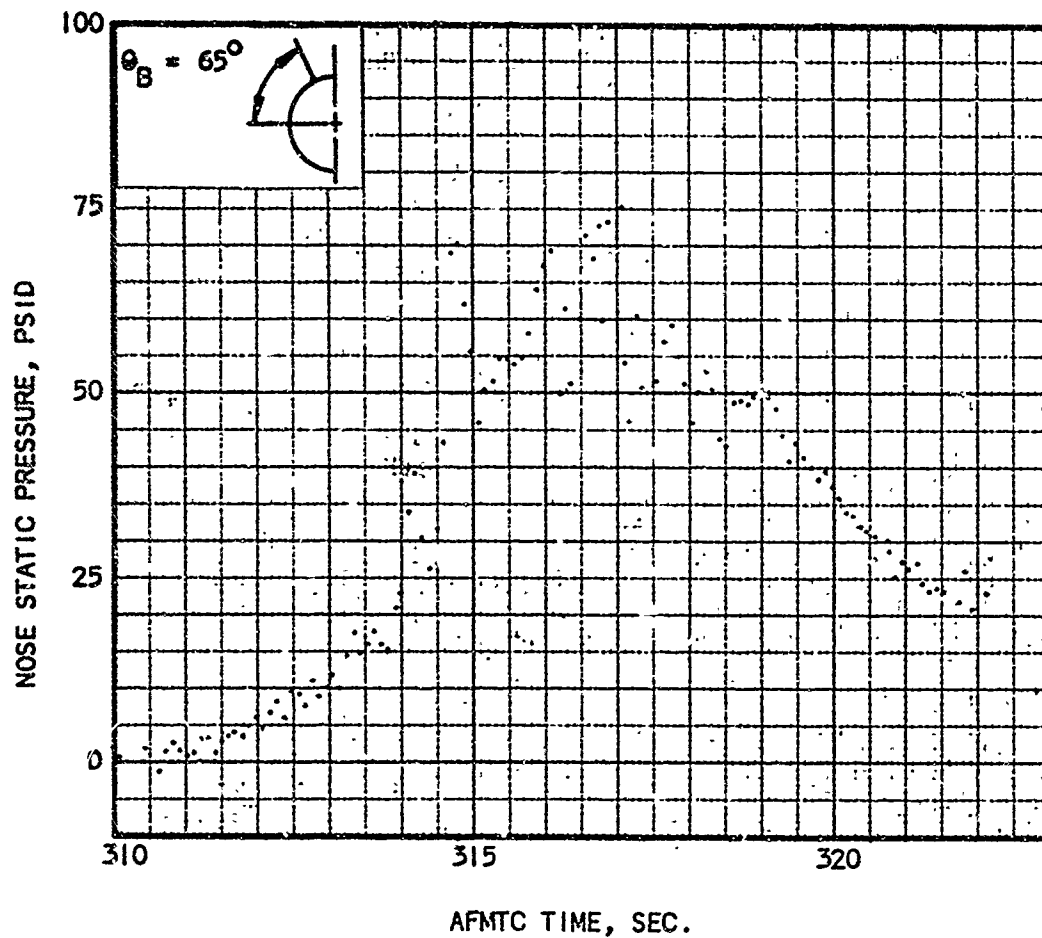


Fig. 57. Measured Pressures at R-26 Orifice Locations during Re-entry, Pressure Orifice C

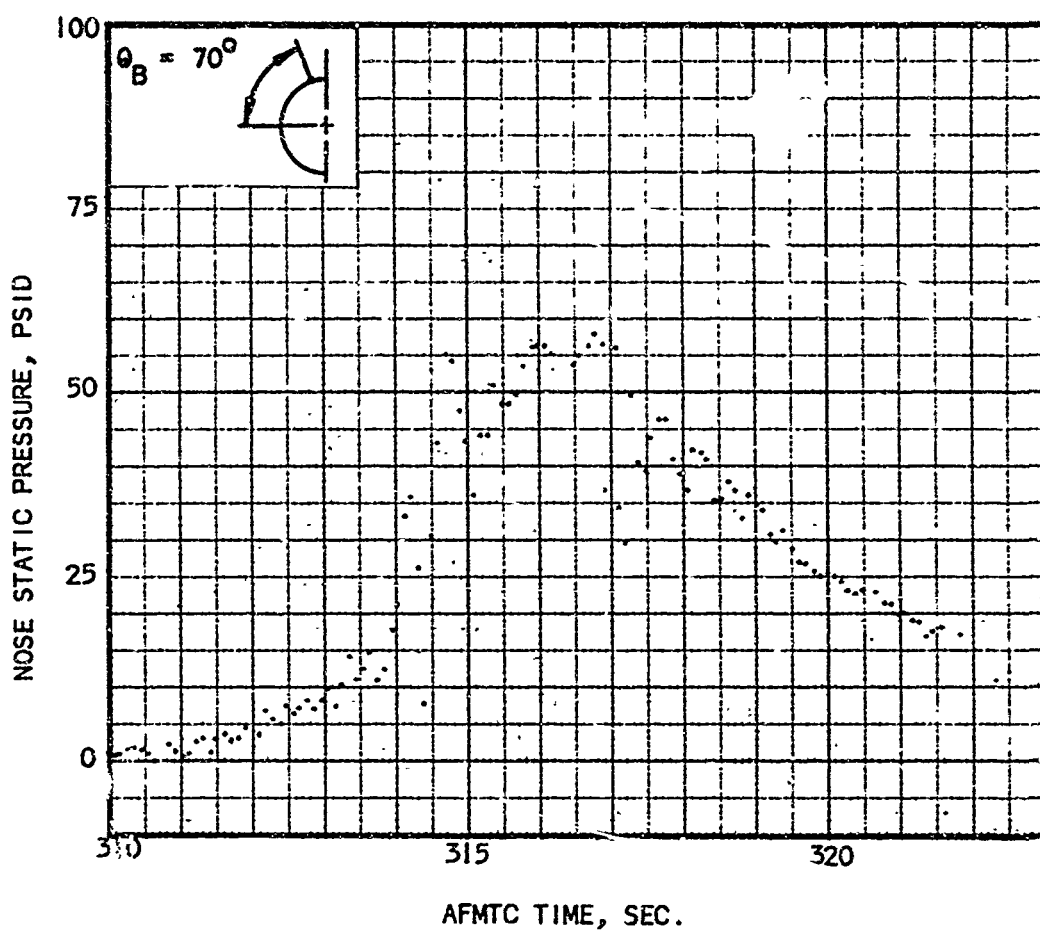


Fig. 58. Measured Pressures at R-26 Orifice Locations during Re-entry, Pressure Orifice D

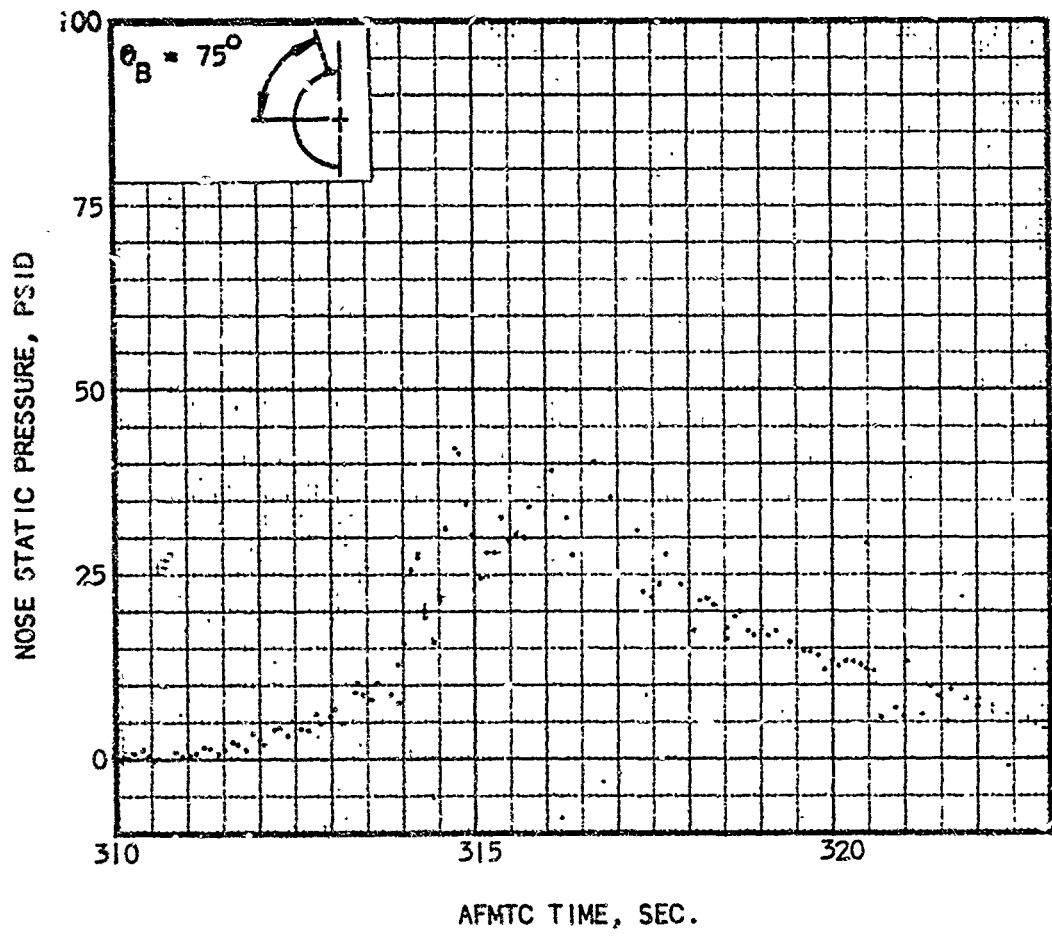


Fig. 59. Measured Pressures at R-426 Orifice Locations during Re-entry, Pressure Orifice E

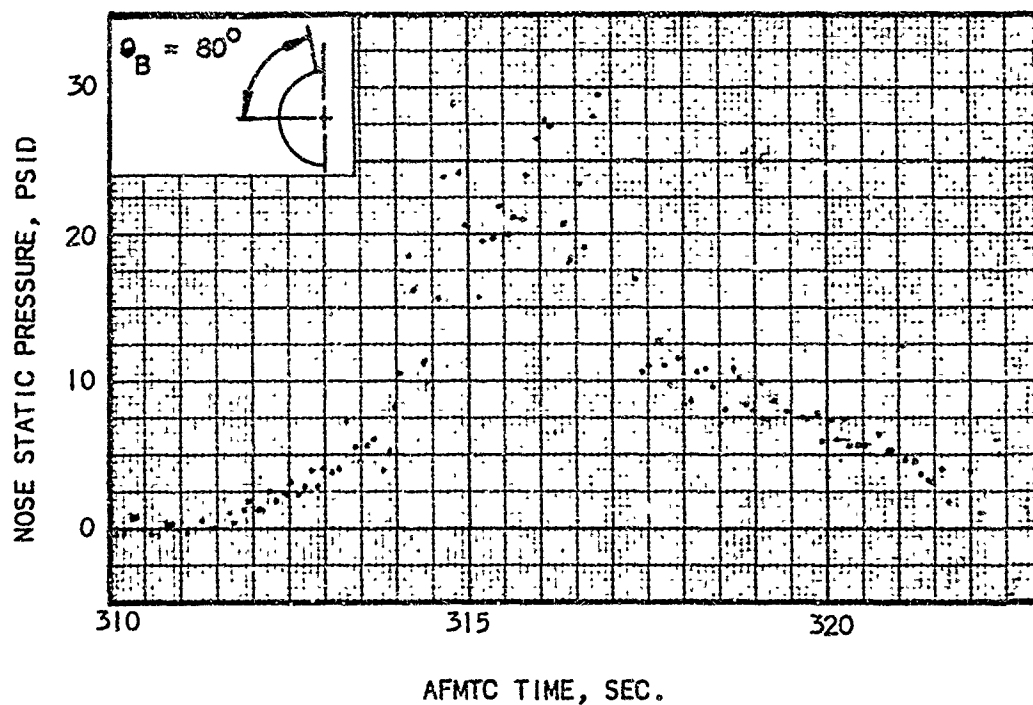


Fig. 60. Measured Pressures at R-26 Orifice Locations during Re-entry, Pressure Orifice F

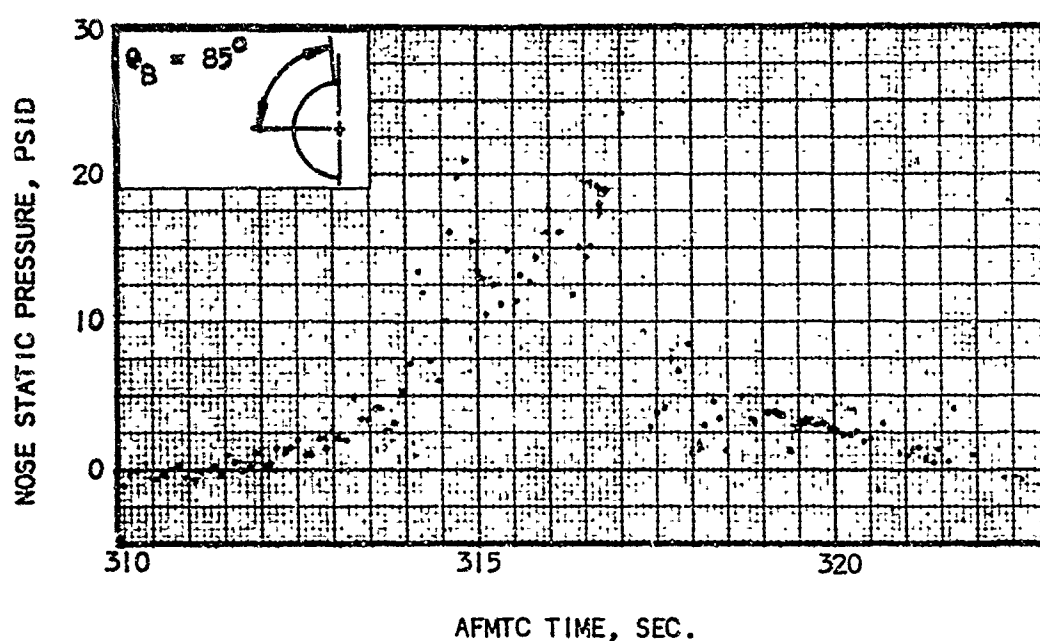


Fig. 61. Measured Pressures at R-26 Orifice Locations during Re-entry, Pressure Orifice G

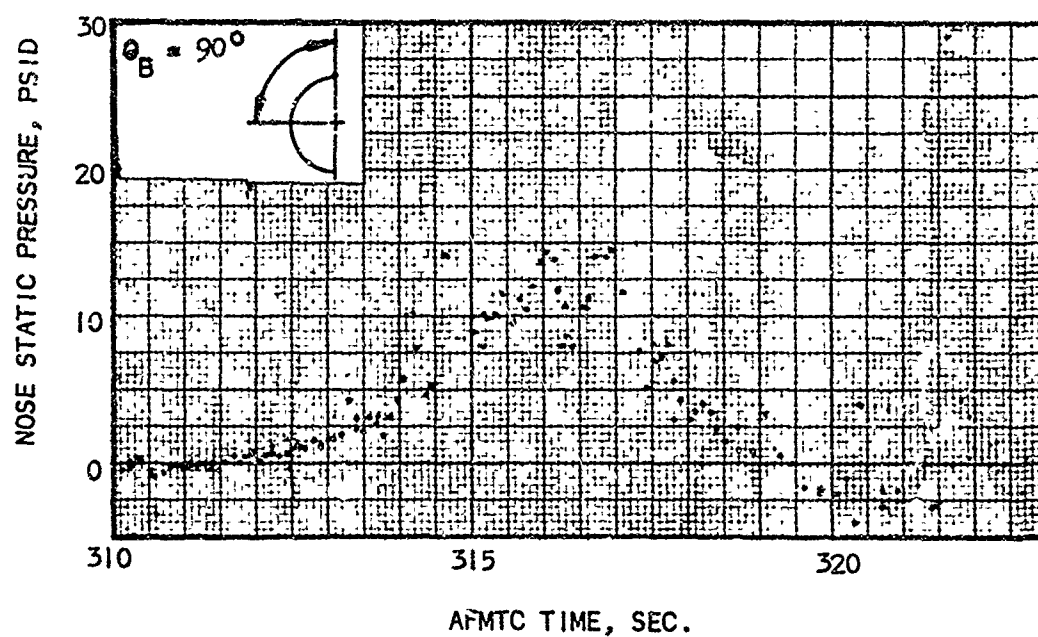


Fig. 62. Measured Pressures at R-26 Orifice Locations during Re-entry, Pressure Orifice H

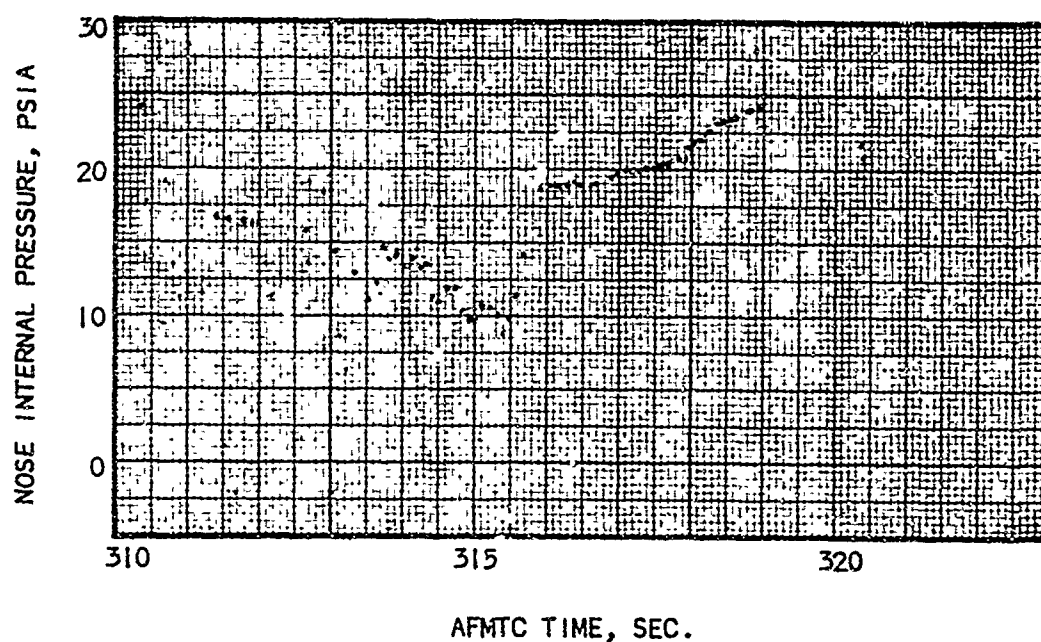


Fig. 63. Measured Nose Internal Pressure

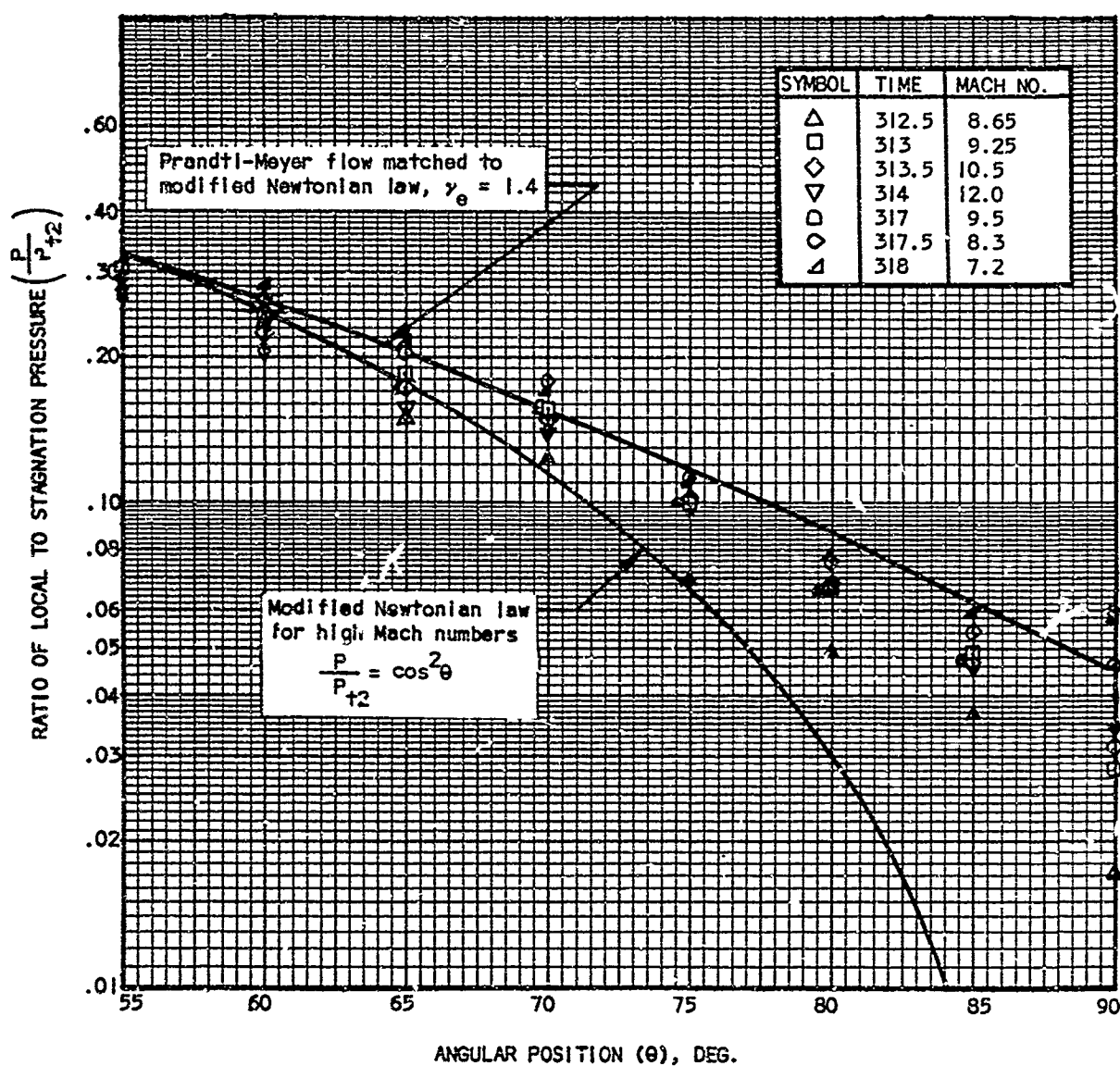


Fig. 64. Comparison of Observed and Predicted Pressures during Re-Entry

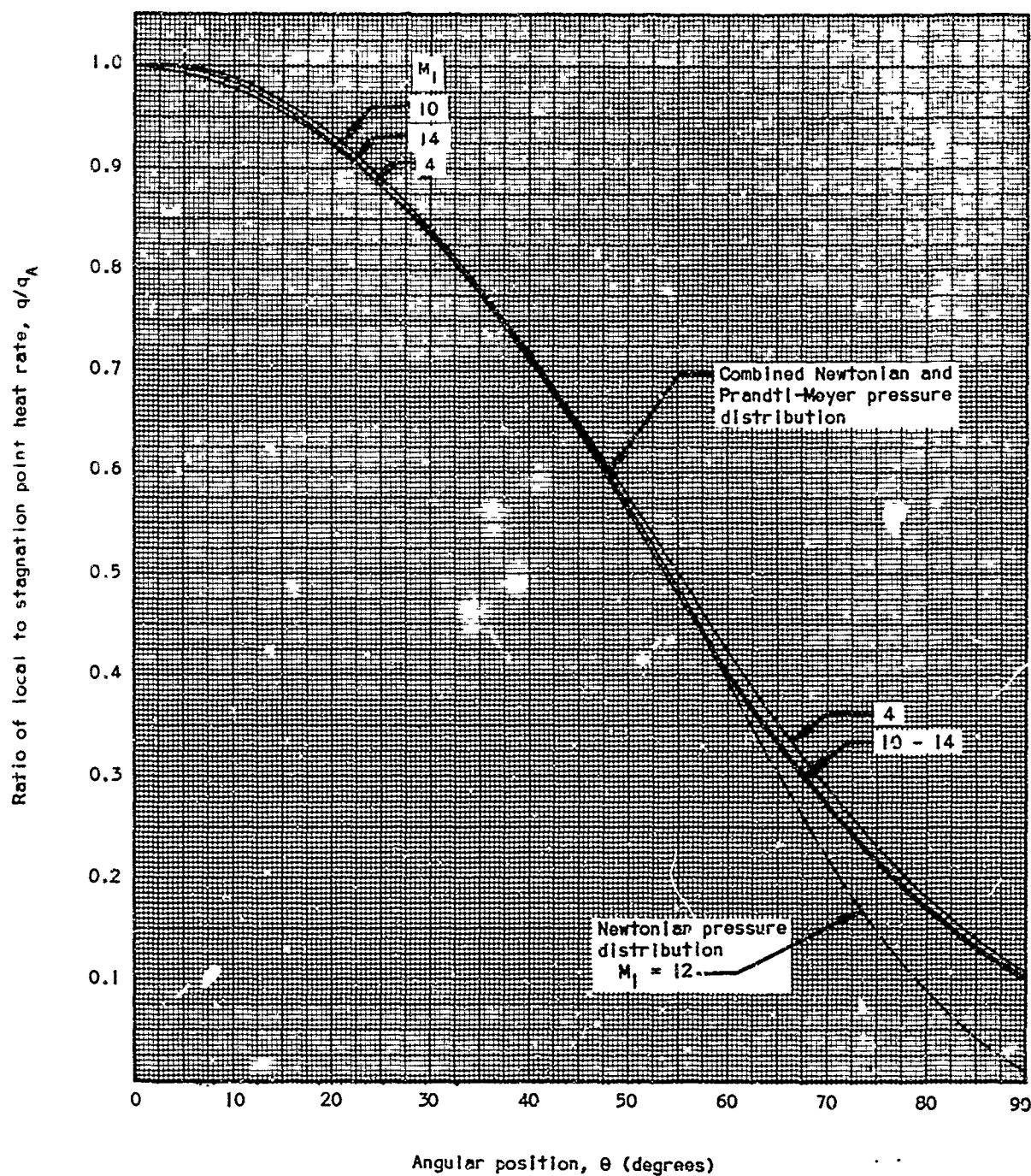


Fig. 65. Theoretical Laminar Heat-Transfer Distribution on a Hemisphere

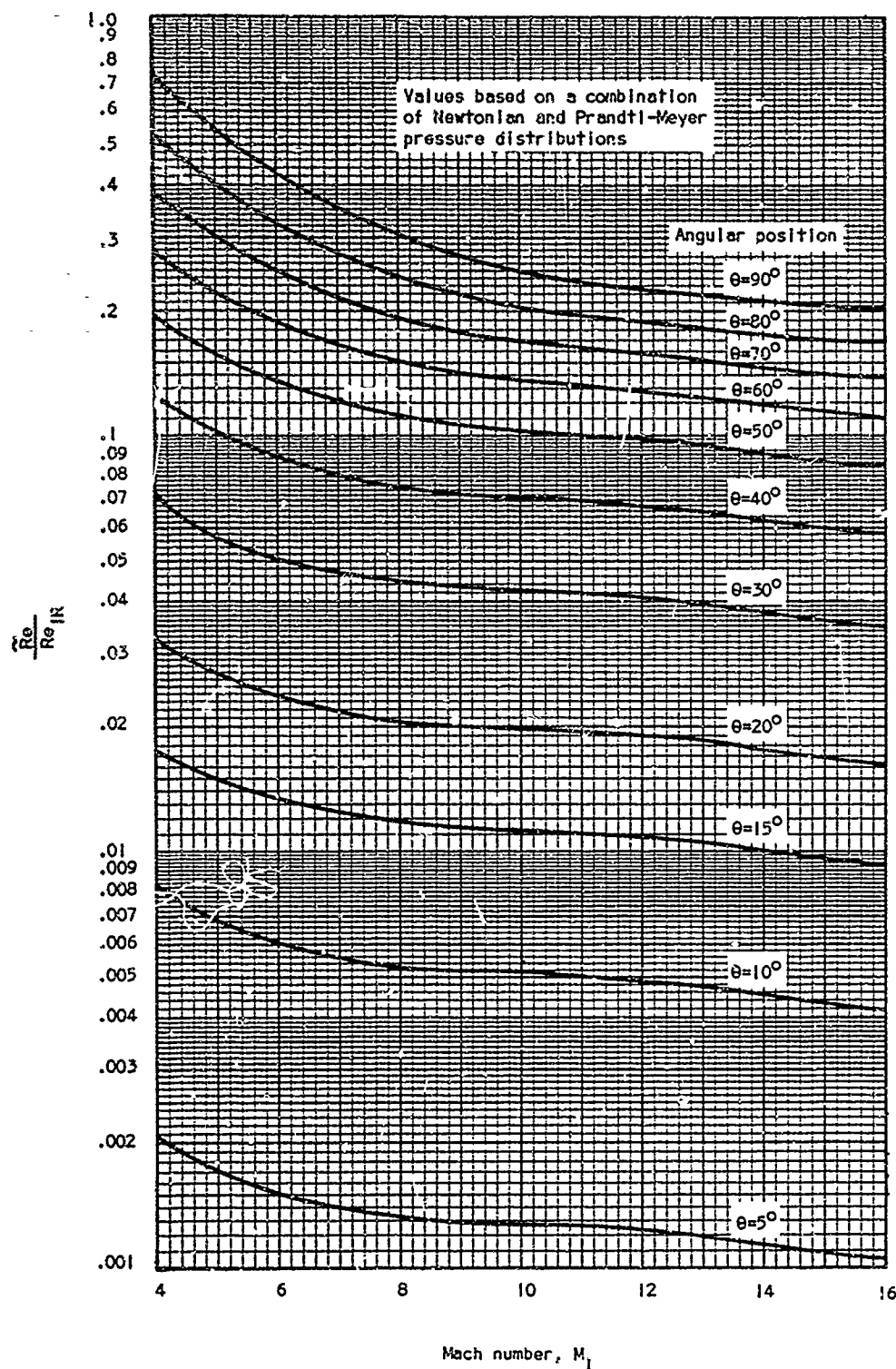


Fig. 66. \tilde{Re}/Re_{IR} as a Function of Angular Position on a Hemisphere

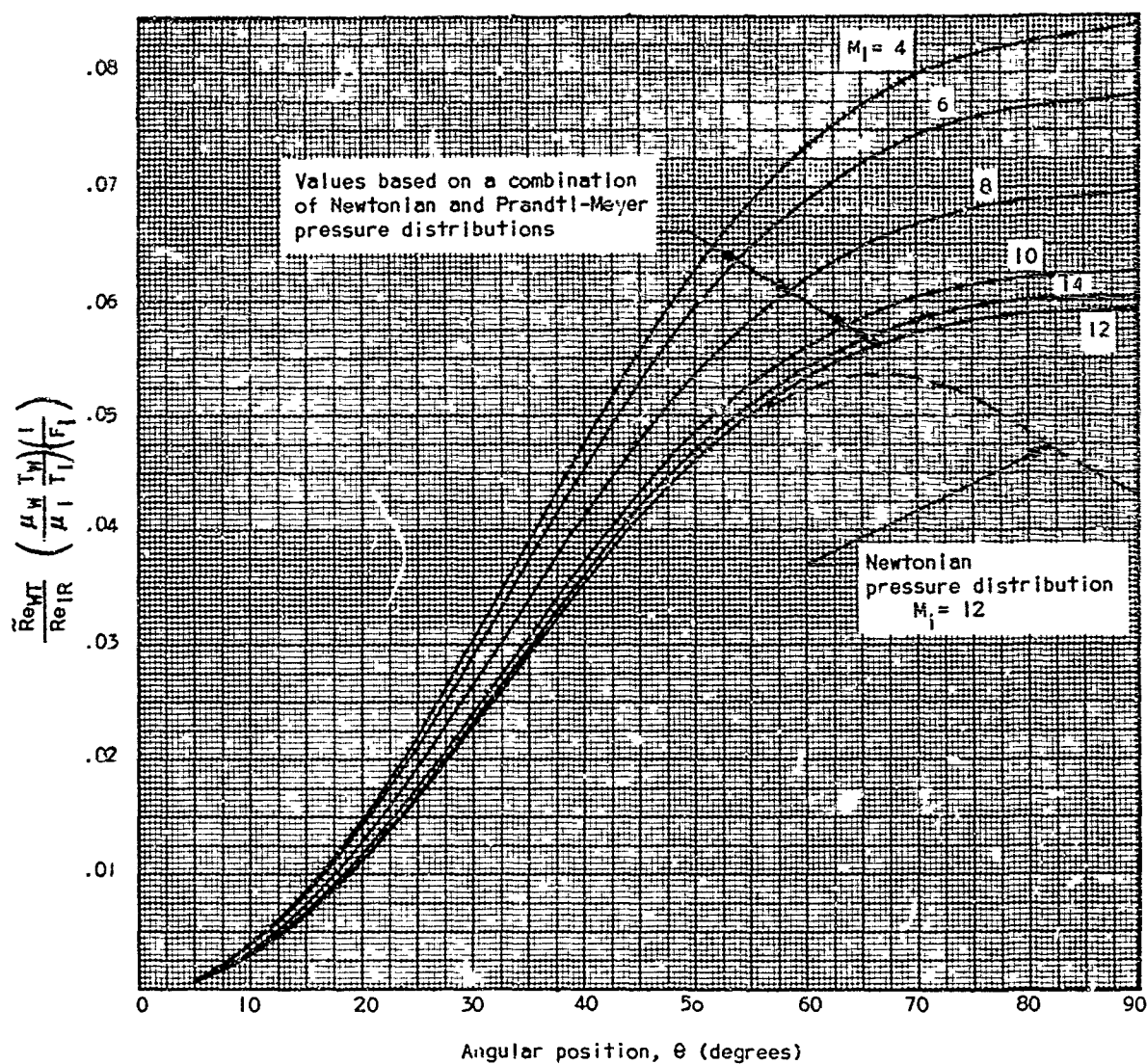


Fig. 67. $\left(\frac{\tilde{Re}_{WT}}{Re_{LR}} \right) \left(\frac{\mu_w}{\mu_1} \right) \left(\frac{T_w}{T_1} \right) \left(\frac{l}{F_1} \right)$ as a Function of Angular Position on a Hemisphere

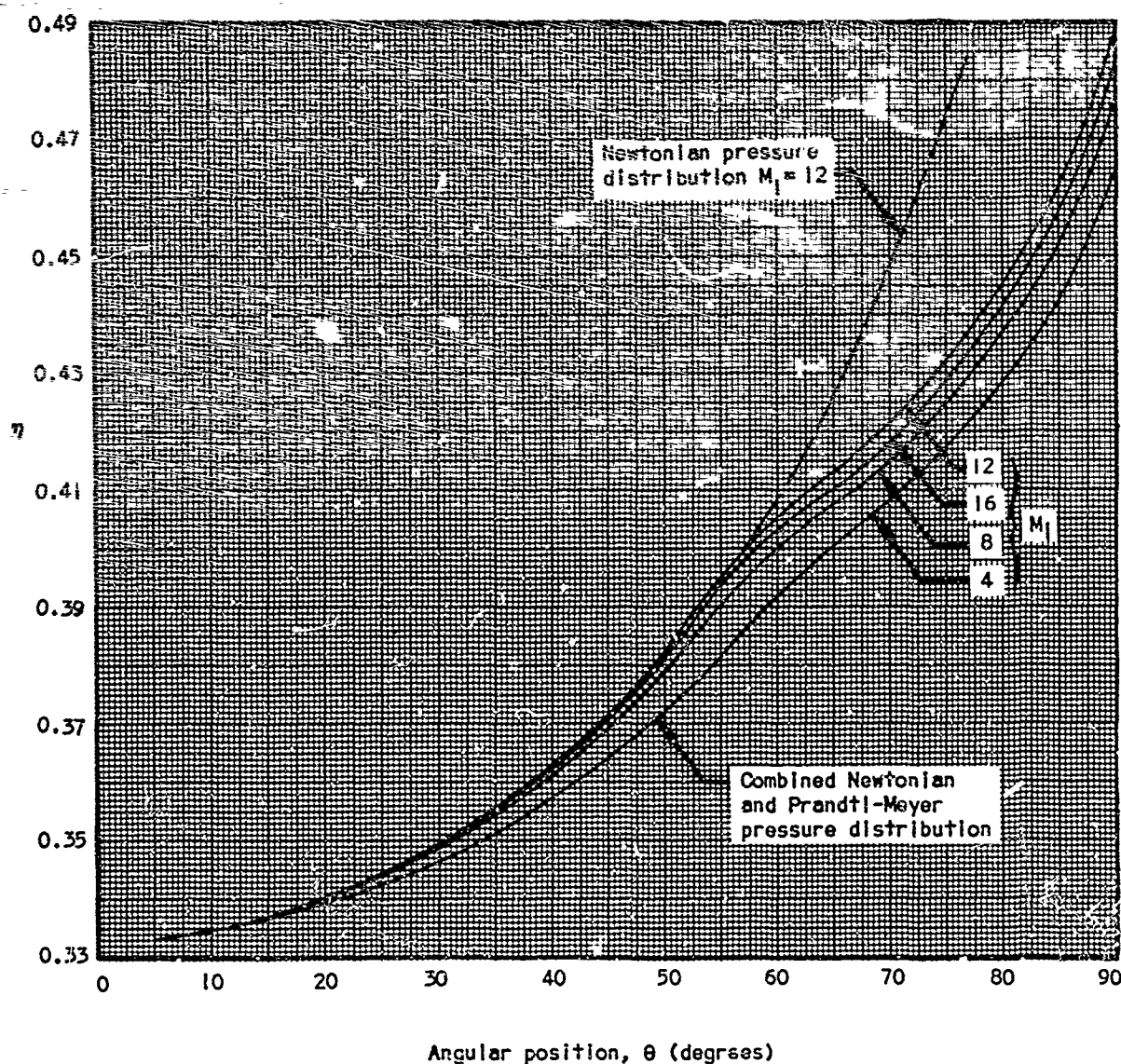


Fig. 68. C_p as a Function of Angular Position on a Hemisphere

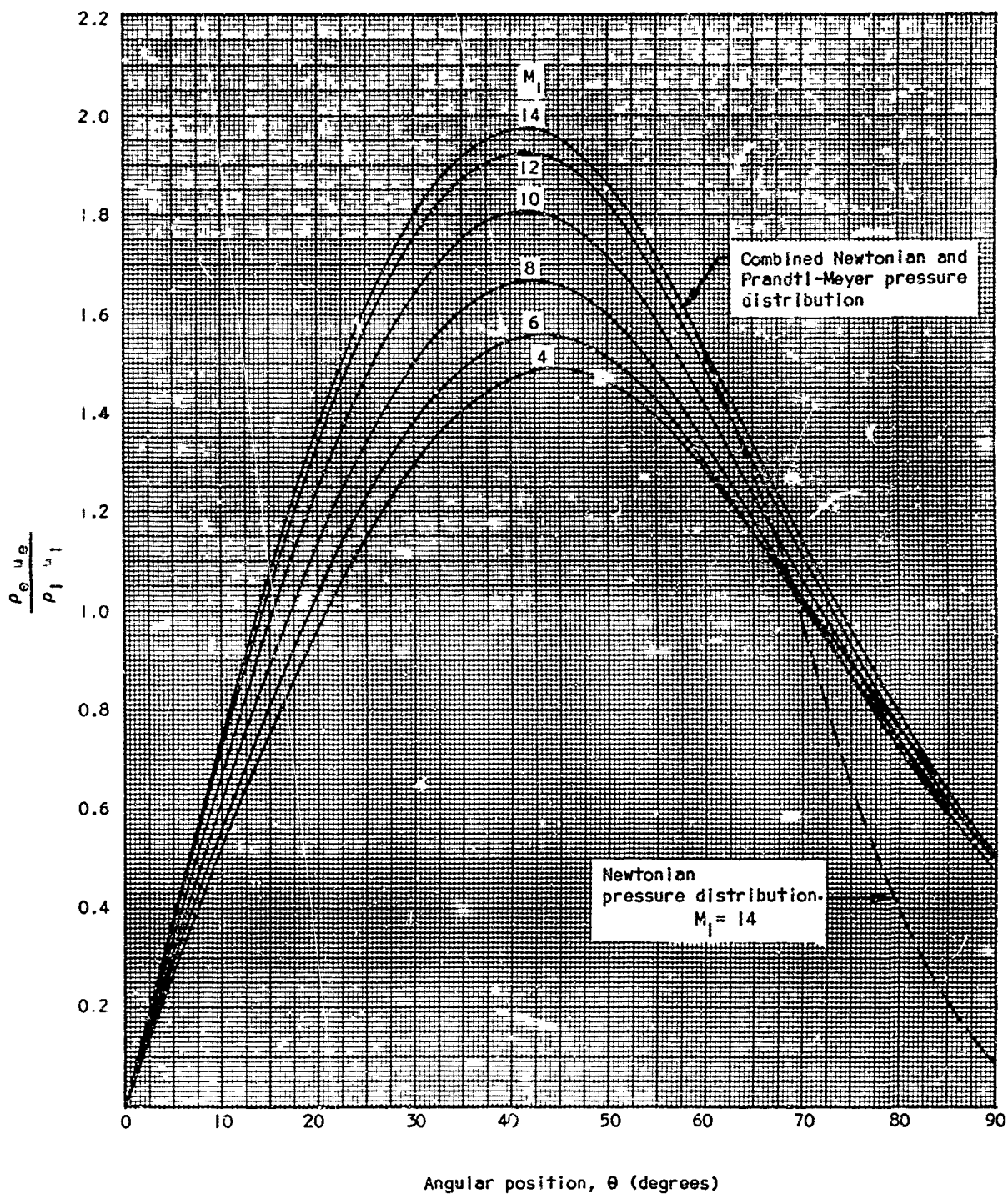


Fig. 69. $\rho_e u_e / \rho_1 u_1$ as a Function of Angular Position for Various Free-Stream Mach Numbers

REFERENCES

1. Summary Analysis of X-17 RTV Program, Lockheed Missile Systems Division Report LMSD-2161, 2 July 1957. Secret
2. X-17 R-1 Final Flight Report, Lockheed Missile Systems Division Report MSD-1834, 17 July 1956. Confidential
3. X-17 R-8 Final Flight Report, Lockheed Missile Systems Division Report MSD-3028, 1 January 1956. Secret
4. The Rocket Panel, "Pressures, Densities and Temperatures in the Upper Atmosphere," Physical Review, No. 88, 1952
5. AVCO, Preliminary Report on the Re-Entry Problem, October 1955. Secret
6. Bromberg, R., An Approximate Solution of the Boundary Layer Equations for Laminar Flow on a Blunt-Nosed Body of Revolution, Ramo-Wooldridge Corporation, 8 April 1955
7. Lees, L., Laminar Heat Transfer over a Blunt-Nosed Body at Hypersonic Flight Speeds, Ramo-Wooldridge Corporation, Revised November 1955
8. Denison, M. R., Turbulent Boundary Layer on Blunt Bodies of Revolution at Hypersonic Speeds, Lockheed Missile Systems Division Research Memorandum, April 1956
9. Van Driest, E. R., "Turbulent Boundary Layer in Compressible Fluids," Jour. Aero. Sci., Vol. 18, No. 3, March 1951
10. Bromberg, R., Fox, J. L., and Ackerman, W. O., "A Method of Predicting Convective Heat Input to the Entry Body of a Ballistic Missile," Transactions of the first Technical Symposium on Ballistic Missiles, Vol. IV, 22 June 1956. Secret

REFERENCES (Continued)

11. X-17 R-2 Preliminary Flight Report, Lockheed Missile Systems Division Report MSD-1882, / August 1956. Secret
12. X-17 R-11 Preliminary Flight Report, Lockheed Missile Systems Division Report MSD-2023, 8 November 1956. Secret
13. X-17 R-8 Preliminary Flight Report, Lockheed Missile Systems Division Report MSD-2012, 22 September 1956. Secret
14. X-17 R-9 Preliminary Flight Report, Lockheed Missile Systems Division Report MSD-2016, 26 October 1956. Secret
15. Armour Research Foundation, Measurements of Thermal Properties, August 1955
16. Battelle Memorial Institute, Thermal Conductivities, Heat Capacities, and Linear Thermal Expansion of Five Materials, November 1955